A study of hypertension induced nanoscale viscoelastic dysfunction of murine cardiovascular tissues

by

©Garrett McDougall

A Dissertation submitted to the School of Graduate Studies in partial fulfillment of the requirements for the degree of

MSc

Department of Chemistry

Memorial University of Newfoundland

July 2018

St. John's Newfoundland

Abstract

Arterial stiffness plays a pivotal role in the pathogenesis and progression of hypertension. Similarly, pathologies of the left ventricle can manifest as a consequence of hypertension. There is currently limited information regarding the impact of hypertension on the nanoscale viscoelastic behaviors of cardiovascular tissues. Using atomic force microscopy (AFM), we investigated viscoelasticity amongst vascular and cardiac tissues. AFM based measurements revealed viscoelastic distinctions between the differential layers of arterial vessels in hypertensive compared to normotensive rats in both the thoracic and abdominal aorta. These minimal nanoindentation studies identify impaired elasticity and energy dissipation throughout vasculature in the hypertensive state. Subtle changes in the epicardium and endocardium of the left and right ventricles were also found to exist, and such changes may be related to greater levels of fibrosis in cardiac tissue in hypertensive animals.

Acknowledgements

Firstly, I'd like to thank Erika for allowing me to continue my honours work in performing my Master's under her supervision. Her enthusiastic approach to chemistry and interest in each and every student within her group have instilled in myself a great interest in this work.

I'd also like to provide a very warm thanks to Dr. Reza Tabrizchi for not only cultivating the samples used in this work, but also for several very insightful conversations concerning the physiology of these tissues. Moreover, I should also like to thank Reza for his encouraging approach to the study of physiology and legitimate interest in my doings outside of the lab.

I should further like to acknowledge the efforts of Shaykat Saha who played an important role in imaging during my honours work and has also contributed to the work presented here on several occasions as he now continues his work elsewhere.

Finally I'd like to thank the National Science and Engineering Research Council of Canada (NSERC) and the Canadian Foundation for Innovation (CFI) for their funding.

Table of Contents

Abstract **ii**

Acknowledgments **iii**

List of Tables **viii**

List of Figures **xvi**

List of Abbreviations **xvii**

1 Introduction **1**

1.1 Hypertension 1

1.2 Function of the Efferent Vascular Tree 2

1.3 Arterial Remodelling in Hypertension 4

1.4 Cardiac Structure and Pathologies 7

1.5 Atomic Force Microscopy 9

1.6 Determination of Viscoelastic Properties by Force Spectroscopy 10

1.6.1 Determination of Elastic Modulus by the Hertz Model 12

1.6.2 Determination of Viscoelastic Properties 14

1.7 Investigating Hypertensive Nanomechanics 15

1.8 Summary 16

Bibliography 16

Co-authorship Statement **22**

2 Probing hypertension induced nanoscale dysfunction of murine aorta by AFM **24**

2.1 Introduction 24

2.2 Experimental 26

2.2.1 Aorta Sample Preparation 26

2.2.2 AFM Sample Preparation and Calibration 27

2.2.3 Nanoscale Arterial Imaging 27

2.2.4 AFM Force Mapping 28

2.2.5 AFM Creep Analysis 28

2.3 Results 30

2.3.1 Nanoscale Elasticity 30

2.3.2 Creep Deformation and Characteristics 34

2.4 Discussion 38

2.5 Conclusions 42

Bibliography 42

3 Nanomechanical Viscoelastic Characterization of Normotensive and Hypertensive Murine Tunica Media **48**

3.1 Introduction 48

3.2 Experimental 50

3.2.1 Tunica Media Sample Preparation 50

3.2.2 AFM Sample Preparation and Calibration 51

3.2.3 AFM Force Spectroscopy and Analysis 51

3.3 Results and Discussion 51

3.3.1 Nanoscale Topography of the Tunica Media 51
3.3.2 Nanoscale Elasticity of the Tunica Media 53
3.3.3 Nanoscale Creep Deformation of the Tunica Media 57
3.3.4 Relationships Between Elastic Modulus and Creep 62
3.4 Conclusions 69
Bibliography 72

4 Nanomechanical Viscoelastic Characterization of Normotensive and Hypertensive Murine Heart Tissues 76
4.1 Introduction 76
4.2 Experimental 78
4.2.1 Heart Sample Preparation and AFM Calibration 78
4.2.2 AFM Force Spectroscopy and Analysis 79
4.3 Results 79
4.3.1 Nanoscale Topography of the Heart 79
4.3.2 Nanoscale Elastic Properties of Heart Tissues 82
4.3.3 Nanoscale Viscoelastics of Heart Tissues 86
4.4 Conclusions 95
Bibliography 97

5 Conclusions 102
5.0.1 Hypertension-Induced Nanomechanical Dysfunction Across the Arterial Wall 102
5.0.2 Hypertensive Remodelling in the Heart Induces Nanomechanical Dysfunction 103
5.0.3 Qualitative Relationships Between Nanoscale Elasticity and Viscoelasticity 105

5.1 Future Directions . . . 105
5.1.1 Arterial De-stiffening and Risk Mitigation . . . 105
5.1.2 Nanomechanical and Topographical Investigation of the Myocardium . . . 106
Bibliography . . . 107

A Energy of Viscous Dissipation **108**
Bibliography . . . 113

B A Raman Investigation of Retinoids in Murine Eye Tissue **114**
B.1 Introduction . . . 114
B.2 Methods . . . 116
B.3 Results and Discussion . . . 116
B.4 Conclusions . . . 124
B.4.1 Future Directions . . . 125
Bibliography . . . 126

C Effect of Parameters **127**

D Programming **129**
D.1 Creep Analysis Procedure . . . 129
D.2 Automated Raman Plotting . . . 138
D.3 Raman Comparison . . . 146

List of Tables

2.1 Elastic moduli and characteristic response times of phase I and phase II relaxation for the intimal tissues of SHR and WKY 31

2.2 Elastic moduli and characteristic response times of phase I and phase II relaxation for the adventitial tissues of SHR and WKY 32

3.1 Elastic moduli, creep characteristic response times of phase I and phase II relaxation for the medial tissues of SHR and WKY 61

4.1 Elastic moduli, creep characteristic response times of phase I and phase II relaxation for the epi and endocardial tissues of the healthy WKY rat. 90

4.2 Elastic moduli, creep characteristic response times of phase I and phase II relaxation for the epi and endocardial tissues of the healthy WKY rat. 91

A.1 Energies of viscous dissipation along with associated ranges for all arterial tissues. 110

List of Figures

1.1 The Windkessel effect in elastic and inelastic arteries depicting differences in systolic compliance and subsequent diastolic recoil. 2
1.2 Cross-sectional view depicting hypertensive arterial remodelling as a function of elastic fiber degradation, extracellular matrix calcification, and collagen deposition. 4
1.3 Cross-sectional view of the heart wall. 7
1.4 Normotensive aortic pressure waveform (grey) is altered by the hypertensive aorta (red). 8
1.5 Working schematic of AFM using beam deflection detection 9
1.6 Representative force spectroscopy experiment with approach, constant force tip-dwelling, and retraction regimes. 11
1.7 Lennard-Jones potential with relevant AFM imaging modes. 12
1.8 Representative plot of creep indentation occurring on arterial tissues during a dwelling phase with a trigger force of 10 nN. Appropriateness of bi-exponential fit demonstrated. 14
1.9 Standard linear solid model composed of two parallel Maxwell elements in series with a purely elastic spring to describe two simultaneously occurring viscoelastic processes, representative of a hierarchical tissue behaviour. 15

2.1 SLS model composed of two Maxwell elements in parallel with a purely elastic spring to describe two simultaneously occuring processes, representative of a hierarchical tissue behaviour. 29
2.3 Representative AFM height images from each area of analysis. (A) Thoracic intima of the SHR featuring fenestrations (B) Abdominal intima of the WKY also featuring fenestrations and unidentified micropolyp like structures (C) Thoracic adventitia of the SHR demonstrating significant fibril density (D) Abdominal adventitia of SHR with possible insertion point of *vasa vasorum* and periaortic fat. 30
2.4 (A) Typical creep indentation force-spectroscopy experiment and (B) creep deformation observed during the dwell phase with corresponding force profile (B). 31
2.5 Box and whisker plots of elastic modulus for the tunica adventitia and the tunica intima, N=6000 for each box. 33
2.6 Box and whisker plots of creep deformation for the tunica adventitia and the tunica intima, N=6000 for each box. 34
2.7 Creep deformation and elastic modulus histograms contrasting the tightly distributed behavior of the WKY thoracic intima with the skewness (right and left respectively) of the SHR analogue. 35
2.8 Log-scaled box and whisker plots of characteristic creep times τ_1 and τ_2 for healthy and hypertensive thoracic intima, N=2500 for each box. . . 36
2.9 Log-scaled box and whisker plots of characteristic creep times τ_1 and τ_2 for healthy and hypertensive abdominal intima, N=2500 for each box. . 38
2.10 Log-scaled box and whisker plots of characteristic creep times τ_1 and τ_2 for healthy and hypertensive thoracic adventitia, N=2500 for each box. 39

2.11 Log-scaled box and whisker plots of characteristic creep times τ_1 and τ_2 for healthy and hypertensive abdominal adventitia, N=2500 for each box. 40

3.1 Amplitude images of healthy thoracic tunica media (left) and hypertensive thoracic tunica media (right) with readily apparent collagen. . . . 52

3.2 Amplitude images of healthy abdominal tunica media (left) and hypertensive thoracic tunica media (right) with greater collagen density and ellipsoidal structures apparent. 53

3.3 Box and whisker plots of elastic modulus for the thoracic and abdominal tunica media in the healthy case demonstrating lesser elasticity of the abdominal media N=8000 for each box. 54

3.4 Log-scaled box and whisker plots of elastic modulus for the thoracic and abdominal tunica media in the hypertensive case demonstrating lesser elasticity of the abdominal media N=8000 for each box. 54

3.5 Box and whisker plots of elastic modulus for the thoracic and abdominal tunica media in the hypertensive and healthy case. N=8000 for each box. 56

3.6 Box and whisker plots of creep deformation for the tunica media of the thoracic and abdominal aorta in the healthy case demonstrating lesser elasticity of the abdominal media N=8000 for each box. 59

3.7 Box and whisker plots of creep deformation for the tunica media of the thoracic and abdominal aorta in the healthy and hypertensive case, N=8000 for each box. 59

3.8 Box and whisker plots of creep deformation for the tunica media of the thoracic and abdominal aorta in the healthy and hypertensive case, N=8000 for each box. 60

3.9 Box and whisker plots of the short-term creep characteristic, τ_1, for the tunica media of the thoracic and abdominal aorta in the healthy and hypertensive case, N=5000 for each box. 61
3.10 Box and whisker plots of the long-term creep characteristic, τ_2, for the tunica media of the thoracic and abdominal aorta in the healthy and hypertensive case, N=5000 for each box. 62
3.11 Elastic modulus (left) and creep (right) maps taken at the same site on the healthy thoracic tunica media in sequence display visual relationships between the two properties. 63
3.12 Amplitude images of healthy abdominal tunica media (left) and hypertensive thoracic tunica media (right) with greater collagen density and some VSMCs apparent. 64
3.13 Amplitude images of healthy abdominal tunica media (left) and hypertensive thoracic tunica media (right) with greater collagen density and some VSMCs apparent. 64
3.14 Relationship between elastic modulus and creep for the healthy (left) and hypertensive (right) thoracic intima. 66
3.15 Relationship between elastic modulus and creep for the healthy (left) and hypertensive (right) abdominal intima. 66
3.16 Relationship between elastic modulus and creep for the healthy (left) and hypertensive (right) thoracic media. 67
3.17 Relationship between elastic modulus and creep for the healthy (left) and hypertensive (right) abdominal media. 67
3.18 Relationship between elastic modulus and creep for the healthy (left) and hypertensive (right) thoracic adventitia. 68

3.19 Relationship between elastic modulus and creep for the healthy (left) and hypertensive (right) abdominal adventitia. 68
3.20 Force-relaxation plots showing decay of force over time for a tip held at constant indentation depth by the piezo. 69

4.1 Amplitude images of healthy left ventricular endocardium (left) and hypertensive left ventricular endocardium (right) show relative smoothness of both tissues with possible underlying fibrillar structures in the hypertensive endocardium. 80
4.2 Amplitude images of healthy left ventricular epicardium (left) and hypertensive left ventricular epicardium (right) demonstrating increased bulbosity in the hypertensive case. 80
4.3 Amplitude images of hypertensive left ventricular myocardium showing what may be surface features of VSMCs. 81
4.4 Box and whisker plots of elastic modulus for the endo and epicardium of each the left and right ventricles for the healthy case. N=8000 for each box. 82
4.5 Box and whisker plots of elastic modulus for the endo and epicardium of each the left and right ventricles for the hypertensive case. N=8000 for each box. 83
4.6 Box and whisker plots comparing the elastic modulus of the endocardium for each the left and right ventricles between the healthy and hypertensive case. N=8000 for each box. 84
4.7 Box and whisker plots comparing the elastic modulus of the epicardium for each the left and right ventricles between the healthy and hypertensive case. N=8000 for each box. 85

4.8 Box and whisker plots showing the creep deformation of the endo and epicardium for each the left and right ventricle of the healthy case. N=8000 for each box. 88
4.9 Box and whisker plots showing the creep deformation of the endo and epicardium for each the left and right ventricle of the hypertensive case. N=8000 for each box. 89
4.10 Box and whisker plots comparing the creep deformation of the epicardium for each the left and right ventricles between the healthy and hypertensive case. N=8000 for each box. 90
4.11 Box and whisker plots comparing the creep deformation of the endocardium for each the left and right ventricles between the healthy and hypertensive case. N=8000 for each box. 91
4.12 Box plots showing distribution of short-term relaxation times, τ_1, for healthy and hypertensive ventricular endocardia. 92
4.13 Box plots showing distribution of long-term relaxation times, τ_2, for healthy and hypertensive ventricular endocardia. 93
4.14 Box plots showing distribution of short-term relaxation times, τ_1, for healthy and hypertensive ventricular epicardia. 94
4.15 Box plots showing distribution of long-term relaxation times, τ_2, for healthy and hypertensive ventricular epicardia. 94

A.1 Typical force spectroscopy experiment with dwell phase. Area of hysteresis used to determine energy of viscous dissipation shaded in light blue. 108
A.2 Box and whisker plots showing relative magnitude of dissipated energies for healthy and hypertensive abdominal intima, N=1200 for each box. . 111

A.3 Box and whisker plots showing relative magnitude of dissipated energies for healthy and hypertensive thoracic media, N=6000 for each box. . . 112
A.4 Box and whisker plots showing relative magnitude of dissipated energies for healthy and hypertensive abdominal adventitia, N=1200 for each box. 113

B.1 Structures of the most common retinoids in their predominant physiological isomers. 115
B.2 Raman spectra of the C56B6 whole eye on glass substrate. 117
B.3 Normalized Raman spectra of the C56B6 whole eye on glass substrate. 117
B.4 Normalized Raman spectra of the C56B6 whole eye on front side of silicon front. 118
B.5 Raman spectra of the C56B6 whole eye on front side of silicon reverse side. 119
B.6 Normalized Raman spectra of the C56B6 whole eye on Mica. 120
B.7 Static Raman spectra about 950 cm^{-1} of the C56B6 whole eye on Mica. 121
B.8 Raman static scan about 1620 cm^{-1} of the C56B6 whole eye on Mica. . 122
B.9 Extended Raman scans of Retinyl Acetate standard under 10x objective with 10 s exposure. 123
B.10 Extended Raman scan of Retinyl Acetate standard under 10x objective with 10 s exposure with in-spectrum normalization, peaks of itnerest are labelled. 124

C.1 Effect of increasing trigger force on indentation depth. 127
C.2 Mild exponential relationship between elastic modulus and indentation taken from healthy tunica media. 128
C.3 Increasing trigger force seems to produce no significant difference in mean elastic modulus. 128

D.1 RamanPlot.ipf generated Raman plot for 20 spectra with intraspectrum normalization. 139
D.2 RamanPlot.ipf generated Raman plot for 20 spectra with interspectra normalization. 140
D.3 RamanComparison.ipf generated Raman plot for 4 spectra with intraspectrum normalization for visual comparison of spectral similarity. . 147
D.4 RamanComparison.ipf generated table of raw and relative similarity scores of Raman Spectra 148

List of Abbreviations and Symbols

AA	Abdominal Adventitia (Externa)
AC	Alternating-Contact (Tapping) Mode
AFM	Atomic Force Microscopy
AI	Abdominal Intima
AM	Abdominal Media
E	Elastic (Young's) Modulus
GM	Garrett McDougall
LA	Left Atrium
LV	Left Ventricle
LVH	Left Ventricular Hypertrophy
RA	Right Atrium
RV	Right Ventricle
SHR	Spontaneously Hypertensive Rat
SPM	Scanning Probe Microscopy
SS	Shaykat Saha
TA	Thoracic Adventitia (Externa)
TI	Thoracic Intima
TM	Thoracic Media
WKY	Wistar-Kyoto Rat

Chapter 1

Introduction

1.1 Hypertension

Since the advent of the twenty-first century, cardiovascular diseases have consistently been ranked as the leading cause of death globally. Within this category, hypertension (defined as persistent and prolonged elevation of arterial blood pressure) is recognized as the leading global risk-factor for mortality. [1] Hypertension also presents with exceptionally high morbidity and affects the heart, blood vessels, kidneys, brain, and eyes. [2] Not only does hypertension have high mortality rates and significant associated morbidity, it is also exceptionally costly on an economic level with hypertension treatment and care costing an estimated 48.6 billion USD yearly in the U.S. alone. [3]

Consequently, there has been significant effort and investment towards elucidating the mechanism and pathogenesis of hypertension. To date, there exists no consensus on the mechanism of essential hypertension. [4] While there exists extensive research to characterize the biochemical behaviour of hypertensive vasculature and cardiac tissues on large scales and also the bulk-scale mechanics. [5] There is little information about the nanomechanical changes occurring to these tissues. [6] The work detailed in

this thesis will focus on the purely elastic and viscoelastic characteristics of healthy and hypertensive murine aortic and ventricular tissues.

1.2 Function of the Efferent Vascular Tree

To understand why these nanoscale viscoelastic properties are of particular interest, an understanding of their function on the bulk-scale is helpful. The efferent, or outward conducting, blood vessels being the aorta, arteries, arterioles and the capillaries function to conduct blood throughout the body with the ultimate goal of perfusing tissues and organs. These classifications of afferent vessels can also be considered in terms of elastic arteries, muscular arteries, and arterioles.

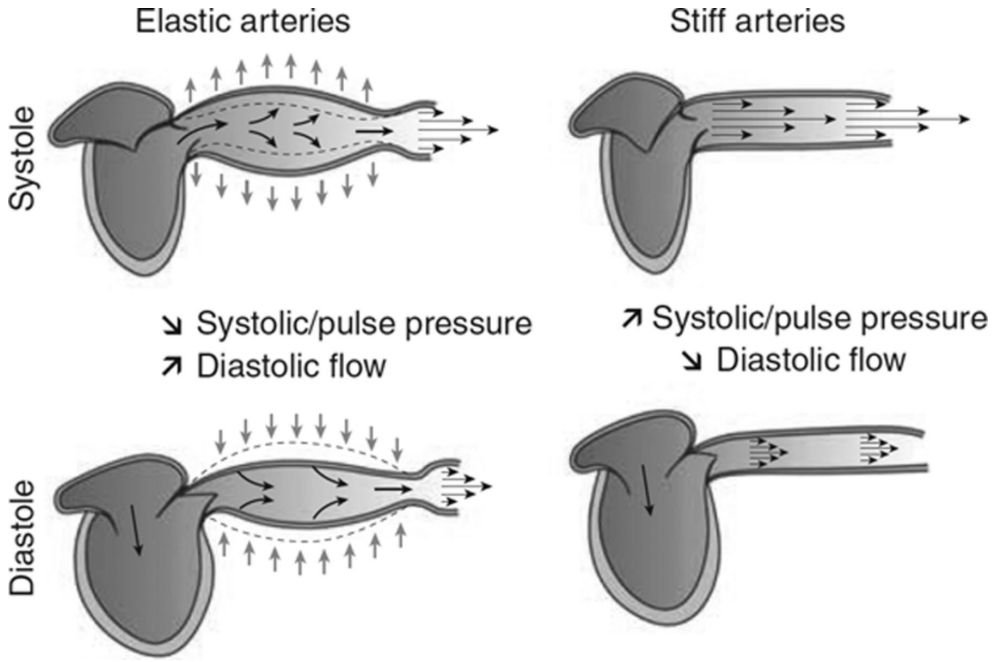

Figure 1.1: The Windkessel effect in elastic and inelastic arteries depicting differences in systolic compliance and subsequent diastolic recoil. (Reprinted with permission from Laurent and Boutouyrie (2015). Copyright 2015 Circulation Research.) [7]

Elastic arteries, such as the aorta which is the largest vessel, have many compositional and structural distinctions from the other forms of afferent vessels. Primarily,

they have significantly higher elastin content in the tunica media, the middle layer of the arterial wall. This ultimately results in these vessels being much more compliant, allowing for vascular damping of pulsatile pressures resulting from left ventricular contraction. [8] The characteristic behaviour of these large, elastic arteries is considered to be Windkesselian or "wind-chamber" like, see Figure 1.1. [7] This behaviour is characterized by distension of the vessel during left ventricular contraction and subsequent relaxation after ventricular contraction. This behaviour is important for several reasons:

1. The significant compliance and related expansion of elastic arteries dissipates pulsatile energy and mitigates tissue damage.

2. Diastolic, i.e. when the heart is not actively contracting, recoil allows for optimal perfusion of distal tissues due to continued flow during diastole.

3. Appropriate recoil timing enables coronary perfusion by augmenting wave reflections, i.e. blood flow directed back towards the heart, returning from peripheral vessels.

4. Appropriate recoil and wave reflection timing decreases cardiac afterload by ensuring wave reflections do not return during peak systolic ejection.

Consequently, any impairment of this Windkesselian behaviour will have deleterious effects upon the vascular tree due to unmitigated pulse pressures throughout and also upon the heart due to increased left ventricular afterload, the pressure that the left ventricle works against in order to eject blood. This is discussed further in Section 4.3.2.

Muscular or conduit arteries serve to guide the flow of blood towards various organs and tissues throughout the body. [9] These muscular arteries then give way

to arterioles which have many smooth muscle cells controlled by the sympathetic nervous system through sympathetic innervation, allowing for vasoconstriction and dilation. This control of vascular tone not only allows for blood pressure control in the form of increased total peripheral resistance (the sum resistance of the vascular circuit against which heart pumps) through systemic arteriolar vasoconstriction which causes widespread contraction of the arteries to decrease the total space available. Vasoconstriction can also direct blood towards tissues in need of perfusion by dilating some vessels while constricting others. [10] Finally, the arterioles feed into capillaries which, being comprised of only a singular layer of endothelial cells, allow for diffusion of gases, nutrients, and other factors between microcirculation and nearby tissues. [11] Circulation then proceeds to the venules, the microcirculatory component of afferent circulation which is concerned with blood returning to the heart.

1.3 Arterial Remodelling in Hypertension

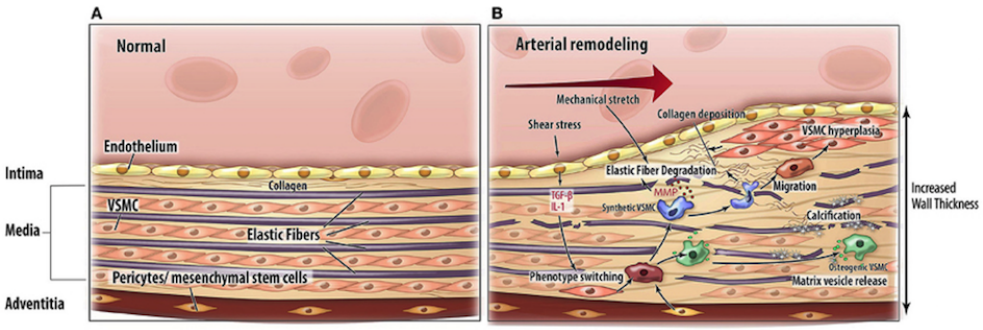

Figure 1.2: Cross-sectional view depicting hypertensive arterial remodelling as a function of elastic fiber degradation, extracellular matrix calcification, and collagen deposition. (Reprinted with permission from Van Varik et al under CC by 3.0.) [12]

As depicted in Figure 1.2, arteries have three concentric layers. The innermost layer is the tunica intima which, on its luminal (inner) side, sports endothelial cells in direct contact with arterial blood flow and the constituents thereof. Once considered to

function strictly as a physical barrier between the arterial wall and the blood which flows within, the endothelial lining is now understood to have not only notable vasoprotective (concerned with protecting the vasculature) function but also to contribute directly to vascular tone through endothelium derived vasoactive factors, i.e. hormonal or paracrine factors which have effects on the vasculature. [13] This endothelial layer, in the normotensive case, is supported by underlying collagen fibrils which may be displaced in pathologies by vascular smooth muscle cells (VSMCs) or plaques. [14] Intimal VSMC hyperplasia, an increase in the reproduction rate of these cells, as well as endothelial hyperplasia combine with thickening of the media to produce stiffer, thickened arterial walls. Of diagnostic concern, increased intima-media thickness has been identified as a marker for early hypertension-induced alterations to the arterial wall which can be identified by ultrasound. [15]

Beneath the tunica intima lies the thick, muscular tunica media, composed largely of elastic tissue (elastin) and smooth muscle cells. Particularly in the aorta, the elastin content of the tunica media is considerable. Hypertensive media is primarily characterized by generalized thickening which has been related to: i) hyperplasia and hypertrophy (increase in size) of VSMCs, and ii) neogenesis of the connective matrix, particularly of that related to collagen fibrillogensis. [16] Similarly, redistribution and degradation of medial elastin have been identified as an earmark of hypertensive alterations. [17, 18] Elastic fiber degradation has also been recognized as a factor in age-induced arterial stiffening. At the same time, increased pulse pressures associated with hypertension causing increased stretching of elastic fibers has been shown to hasten the degradation process. [19] In young, healthy individuals elastin in the media is primarily formed by VMSCs. However, in aged or hypertensive populations, these VSMCs tend to synthesize collagen in place of elastin. [20] This implies that hypertension not only induces the breakdown of these elastic components, but also pre-maturely inhibits

their production.

The outermost arterial layer, the tunica adventitia, is composed largely of collagen fibres. This layer has been reported to support up to a fourth of the pressure load normally. In hypertensive pathologies the adventitia can be expected to support pressures near 50% of the total pressure load. [21] Notably, this layer has been found to undergo significant remodelling during hypertension. [22] Being a large, predominantly collagenous layer the collagen composition of the adventitia in both the healthy and hypertension case is of particular interest. Type I collagen has previously been localized to the outer media and adventitia and is expected to play a role in vascular resistance in order to limit distensibility. Type III collagen, however, has been found to be distributed diffusely throughout the differential layers. These fibrils are comparatively fine and are involved primarily in the arrangement of VSMCs. [23, 24] Interestingly, the proportion of Type I relative to Type III fibres has been seen to increase sharply with increased pressure-loads, the net effect being to reduce the content of the more elastic Type III collagen and replace it with the stiffer Type I collagen. Ultimately, this stiffening behaviour of the adventitia may ear-mark it as the mechanically predominant layer in hypertension.

Hypertension and vascular stiffening have always presented researchers with something of a "chicken or the egg" conundrum. However, work by Lee and co-workers has identified that hypertension in the SHR may be instigated by arterial remodelling occurring prior to any significant increase in arterial pressure. [25, 26] However, that work was concerned with bulk-scale phenomena while here we are concerned with nanoscale behaviours. This is important as exceptionally small changes in pressure and other factors may induce nanoscale structural and mechanical changes as will be investigated here. For this reason, it cannot be said that remodelling occurs prior to hypertension without properly evaluating tissue response on the most minute of scales.

1.4 Cardiac Structure and Pathologies

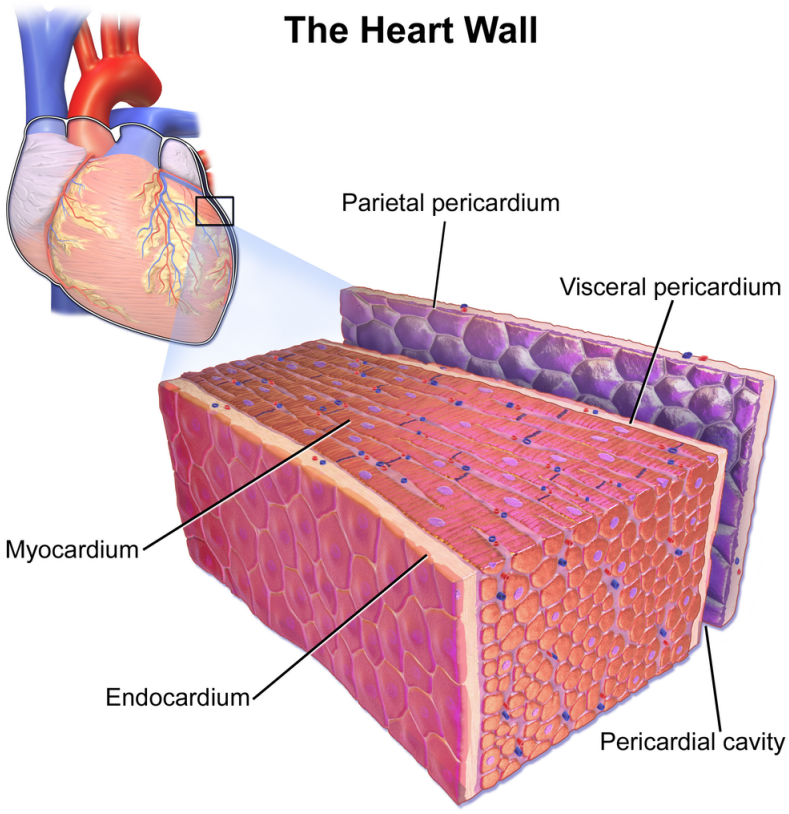

Figure 1.3: Cross-sectional view of the heart wall. (Reprinted with permissions from Blausen under CC by 2.0.)

The heart is a muscular, four chambered organ responsible for pulmonary and systemic circulation with the the respective intents of oxygenating the blood and then perfusing tissues throughout the body. In order to do so, blood is first shunted by contraction of the right ventricle through the pulmonary artery into pulmonary circulation where off-gassing of metabolic by-products and simultaneous oxygenation occurs by function of partial pressure gradients. Oxygenated blood then returns to left ventricular holding via the pulmonary vein and left atrium. Upon left ventricular contraction the blood is ejected into the aorta through the semilunar aortic valve. Once entering the aorta, blood flow continues distally. The inertia resulting from

ventricular ejection provides impetus for continued forward flow but is also augmented by the Windkessel effect. This behaviour is discussed in Section 1.2 as is the associated mechanism of the wave reflection.

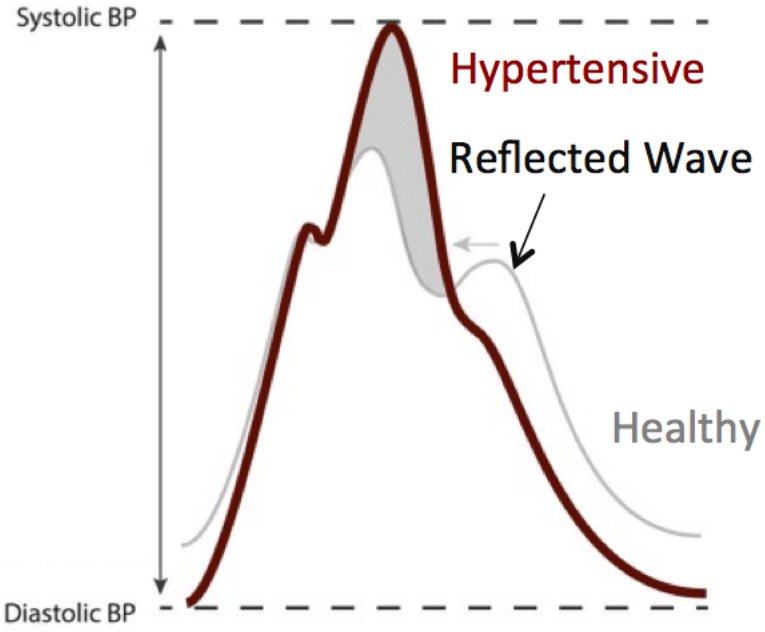

Figure 1.4: Normotensive aortic pressure waveform (grey) is altered by the hypertensive aorta (red). (Adapted with permissions from Teemu et al under CC BY-NC 3.0.) [27]

The pressure in the aorta which the left ventricle pumps against is known as cardiac afterload and is frequently seen to increase in hypertensive conditions. This increased afterload and altered coronary perfusion initiates a series of changes to the heart that fall under the umbrella of "hypertensive heart". Here we are most concerned with wave reflection timing and total peripheral resistance. Wave reflection is one component of the aortic pressure waveform which arises from a forward-travelling wave generated by left ventricular ejection and is sustained by Windkesselian behaviour. Occurring after the forward-travelling wave is the wave reflection discussed in Section 1.2 which arises primarily from peripheral vasculature (mainly the arterioles). [28] This wave reflection can be observed in the healthy case depicted in Figure 1.4 and generally returns to the heart during late diastole. [29] For this reason, altered arterial viscoelastics (i.e.

changes to the magnitudes and rate of Windkesselian behaviour) may offset the timing of wave reflections, which can consequently impair coronary perfusion and optimal myocardial blood flow. [30] Importantly, if the wave reflection returns during systole, when the heart is actively contracting, we can expect increased cardiac afterload which has been observed to induce left ventricular hypertrophy, a common presentation of hypertensive heart. [31, 32]

1.5 Atomic Force Microscopy

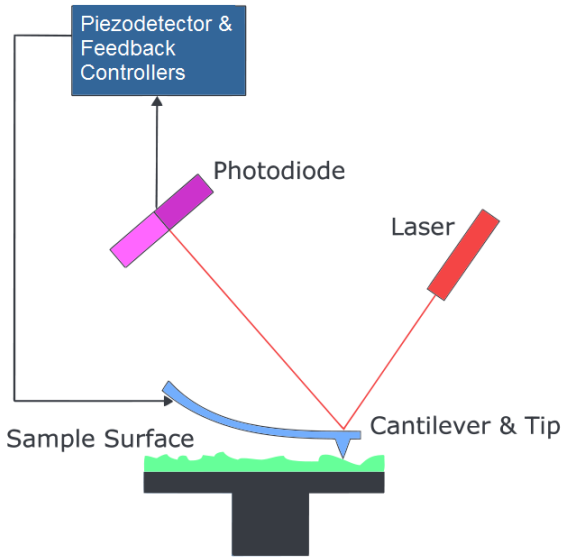

Figure 1.5: Working schematic of AFM using beam deflection detection. (C.C. by 3.0 under public domain.)

Atomic Force Microscopy (AFM) is a Scanning Probe Microscopy (SPM) technique which allows for nano-scale surface analyses such as topographical imaging, mechanical analysis, and many others. In AFM, Figure 1.5, a nanoscale probe mounted on a cantilever is raster-scanned across the sample surface allowing for collection of data along with its associated location. This is typically accomplished in one of two modes:

i) Contact mode, where the tip is in physical contact with the surface and changes in cantilever deflection are monitored to determine changes in height; and ii) Alternating Contact or Tapping mode, where the tip oscillates at a pre-determined amplitude above the sample surface. Changes in oscillatory amplitude due to interactions between the two are then observed and used to generate topographies. In each case a feedback variable (deflection in contact mode and amplitude in alternating contact mode) is used in a feedback loop which ensures the continuous restoration of tip height or amplitude, respectively. This is accomplished through the use of a piezoelectric scanner which expands and contracts in response to an applied voltage proportional to changes in the feedback variable.

Here we have investigated the properties of delicate biological tissues maintained in a state of continuous hydration. This provides that the mechanical and morphological properties of the sample better resemble those in vivo when compared to dehydrated samples. In fact, changes in the ionic composition of the hydrating solution have also been found to alter mechanical behaviour. [33] Hydrated tissues, being more delicate than their dehydrated analogues often necessitate the use of alternating contact mode to mitigate sample damage. Additionally, the error (amplitude) signal in alternating contact mode tends to show much more contrast than the height signal and emphasizes edges. [34] This can be seen in Figure 3.2.

1.6 Determination of Viscoelastic Properties by Force Spectroscopy

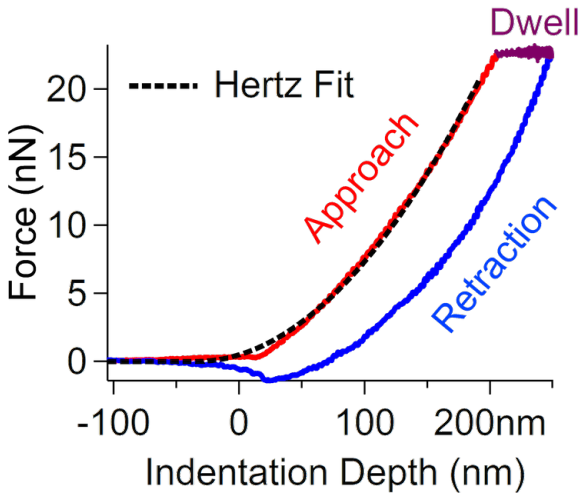

Figure 1.6: Representative force spectroscopy experiment with approach, constant force tip-dwelling, and retraction regimes.

AFM-based topographical analyses are often accompanied by either concurrent or subsequent force spectroscopy experiments which allow for the collection of mechanical data. These experiments can be particularly insightful to disclose the relation of mechanical properties to structural features. Figure 1.6 represents a typical force spectroscopy experiment conducted in this work. Notably, there are three phases of this experiment. Firstly, there is the approach or indentation phase where the tip is advanced towards the sample until reaching a point where attractive forces overwhelm and the tip jumps to contact with the sample, this occurs at an indentation depth of 0 nm in Figure 1.6. This occurs at an indentation depth of zero. Behaviour in this near-sample approach region can be modelled by the Lennard-Jones potential, Figure 1.7.

$$V(d) = 4\epsilon\left(\left(\frac{\sigma}{d}\right)^{12} - \left(\frac{\sigma}{d}\right)^{6}\right) \tag{1.1}$$

In the Lennard-Jones potential, Equation 1.1, V represents the intermolecular potential, ϵ the depth of energy well, σ the distance at which the intermolecular potential between the two particles is zero, and d the distance of separation between the two particles.

Once the tip has come into contact with the sample its indentation behaviour can then be described by the Hertz model, described next.

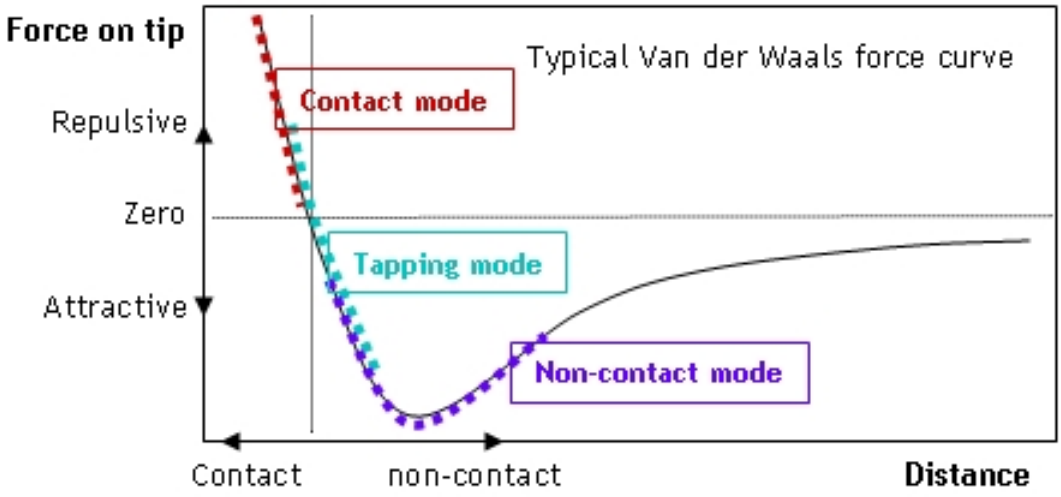

Figure 1.7: Lennard-Jones potential with relevant AFM imaging modes. (Permissions from Opensource Handbook of Nanoscience and Nanotechnology under CC by 2.5)

1.6.1 Determination of Elastic Modulus by the Hertz Model

Once making contact with the sample the indentation force is gradually increased and the tip indents into the sample. This continues until reaching the trigger force (20 nN in this case). This curve, depicted in red in Figure 1.6, can then be fit with the Hertz model, Equation 1.5, in order to determine the elastic modulus of the sample. The use of the Hertz model for determination of elastic moduli in biological samples is fairly ubiquitous and widely reported in the literature. [35] This approach models the elastic deformation experienced by two smooth bodies in contact under a known load. However, in doing so, two requirements must be satisfied. Firstly, we require that the depth of indentation be much smaller than the sample thickness. For minimal indentation methods, such as the one in question here, this holds. Secondly, we desire the indenter to be parabolic in shape. For minimal indentation methods, Mahaffy

and co-workers have previously demonstrated that this is the case with conical or spherical probes. [36] Additionally, the use of minimal nanoindentation here allows that substrate effects be treated as negligible since we indent less than a tenth of the samples thickness. [37]

If we approximate our tip as a sphere of radius R, then we may write the force on the cantilever, $F(\delta)$ as:

$$F(\delta) = \frac{4\sqrt{R}}{3} E^* \delta^{3/2} \tag{1.2}$$

Here δ is the indentation depth and E^* the reduced elastic modulus, calculated as:

$$\frac{1}{E^*} = \frac{1-\nu_{\text{tip}}^2}{E_{\text{tip}}} + \frac{1-\nu_{\text{sample}}^2}{E_{\text{sample}}} \tag{1.3}$$

Where ν is the Poisson's ratio, i.e. the ratio of transverse strain to axial strain which, for this sample, has been reported to be 0.45 for arterial tissues and 0.50 for cardiac tissues. [38] For biomaterials the indenter is often much harder than the sample. This means that $E_{\text{tip}} \gg E_{\text{sample}}$ and so:

$$E^* = \frac{E_{\text{sample}}}{1-\nu_{\text{sample}}^2} \tag{1.4}$$

This allows us to rewrite Equation 1.2 as:

$$F(\delta) = \frac{4\sqrt{R}}{3} \frac{E_{\text{sample}}}{1-\nu_{\text{sample}}^2} \delta^{3/2} \tag{1.5}$$

However, in our work we often utilize a conical indenter. The Sneddon expansion to the Hertz model accounts for conical tip geometries and gives the force on the

cantilever, $F(\delta)$ to be [39]

$$F(\delta) = \frac{2}{\pi} \frac{E_{\text{sample}}}{1 - \nu_{\text{sample}}^2} \tan(\alpha) \delta^2, \tag{1.6}$$

where α is the half-angle of the indenter.

1.6.2 Determination of Viscoelastic Properties

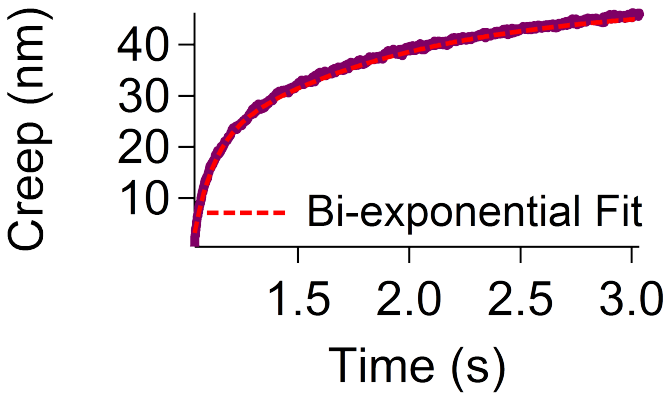

Figure 1.8: Representative plot of creep indentation occurring on arterial tissues during a dwelling phase with a trigger force of 10 nN. Appropriateness of bi-exponential fit demonstrated.

Once the indentation force has reached the trigger force the tip is allowed to dwell on the sample surface for some time. This means that the tip is held, at constant force, on the sample surface and the depth of the indentation is continually monitored. If there is further indentation of the tip into the sample during this phase it is indicative of accommodation on the part of the sample. This viscoelastic, or time-dependent elastic, behaviour is called creep deformation. Typically, when we observe the indentation versus time plot in this work, Figure 1.8, a continued indentation best fit bi-exponentially is seen. This would indicate that the closest mathematical approximation for the creep behaviour is bi-exponential. The bi-exponential behaviour of this accommodation is

telling of the nature of the process(es) occurring. Specifically, the requirement for a bi-exponential model indicates that there are likely two simultaneously occurring creep processes. This can then be represented by the mechanical model below, Figure 1.9. This is found to be the case for both the cardiac and arterial tissues in question.

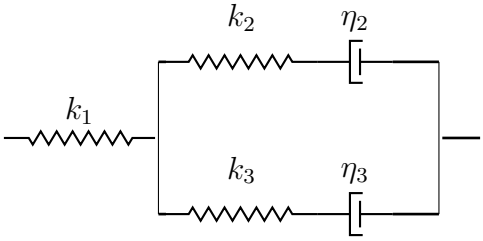

Figure 1.9: Standard linear solid model composed of two parallel Maxwell elements in series with a purely elastic spring to describe two simultaneously occurring viscoelastic processes, representative of a hierarchical tissue behaviour.

This model is comprised of a purely elastic spring in series with two parallel Maxwell elements, one for each simultaneously occurring viscoelastic process. Each Maxwell element contains an elastic spring element and a viscous dashpot. Using this model and the bi-exponential fit we can extract Equation 1.7 for the indentation depth, $\delta(t)$

$$\delta(t) = A_1 \exp\left(-\frac{t}{\tau_1}\right) + A_2 \exp\left(-\frac{t}{\tau_2}\right) \tag{1.7}$$

Where A_1 and A_2 are fitting constants, while τ_1 and τ_2 are the short and long term creep characteristics respectively. [40]

1.7 Investigating Hypertensive Nanomechanics

While neglected in the literature, the elucidation of hypertensive nanomechanics along with a scaled Finite Element Modelling (FEM) analysis will allow for new insight into the pathogenesis of hypertension. [41] The data presented later in this thesis indicates that hypertension affects tissues not only on the bulk scale, but also on the nanoscale.

This knowledge invites better understanding of the progression of hypertension and, at the same time, allows for therapies possibly targeting the nanomechanics of the tissues in question where most current treatments function on a biochemical or bulk scale. The work detailed here extends upon that of my honours work by returning to the tunicas intima and adventitia for characterization of their viscoelastic properties, by investigating elastic and viscoelastic properties of the tunica media, and the same in the endocardium and epicardium of the left and right ventricles.

The pairing of the SHR and WKY is one of the most commonly used models to investigate essential hypertension in humans. The SHR is simply a strain resulting from continual selection of WKY with higher blood pressures.

1.8 Summary

In Chapter 2 of this work my original honours work is discussed briefly in addition to the aforementioned viscoelastic analysis of the tunicas adventitia and intima conducted during my M.Sc. This chapter, being formatted as a paper, also discusses the methodology, instrumentation, and sample treatment used for this work. Chapter 3 presents and discusses the elastic and viscoelastic findings for both the healthy and hypertensive tunica media while Chapter 4 does the same for the epi and endocardium of the left and right ventricles.

Bibliography

[1] *Global health risks mortality and burden of disease attributable to selected major risks.* World Health Organization, Geneva, Switzerland, 2009. http://www.who.int/healthinfo/global_burden_disease/GlobalHealthRisks_report_full.pdf.

[2] J. Redon, M. Tellez-Plaza, D. Orozco-Beltran, V. Gil-Guillen, S. Pita Fernandez, J. Navarro-Pérez, V. Pallares, F. Valls, A. Fernandez, A. Perez-Navarro, C. Sanchis, A. Dominguez-Lucas, G. Sanz, and J. Martin-Moreno. Impact of hypertension on mortality and cardiovascular disease burden in patients with cardiovascular risk factors from a general practice setting. *Journal of Hypertension*, 34(6):1075, 2016.

[3] D. Mozaffarian and E. Benjamin. Heart Disease and Stroke Statistics. *Circulation*, 133(4):e38, 2016.

[4] M. Singh, G. Mensah, and G. Bakris. Pathogenesis and clinical physiology of hypertension. *Cardiology Clinics*, 28(4):545, 2010.

[5] S. Nadar, A. Blann, and G. Lip. Endothelial dysfunction: Methods of assessment and application to hypertension. *Current Pharmaceutical Design*, 10(29):3591, 2004.

[6] G. Brevetti, V. Schiano, and M. Chiariello. Cellular adhesion molecules and peripheral arterial disease. *Vascular Medicine*, 11(1):39–47, 2006.

[7] S. Laurent and P. Boutouyrie. The structural factor of hypertension: large and small artery alterations. *Circulation research*, 116(6):1007, 2015.

[8] H.P. Dustan. Atherosclerosis complicating chronic hypertension. *Circulation*, 50(5):871, 1974.

[9] M. Pugsley and R. Tabrizchi. The vascular system: An overview of structure and function. *Journal of pharmacological and toxicological methods*, 44(2):333, 2000.

[10] S. Segal. Regulation of blood flow in the microcirculation. *Microcirculation*, 12(1):33, 2010.

[11] S. Yuan and R. Rigor. *Regulation of Endothelial Barrier Function*. Morgan & Claypool Life Sciences, San Rafael, CA, USA, 2010.

[12] B. van Varik, R. Rennenberg, C. Reutelingsperger, A. Kroon, P. de Leeuw, and L. Schurgers. Mechanisms of arterial remodeling: lessons from genetic diseases. *Frontiers in genetics*, 3(13):290.

[13] A. Sandoo, J. van Zanten, G. Metsios, D. Carroll, and G. Kitas. The endothelium and its role in regulating vascular tone. *The open cardiovascular medicine journal*, 4:302, 2010.

[14] G. Favero, C. Paganelli, B. Buffoli, L. Rodella, and R. Rezzani. Endothelium and its alterations in cardiovascular diseases: life style intervention. *BioMed Research International*, 2014:801896, 2014.

[15] A. Simon, J. Gariepy, and G. Chironi. Intima–media thickness: a new tool for diagnosis and treatment of cardiovascular risk. *Journal of Hypertension*, 20(2):159, 2002.

[16] P. Hadjiisky, N. Peyri, and Y. Grosgogeat. Tunica media changes in the spontaneously hypertensive rat (SHR). *Atherosclerosis*, 65(1):125, 1987.

[17] J. Wagenseil and R. Mecham. Elastin in Large Artery Stiffness and Hypertension. *Journal of Cardiovascular Translational Research*, 5(3):264, 2012.

[18] A. Avolio and D. Jones. Quantification of alterations in structure and function of elastin in the arterial media. *Hypertension*, 32(1):170, 1998.

[19] E. Smith, L. Tomlinson, M. Ford, and L. McMahon. Elastin degradation is associated with progressive aortic stiffening and all-cause mortality in predialysis chronic kidney disease. *Hypertension*, 59(5):973, 2012.

[20] S. Greenwald. Ageing of the conduit arteries. *The Journal of Pathology*, 211(2):157, 2007.

[21] C. Schulze-Bauer, P. Regitnig, and G. Holzapfel. Mechanics of the human femoral adventitia including the high-pressure response. *American Journal of Physiology: Heart and Circulatory Physiology*, 282(6):H2427, 2002.

[22] S. Arribas, C. Hillier, C. González, S. McGrory, A. Dominiczak, and J. McGrath. Cellular aspects of vascular remodeling in hypertension revealed by confocal microscopy. *Hypertension*, 30(6):1455, 1997.

[23] C. Xu, C. Zarins, H. Bassiouny, W. Briggs, C. Reardon, and S. Glagov. Differential Transmural Distribution of Gene Expression for Collagen Types I and III Proximal to Aortic Coarctation in the Rabbit. *Journal of Vascular Research*, 37(3):170, 2000.

[24] M. Barnes and R. Farndale. Collagens and atherosclerosis. *Experimental Gerontology*, 34(4):513, 1999.

[25] R. Lee. *Blood vessel changes in hypertension : structure and function*. CRC Press, Florida, United States, 1989.

[26] D. Zhu, T. Herembert, and P. Marche. Increased proliferation of adventitial fibroblasts from spontaneously hypertensive rat aorta. *Journal of hypertension*, 9(12):1161, 1991.

[27] T. Niiranen, B. Kalesan, N. Hamburg, E. Benjamin, G. Mitchell, and R. Vasan. Relative Contributions of Arterial Stiffness and Hypertension to Cardiovascular Disease: The Framingham Heart Study. *Journal of the American Heart Association*, 5(11):e004271, 2016.

[28] W. Nichols and B. Singh. Augmentation index as a measure of peripheral vascular disease state. *Current Opinions in Cardiology*, 17(5):543, 2002.

[29] M. Weir and E. Lerma. *Chronic Kidney Disease and Hypertension*. Humana Press, New York, United States, 2015.

[30] W. Nichols, M. O'Rourke, and C. Vlachopoulos. *McDonald's blood flow in arteries: theoretical, experimental and clinical principles*. Hodder Arnold, London, United Kingdom, 2011.

[31] M. Roman, A. Ganau, P. Saba, R. Pini, T. Pickering, and R. Devereux. Impact of Arterial Stiffening on Left Ventricular Structure. *Hypertension*, 36(4):489, 2000.

[32] B. Lorell and B. Carabello. Left Ventricular Hypertrophy:pathogenesis, detection, and prognosis. *Circulation*, 102(4):470, 2000.

[33] C. Grant, D. Brockwell, S. Radford, and N. Thomson. Tuning the elastic modulus of hydrated collagen fibrils. *Biophysical journal*, 97(11):2985, 2009.

[34] J. Davis. *Engineering the Bioelectronic Interface: Applications to Analyte Biosensing and Protein Detection*. RSC Publishing, Cambridge, United Kingdom, 2009.

[35] T. Kuznetsova, M. Starodubtseva, N. Yegorenkov, S. Chizhik, and R. Zhdanov. Atomic force microscopy probing of cell elasticity. *Micron*, 38(8):824, 2007.

[36] R. Mahaffy, C. Shih, F. MacKintosh, and J. Käs. Scanning probe-based frequency-dependent microrheology of polymer gels and biological cells. *Physical Review Letters*, 85(4):880, 2000.

[37] A. Mathur, G. Truskey, and W. Monty Reichert. Atomic Force and Total Internal Reflection Fluorescence Microscopy for the Study of Force Transmission in Endothelial Cells. *Biophysical Journal*, 78(4):1725, 2000.

[38] G. Giannakoulas, G. Giannoglou, J. Soulis, T. Farmakis, S. Papadopoulou, G. Parcharidis, and G. Louridas. A computational model to predict aortic wall stresses in patients with systolic arterial hypertension. *Medical Hypotheses*, 65(6):1191, 2005.

[39] I. Sneddon. The relation between load and penetration in the axisymmetric boussinesq problem for a punch of arbitrary profile. *International Journal of Engineering Science*, 3(1):47, 1965.

[40] S. Moreno-Flores, R. Benitez, M. dM Vivanco, and J. Toca-Herrera. Stress relaxation microscopy: Imaging local stress in cells. *Journal of Biomechanics*, 43(2):349, 2010.

[41] R. Raghu and I. Vignon-Clementel. Comparative study of viscoelastic arterial wall models in nonlinear one-dimensional finite element simulations of blood flow. *Journal of Biomechanical Engineering*, 133(8):81003, 2011.

Co-authorship Statement

Tissues resected from WKY and SHR were obtained from and cultivated by Prof. Reza Tabrizchi's research lab.

This M.Sc. work on viscoelastic response built upon prior data using a purely elastic model. The manuscript in Chapter 2 includes that data. This prior data was collected by Garrett McDougall (GM) as a B.Sc. student and by Shaykat Saha (SS) as a B.Sc. student.

About half of the elastic modulus data in Chapter 2, Figure 2.5 are previously published in GM's Honours Thesis. The remainder is original to this thesis. All analyses presented in this thesis are new and original.

Early imaging of the tunica intima and adventitia samples was completed during GM's Honours work under Prof. Merschrod with assistance from SS an undergraduate research assistant in Prof. Merschrod's group. SS also assisted with the gathering of elastic modulus data for these samples. Viscoelasticity data and all data related to cardiac tissues and the tunica media was gathered by myself during the course of my M.Sc.

A portion of the Raman spectra detailed in Appendix B were collected by or with the assistance of Katie Brown during her time as a MUCEP student in the group.

Finally, all chapters and appendices within this thesis have been written by myself with corrections and feedback from Profs. Merschrod and Tabrizchi. Likewise, all

experimental protocols and data collection not excepted above have been performed by myself. This also includes all data analysis.

Chapter 2

Hypertension Induced Elastic Dysfunction of Murine Aorta*

2.1 Introduction

Optimal elasticity in vasculature plays an imperative role in cardiac function and the delivery of blood throughout the body. [1] Accordingly, impaired arterial elasticity can be linked to increased left ventricular afterload, left ventricular hypertrophy (LVH), and subendocardial ischemia (hypoxia of the layer of tissue just below the endocardium) due to decreased coronary vascular perfusion and reserve. [2–4] Optimal coronary perfusion occurs when the wave reflection returns during late diastole or early systole. [5] Thus, increased arterial stiffness may offset the timing of wave reflections, and can consequently impair coronary perfusion and optimal myocardial blood flow. [6, 7] In addition, approximately half of the left ventricular stroke volume during systole is stored in conduit arteries (i.e. the thoracic and abdominal aorta), and the viscoelastic recoil of these vessels during diastole produces a continuous flow

*Probing hypertension induced nanoscale elastic and viscolelastic dysfunction of murine aorta by AFM, Garrett McDougall, Shaykat Saha, Reza Tabrizchi, Erika Merschrod, *Biophys J* in preparation

of blood throughout the peripheral vasculature. [8] This behaviour has been referred to as the Windkessel effect and it allows for continuous perfusion of tissues and organs.

Hypertension has been linked to dysfunctionality of the endothelial cell layers and the adventitial matrix of the vasculature. [9–11] Certainly, the adventitial matrix has been found to undergo drastic remodelling in hypertension. [12, 13] The tunica adventitia supports up to 25% of the vascular load normally and, in pathologies with increased pressure-loads, can provide nearly half of the necessary support. [14] Consequently, the tunica adventitia is of particular importance in investigating the mechanical effects of high intravascular pressure, i.e. hypertension. [15, 16] While the tunica intima has only a minor contribution to the bulk-scale mechanical behaviour of the aorta in a direct sense, it is responsible for the release of vasoactive substances from endothelial cells.These vasoactive substances are activated by mechanical processesses often relating to pressure and sheer. [17] Consequently, abnormal mechanical behaviour of the intima may significantly alter vascular tone through the release of vasoactive substances.

The importance of arterial elasticity in coronary perfusion and continued peripheral blood flow are well known, and the nanomechanical properties of arteries have been investigated in some detail in the normal state. [18–21] However, our current understanding of the relationship between arterial structure and the altered nanomechanical properties in the hypertensive case remains largely incomplete. [22] Here we have investigated the effects of hypertension on the nanoscale elasticity and viscoelasticity of the tunicas intima and adventitia of both the thoracic and abdominal aorta using a minimal nanoindentation AFM technique. It must be recognized that abnormal alterations in nanomechanical behavior of the larger blood vessels can manifest as stiffer arteries that could ultimately affect left ventricular afterload, coronary perfusion, and the normal perfusion of tissues and organs throughout the body.

2.2 Experimental

2.2.1 Aorta Sample Preparation

SHR and WKY rats (13-15 weeks old) from Charles River were anaesthetized with isoflurane (5% in 100% O_2; induction; treated with buprenorphine 0.01 mg/kg s.c.) and maintained under isoflurane (1.5- 2.0% in 100% O_2). Catheter (polyethylene tubing, I.D. 0.28 mm, O.D. 0.61 mm) was inserted into the femoral artery for systolic and diastolic blood pressure and heart rate measurements. Body temperature was maintained at 37 $\pm$ 1 °C using a heating lamp and monitored with a thermometer placed in the rectum. Arterial blood pressure was recorded with a pressure transducer (Gould Statham, USA; Model PD23B). The pressure transducers were connected to an amplifier (DA 100A) that, in turn, was linked to a universal interface module (UIM 100), which then interfaced with an acquisition unit (MP 100). The data was collected using AcqKnowledge III system. Heart rate was calculated from the blood pressure signal, with the aid of AcqKnowledge III system. Blood pressure and heart rate were monitored for 20-30 minutes. Each animal was then euthanized under anesthesia/analgesia by thoracotomy and thoracic aorta and abdominal aorta (below the kidneys) were removed. The blood vessels, once removed, were dissected free of fat and connective tissue at room temperature in Krebs buffer with the following composition (in mM): NaCl, 113; KCl, 4.6; glucose, 11; $MgCl_2$, 1.2; $CaCl_2$, 2.5; KH_2PO_4, 1.2; $NaHCO_3$, 25; EDTA, 0.1 and gassed with a 95% O_2 : 5% CO_2 gas mixture. Each blood vessel was cut into 3-4 mm in length, split open and placed in 0.02% sodium azide (NaN_3) phosphate buffer saline solution pH 7.4 for *in vitro* imaging studies.

Before imaging, all samples were adhered to glass microscope slides (Pearl, China; Cat No. 7101, roughened with a diamond stencil) using artificial tissue glue (Medtech

Global LLC, USA) selected to minimize changes in the mechanical properties of the sample. All slides were cleaned with 95% ethanol (v/v) solution after roughening and dried under N_2 before application of the tissue glue. The glue was allowed to set for 15 minutes. Sample hydration was maintained during this time by spotting of ultrapure water onto the en face side of the sample by Eppendorf pipette.

2.2.2 AFM Sample Preparation and Calibration

AFM images were obtained using an Asylum Research MFP-3D Atomic Force Microscope (California, USA) and silicon probes with gold-chromium coated tips (CSC37/Cr-Au, Mikromasch Inc.). A mean tip radius of 37 nm was reported by the manufacturer for the batch used (1117722).

Prior to all imaging the spring constant of the tip in air was determined by the thermal noise method. [23] An auto-tune was then performed with a target percentage of -5%. The tip was brought to near contact with the sample and ultrapure water added via Eppendorf pipette. The system was allowed to equilibrate for 15 minutes. Thermal calibration of the tip was performed once more in imaging medium. The tip was then tuned manually by manipulating the drive voltage to ensure an oscillation amplitude of 1.0 V.

2.2.3 Nanoscale Arterial Imaging

Scan sizes of 20 $\times$ 20 μm, 10 $\times$ 10 μm and 40 $\times$ 40 μm were used for both adventitial and intimal imaging. Scan size was decreased as necessary and as desired during analysis. All scans were performed in ultrapure water. Imaging was performed exclusively in tapping mode.

2.2.4 AFM Force Mapping

Prior to force mapping all tips were calibrated, in ultrapure fluid, on a glass mounted silicon wafer. A trigger force of 10.0 nN was used in combination with a z-velocity of 1.00 μm/s.

32 $\times$ 32 force mapping was performed using the CSC37/Cr-Au tips, as specified previously. Three sites for each sample (thoracic intima, thoracic adventitia, abdominal intima, and abdominal adventitia), for each rat were mapped. An xy tip velocity of 1.00 μm/s was used. A trigger force of 10 nN and a z-velocity of 1.00 μm/s were used.

Here determination of the elastic modulus has been conducted using the Hertz model as is often the case with biological samples. [24] Notably, For soft biological samples in contact with a parabolic indenter the Hertz model may be written as Equation 2.1,

$$F(\delta) = \frac{4\sqrt{R}}{3} \frac{E_{\text{sample}}}{1 - \nu_{\text{sample}}^2} \delta^{3/2} \tag{2.1}$$

Here $F(\delta)$ is the indentation force with R being the probe radius, $\nu_{sample}$the Poisson's ratio of the tissue (taken as 0.45), δ the indentation depth, and E_{sample} the elastic or Young's modulus of the tissue. [25] The Hertz model assumes that the indentation depth is significantly less than the sample thickness as is the case with minimal nanoindentation methods. Minimal nanoindentation also allows substrate effects to be ignored. [26] AFM-based methods allow for experiments of this nature but also provide topographical data. [27, 28]

2.2.5 AFM Creep Analysis

Viscoelastic creep measurements were taken using the same parameters as force mapping with the addition of a two second hold at the trigger force of 10 nN. Further indentation into the sample during the dwell phase is then observed. The Maxwell

model in question, Equation 2.2, is then applied to the resultant creep deformation vs. time plot, Figure 2.4 B. The model in question, Figure 2.1, is composed of two parallel Maxwell elements in series with a purely elastic spring.

$$\delta(t) = A_1 \exp\left(-\frac{t}{\tau_1}\right) + A_2 \exp\left(-\frac{t}{\tau_2}\right), \tau_i = \frac{\eta_i}{E_i} \tag{2.2}$$

Here τ_1 and τ_2 are the long and short term creep characteristic times. The bi-exponential behaviour of this process necessitates two time scales. A_1 and A_2 are fitting constants while η_i and E_i are the viscosity and compressive moduli respectively. The presence of bi-exponential behavior is consistent with hierarchical tissue behavior with local creep occurring on a shorter time scale and a regional or hierarchical creep behaviour on a longer time scale, similar behaviours have been observed in other collagen-based structures. [29–31] The distinction between τ_1 and τ_2 seen in Figure 2.8 is indicative of this behaviour. Moreover, it appears that hypertension increases the time scale of the short term characteristic while simultaneously reducing that of the long term. Incidentally, the amplitude of the indentation appears to have negligible effect on the measured time scales beyond 2 seconds of indentation as the indentation behaviour plateaus. This being said, the creep indentation is determined by change in indentation depth during the dwell phase.

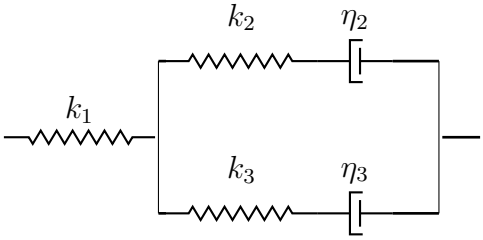

Figure 2.1: SLS model composed of two Maxwell elements in parallel with a purely elastic spring to describe two simultaneously occuring processes, representative of a hierarchical tissue behaviour.

2.3 Results

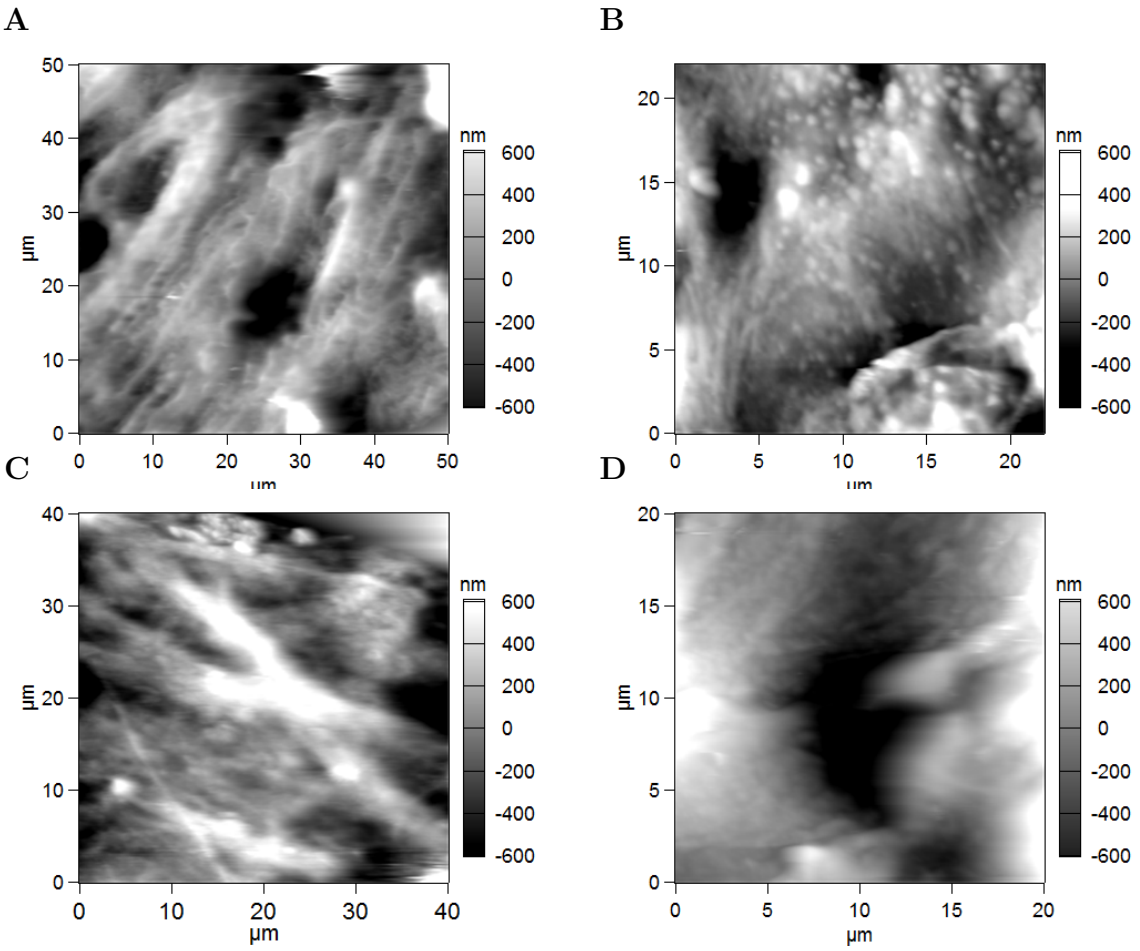

Figure 2.3: Representative AFM height images from each area of analysis. (A) Thoracic intima of the SHR featuring fenestrations (B) Abdominal intima of the WKY also featuring fenestrations and unidentified micro-polyp like structures (C) Thoracic adventitia of the SHR demonstrating significant fibril density (D) Abdominal adventitia of SHR with possible insertion point of *vasa vasorum* and periaortic fat.

2.3.1 Nanoscale Elasticity

The left panel in Figure 2.4 depicts a typical creep indentation experiment. During such an experiment, after the probe has come into contact with the sample, the applied force is increased gradually to a trigger force of 10 nN during the final portion of the

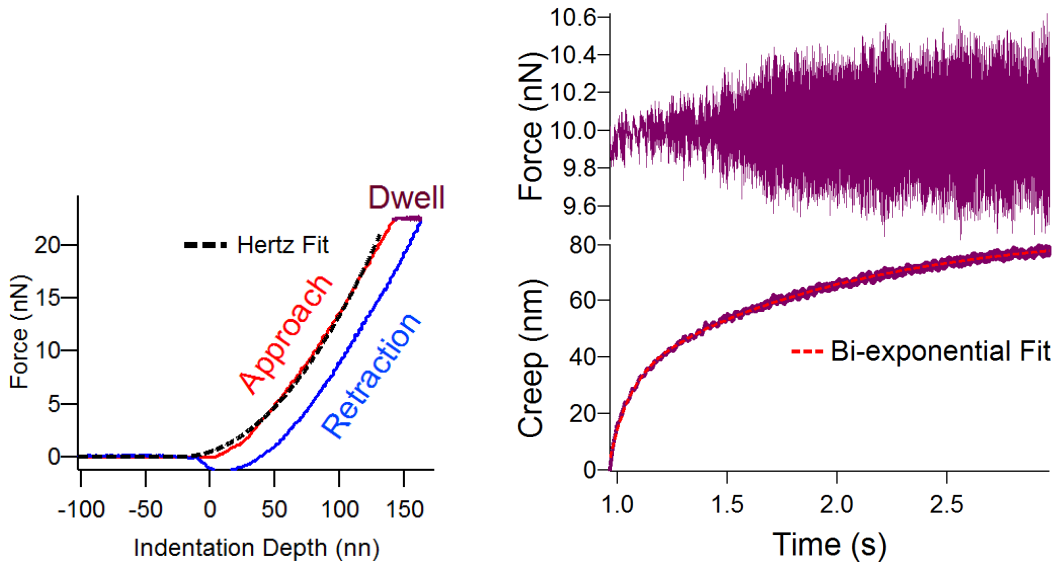

Figure 2.4: (A) Typical creep indentation force-spectroscopy experiment and (B) creep deformation observed during the dwell phase with corresponding force profile (B).

approach phase. This indentation within the elastic regime can be fit with the Hertz model to determine sample stiffness.

At the end of the approach phase the trigger force, 10 nN in this work, becomes the holding force and is maintained for 2 seconds. During this period the tip is considered to dwell on the sample. During the dwell phase the indentation can be observed as a function of time, Figure 2.4 (right). Finally, the tip is drawn away from the sample and the load on the tissue is removed.

Table 2.1: Elastic moduli and characteristic response times of phase I and phase II relaxation for the intimal tissues of SHR and WKY

Tissue	E (kPa)	Range (kPa)	Creep (nm)	τ_1 (s)	τ_2 (s)
WKY-TI	44.0	2.36-253.2	89.3	0.12±0.21	1.29±1.37
SHR-TI	77.9	10.4-698.3	66.4	0.11±0.05	0.94±0.76
WKY-AI	32.0	2.96-458.2	57.6	0.31±0.782	1.12±1.74
SHR-AI	55.6	6.41-583.4	25.3	0.35±0.953	1.28±1.54

†Indicates statistical equivalence

Two-way ANOVA with post-hoc Scheffe's test, performed in Igor Pro 7.11 (Wave-

Table 2.2: Elastic moduli and characteristic response times of phase I and phase II relaxation for the adventitial tissues of SHR and WKY

Tissue	E (kPa)	Range (kPa)	Creep (nm)	τ_1 (s)	τ_2 (s)
WKY-TA	337.9	7.77-4,913	156	0.32±0.67	2.29±3.24
SHR-TA	417.1	9.05-5,011	67.0	0.14±0.41	1.40±0.78
WKY-AA	302.3	7.08-1,840	57.1	0.15±0.41	1.20±1.60
SHR-AA	574.6	0.91-5,590	76.3	0.17±0.40	1.59±2.78

*Indicates statistical equivalence

Metrics), indicates statistically significant difference between all possible pairings shown in Figure 2.5 and for all others throughout this thesis unless otherwise indicated. It bears mentioning that, in many cases, standard deviations have been omitted in favour of the 10th and 90th percentile values identified as the range. Frequently, for force spectroscopy on biosamples we observe standard deviations much larger than the mean value. Consequently, standard deviations are used solely for statistical analysis. For all tissues, excepting the adventitia of the SHR, we find the mean elastic moduli of thoracic tissues to be greater than that of their abdominal counterparts. Mean elastic moduli and the corresponding ranges are provided in Table 2.1 & Table 2.2.

The elastic modulus of both adventitial and intimal SHR tissues is significantly greater than that of their WKY counterparts. Moreover, the elastic moduli spread of the SHR is greater than that of the WKY indicating that hypertension acts to heterogenize the tissues in question towards values of higher elastic modulus.

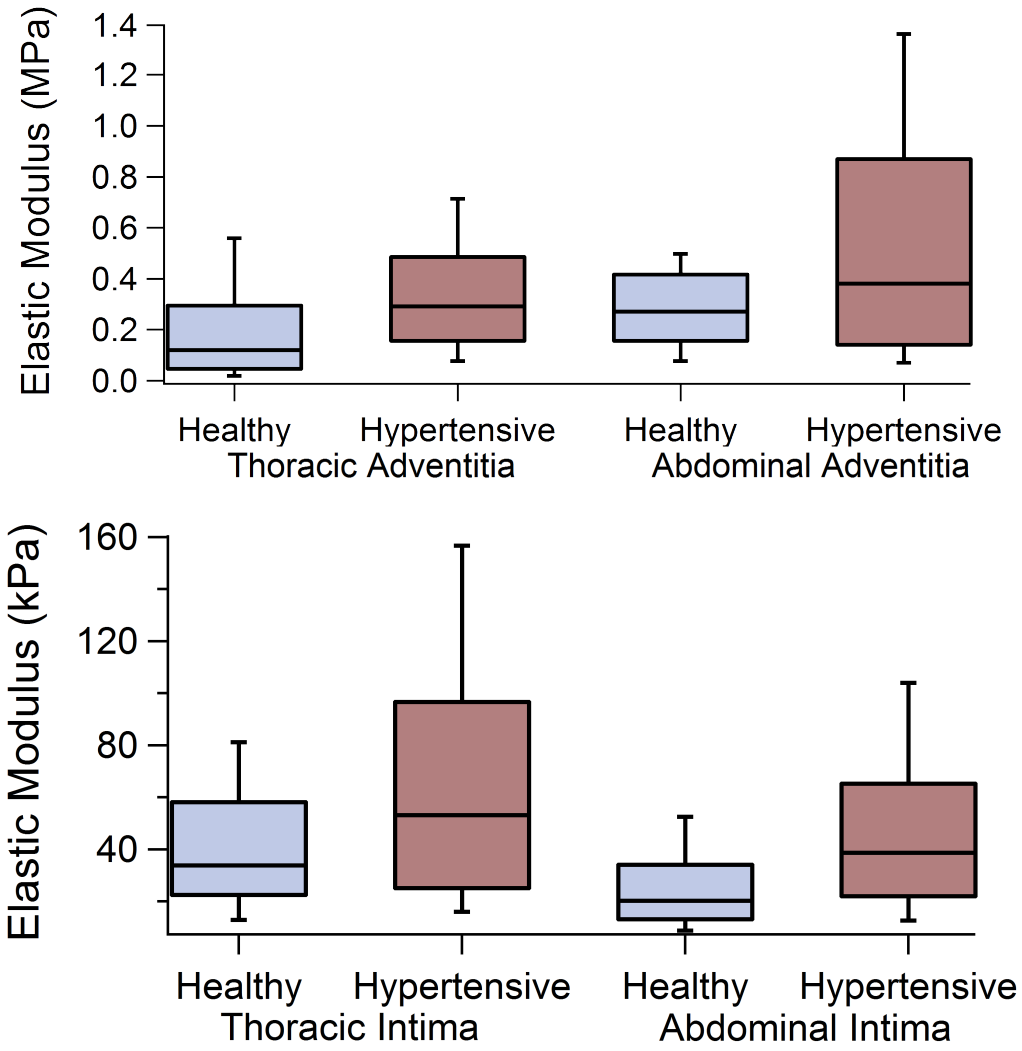

Figure 2.5: Box and whisker plots of elastic modulus for the tunica adventitia and the tunica intima, N=6000 for each box.

2.3.2 Creep Deformation and Characteristics

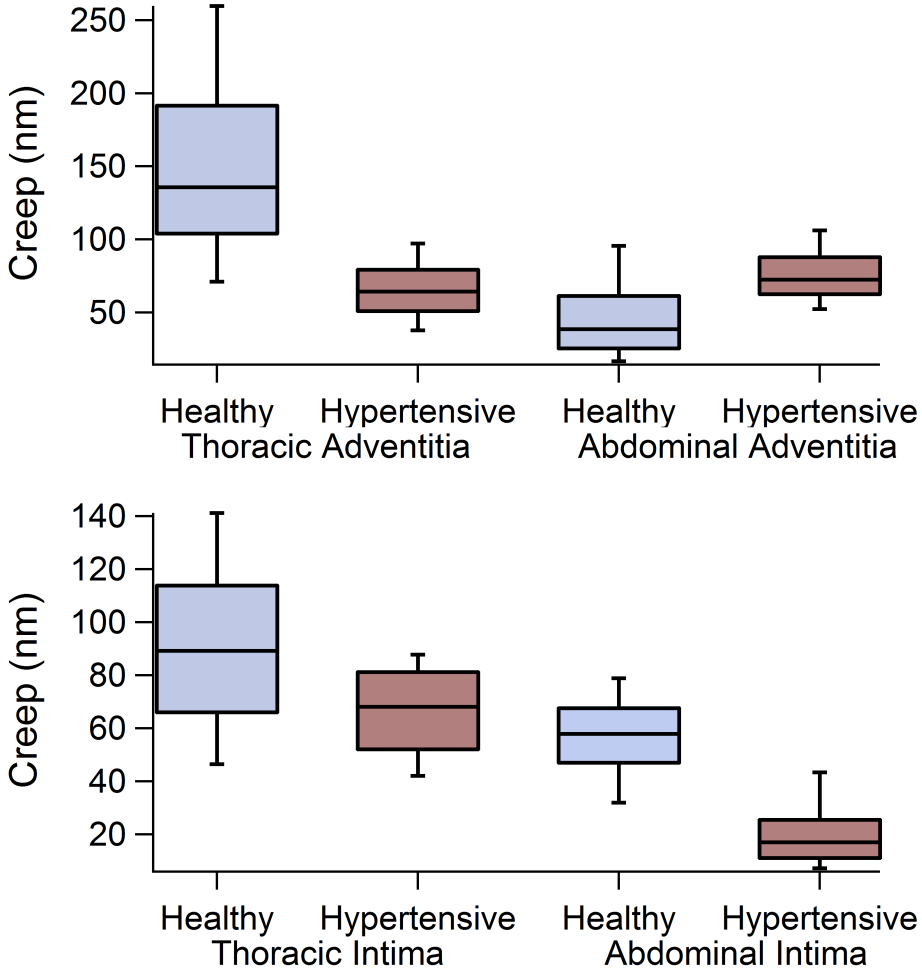

Figure 2.6: Box and whisker plots of creep deformation for the tunica adventitia and the tunica intima, N=6000 for each box.

While Grant and Twigg found creep deformation to be distributed log-normally in porcine tissues, we have found creep deformation to be distributed normally for healthy murine aortal tissues. [19] Other recent work has shown the progression of age-related viscoelastic changes in sheep aorta. [32] Figure 2.7 displays the greater visco-elastic creep undergone by the thoracic intima of the WKY (mean 88.2 nm) relative to the SHR (mean 66.4 nm). In Figure 2.6 both the intima and adventitia

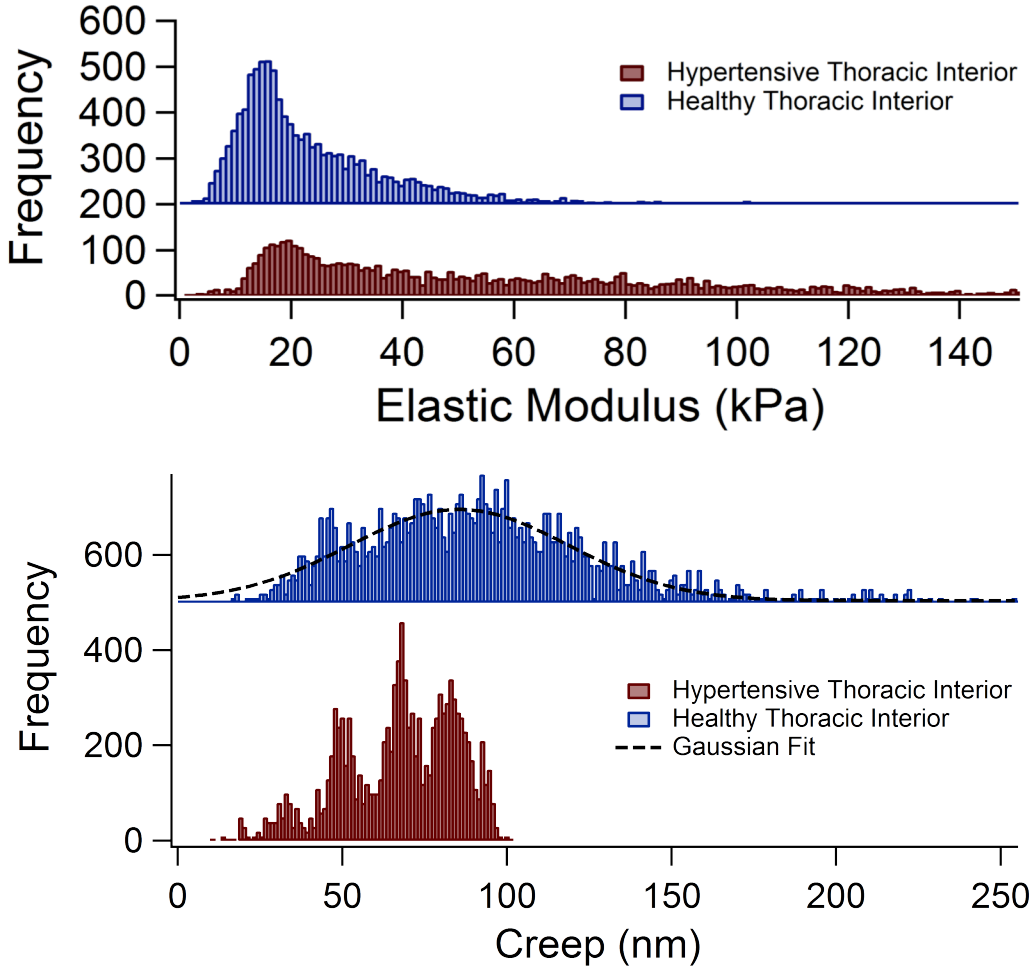

Figure 2.7: Creep deformation and elastic modulus histograms contrasting the tightly distributed behavior of the WKY thoracic intima with the skewness (right and left respectively) of the SHR analogue.

of the WKY thoracic aorta are seen to exhibit greater creep deformation than their SHR counterparts. Interestingly, the abdominal tissues demonstrate the opposite trend. In addition to investigating the magnitude of creep deformation we can also explore the time scale along which this deformation occurs. For a bi-exponential process like the one in question here, there are two relevant time scales. The time scale of each process is represented by its creep characteristic, τ. The first (or short term) creep characteristic, τ_1, represents the time it takes for 63.4% of the total creep

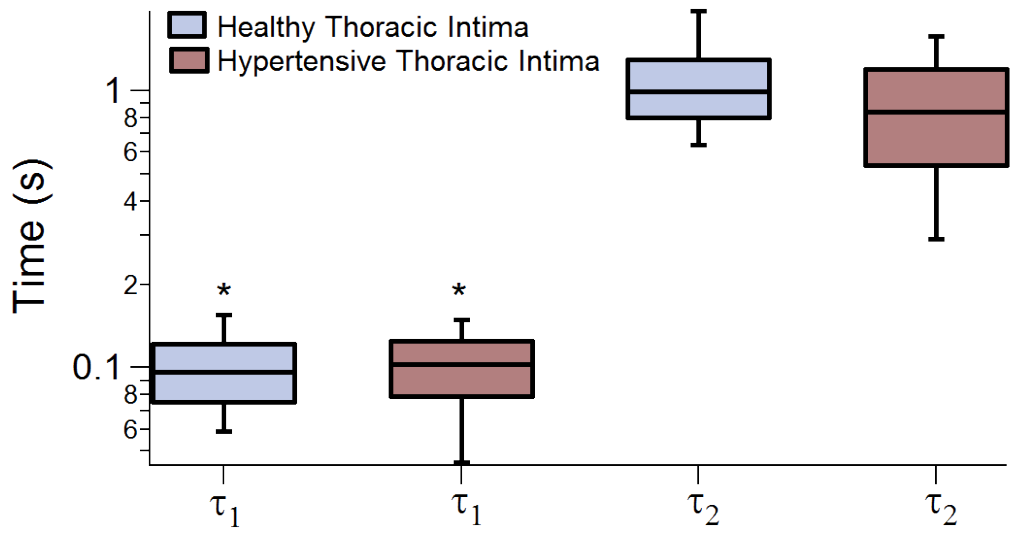

Figure 2.8: Box and whisker plots of characteristic creep times τ_1 and τ_2 for healthy and hypertensive thoracic intima, N=2500 for each box.

deformation to occur. This means that the remaining 36.6% of creep deformation is left to be represented by the second (or long term) creep characteristic, τ_2. These creep characteristics can be possibly thought of as being related to local and regional behaviours respectively. I.E. the primary determinant of τ_1 is the mechanical point-behaviour at the tip site where as τ_2 will also likely have significant contribution from tissue surrounding the indentation site and/or from underlying tissues layers and may be indicative of hierarchical behaviours.

Figure 2.8 introduces an obvious consistent trend for creep behaviour in these tissues. This trend relates to the relevant time scales of the two characteristics. τ_1 occurs on the scale of a tenth of a second with values distributed about 0.12 and 0. 11 s for the healthy and hypertensive animal respectively with no significant difference. Meanwhile, τ_2 takes approximately ten-times longer with distributions about 1.29 and 0.94 s for the healthy and hypertensive, respectively. This implies that the final 34% of accommodation occurs much more quickly in the hypertensive case. It is important to consider τ_1 and τ_2 in the context of the magnitude of creep deformation. For

instance, we have seen that hypertension greatly impairs the magnitude of deformation in the thoracic intima, Figure 2.6. However, the time-scale required for the first two thirds of this deformation to occur has not changed. This mean we that the rate of deformation has decreased as there is a lesser amount of deformation occurring on the same time-scale.

In the abdominal intima, Figure 2.9, we see that the relative ratio between τ_1 and τ_2 is roughly maintained with distributions about 0.310 and 0.353 s for healthy and hypertensive τ_1 and about 1.12 and 1.28 s for τ_2 for the same respective tissues. Interestingly we can see here that the faster relaxation process takes approximately three-times longer in the abdominal tissues than the thoracic tissues, for both the healthy and hypertensive case. Statistically significant differences between the healthy and hypertensive tissues present here for both τ_1 and τ_2. Interestingly, we see that the short-term process occurs faster while the long-term process seems to occur more slowly under the influence of hypertension.

Moving towards the adventitial layer we notice that ratios of τ_1 and τ_2 are roughly maintained with respective values and variances in Table 2.2. In the thoracic tissues, Figure 2.10, we observe notable "tightening" of the hypertensive distributions and an associated shortening of both the short-term and long-term relaxation processes. When we cross-reference these changes with those to creep we can conclude that a lesser degree of creep accommodation is induced by hypertension in the thoracic tissue but occurs at a faster relative rate for both the short and long-term accommodation.

Contrary to the shortening of the creep characteristics in the thoracic tissue, we see a lengthening in the abdominal adventitia. This may relate to the unusual behaviour seen in Figure 2.6, that is the increasing creep behaviour in the abdominal adventitia due to hypertension. We reasoned that this may be a compensatory alteration intended to "make up" for the loss of creep accommodation at the more proximal thoracic

tissue. This compensatory change seems to be associated with a lengthening of both characteristics. This means that we ultimately observe a more significant, longer accommodation process in the abdominal aorta.

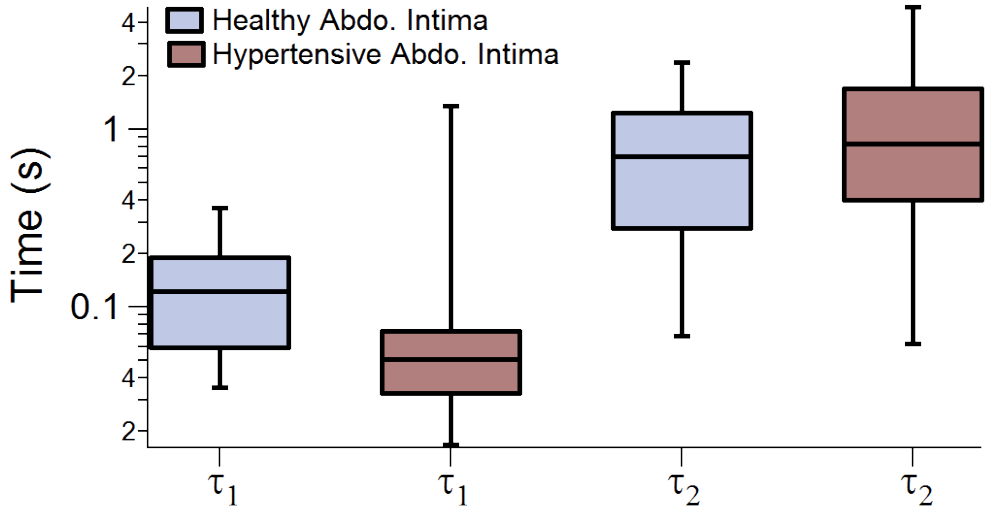

Figure 2.9: Log-scaled box and whisker plots of characteristic creep times τ_1 and τ_2 for healthy and hypertensive abdominal intima, N=2500 for each box.

2.4 Discussion

The greater elastic modulus of thoracic tissues relative to their abdominal counterparts is apparent in Figure 2.5. This is in following with the understanding that the circulatory system is composed of stiffer proximal vessels and more compliant, smaller distal vessels. [33] This multifarious stiffness plays a significant pathophysiological role such that the stiffer proximal arteries, specifically the aorta, function to dampen pressure waves originating from left ventricular ejection. For this reason, proximal arterial stiffness has long been understood to relate to left ventricular function. [34, 35]

Arterial compliance is dependent upon a number of factors including vascular tone, collagen and elastin composition, and even hydration within the vascular wall. Many

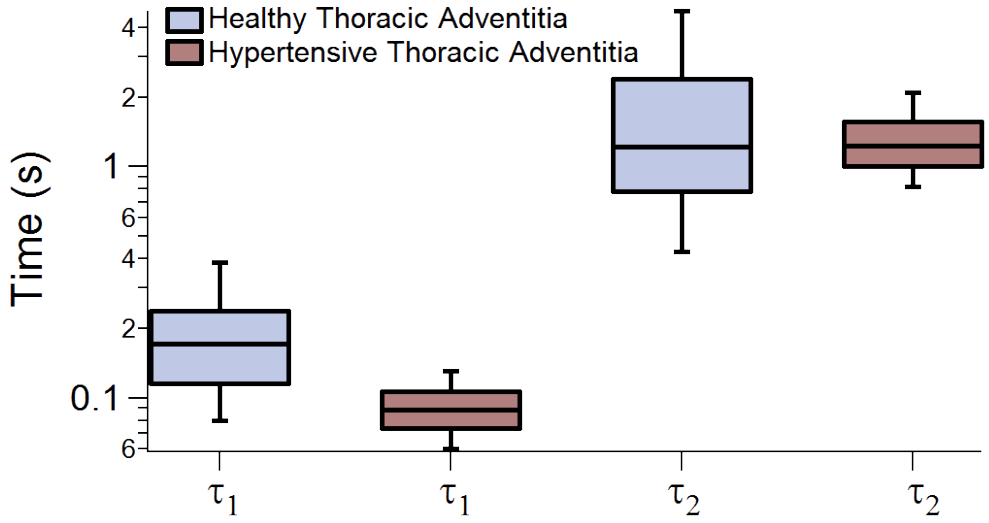

Figure 2.10: Box and whisker plots of characteristic creep times τ_1 and τ_2 for healthy and hypertensive thoracic adventitia, N=2500 for each box.

of these factors may change in response to increased pressure loads. [36] Considering this, the greater nanomechanical stiffness of the adventitial and intimal thoracic aorta tissues observed here precipitate from the greater pressure load experienced by these tissues relative to the abdominal tissues. This is the case in both the native and hypertensive states. For this reason, more proximal arterial tissues may provide better insight into the pathogenesis and effects of hypertension. However, contributions of the tunica media to macroscale arterial elasticity are non-negligible and require further investigation. [37] The work completed in Chapter 3 addresses this.

Figure 2.5 displays the nanoscale stiffening of tissues induced by hypertension. This stiffening has physiologically significant consequences, particularly in the proximal aorta. Here increased stiffness mitigates the ability of the aorta to dampen pulse waves and diminishes aortal distensibility. Decreased aortal expansion reduces the effectiveness of the Windkessel effect as a smaller volume of blood is retained to be released during diastole. From this it follows that hypertension may have serious implications for systemic and coronary perfusion related to the Windkessel effect.

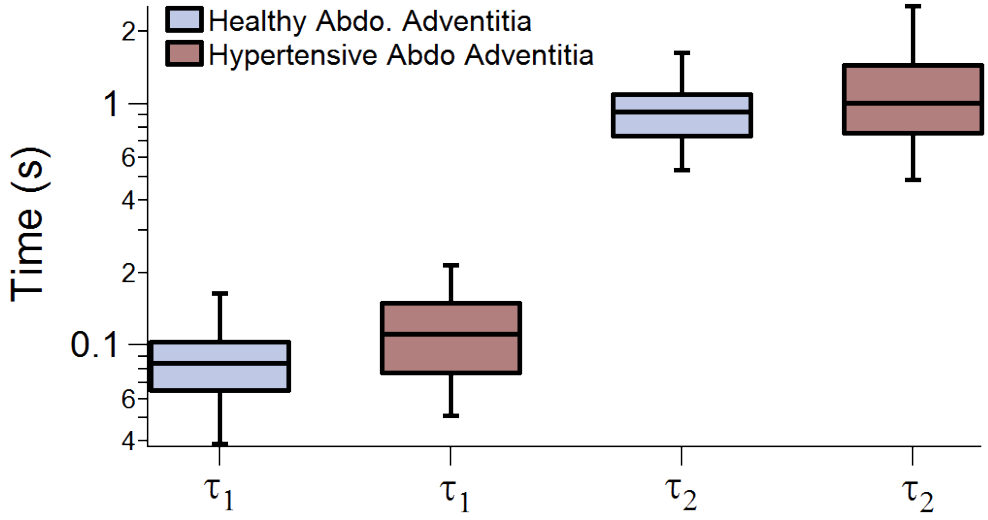

Figure 2.11: Box and whisker plots of characteristic creep times τ_1 and τ_2 for healthy and hypertensive abdominal adventitia, N=2500 for each box.

It also bears mentioning that there exist gross anatomical differences between the thoracic and abdominal aorta. For instance, the abdominal aorta has less collagen and elastin than the thoracic while also having a greater number of outlets which can affect fluid dynamics. [38] These differences may then affect the on-going biophysical changes occuring in response to a hypertensive state. Consequently, increased intravascular pressure may be expected to have differential effects on various segments of the arterial tree. This is a significant consideration as the behaviour of small arteries plays an important role in haemodynamics, particularly in the generation of wave reflections. [36]

While impaired arterial elasticity has immediate, intuitive consequences, those associated with altered arterial viscoelasticity are also significant. Arterial viscoelasticity plays a significant role in maintaining diastolic blood flow through the Windkessel effect. The presence of hysteresis in the range of indentation depths between 0 and 50 nm in Figure 2.4 A is indicative of the viscoelastic nature of these arterial tissues. [39]

The lesser viscoelastic creep of the SHR relative to the WKY (Figure 2.6), with

the exception of the abdominal adventitia, is indicative of a diminished capacity of the SHR to dissipate energy resulting from left ventricular contraction and also decreased Windkesselian behaviour. Importantly, this altered viscoelastic behaviour may offset wave reflection timing and consequently impair coronary perfusion. Viscoelastic behaviour of the abdominal aorta is of particular importance. Typically the abdominal aorta contributes to wave reflections which return to the proximal aorta during late systole. It is possible that dysfunctional viscoelastic relaxation time may result in wave reflections returning later in systole, thus increasing left ventricular afterload and interrupting coronary perfusion. Similarly, continued diastolic bloodflow may be affected due to the altered tissue relaxation times. This may have significant effects upon peripheral perfusion. Figure 2.7 demonstrates the left skewness in creep distribution induced by hypertension.

As mentioned, the abdominal adventitia of the WKY presents with a seemingly counter-intuitive finding. One argument for this may be based on the relationship between distal blood flow and the elastic and viscoelastic behavior of more proximal vessels. As discussed in Section 2.3.1, the thoracic aorta of the SHR, being of greater elastic modulus, has a diminished capacity to dampen pulse pressures. This diminished capacity results in greater pulse pressures in more distal vessels. Consequently, these distal vessels may adapt to improve their viscous dissipation of pulsatile energy and thus demonstrate higher degrees of viscoelastic creep.

Investigation of the creep characteristics indicate significant hypertensive changes to the time-scale of both the short and long-term accommodation processes in both the intimal and adventitial layers with the exception of the thoracic intimas short-term behaviour. Interestingly we observe differential responses along the two time scales, particularly in different tissues which have been discussed in the previous section on a case-wise basis. Generally, we find τ_2 to take approximately ten-times longer than τ_1.

Additionally, the counter-intuitive behaviour of the abdominal adventitia explained above seems to also present in the τ_1 and τ_2 data.

It must be noted that nanoscale materials behaviours may not necessarily correlate to bulk scale behaviours due to hierarchical effects. Likewise, variances in imaging solution may also alter the nanomechanical properties of these tissues. Particularly, the mechanical properties of collagen, a major structural component of arteries, may be altered. [40]

2.5 Conclusions

A minimal nanoindentation AFM technique has elucidated several mechanical distinctions both between and within tissue pathologies maintained in a state of hydration. The tunica adventitia has a nanoscale elasticity an order of magnitude less than that of the tunic intima. In a similar vein, the thoracic intima is significantly less elastic than the abdominal intima. This likely precipitates from load-induced stiffening of the thoracic intima. Likewise, hypertension has demonstrated a generalized nanoscale stiffening effect upon the tissues in question. Greater viscoelastic creep was observed in thoracic aorta tissues compared to those of the abdominal aorta. Moreover, impaired creep deformation was observed in hypertensive tissues indicating a decreased ability to dissipate pulsatile energy.

Bibliography

[1] J. Wagenseil, C. Ciliberto, R. Knutsen, M. Levy, A. Kovacs, and R. Mecham. Reduced vessel elasticity alters cardiovascular structure and function in newborn mice. *Circulation research*, 104(10):1217, 2009.

[2] M. Roman, A. Ganau, P. Saba, R. Pini, T. Pickering, and R. Devereux. Impact of Arterial Stiffening on Left Ventricular Structure. *Hypertension*, 36(4):489, 2000.

[3] B. Darne, X. Girerd, M. Safar, F. Cambien, and L. Guize. Pulsatile versus steady component of blood pressure: a cross-sectional analysis and a prospective analysis on cardiovascular mortality. *Hypertension*, 13(4):392, 1989.

[4] B. Lorell and B. Carabello. Left Ventricular Hypertrophy:pathogenesis, detection, and prognosis. *Circulation*, 102(4):470, 2000.

[5] M. Weir and E. Lerma. *Chronic Kidney Disease and Hypertension*. Humana Press, New York, United States, 2015.

[6] M. Safar. Pulse pressure in essential hypertension: clinical and therapeutical implications. *Journal of hypertension*, (7):769, 1989.

[7] W. Nichols, M. O'Rourke, and C. Vlachopoulos. *McDonald's blood flow in arteries: theoretical, experimental and clinical principles*. Hodder Arnold, London, United Kingdom, 2011.

[8] G. Belz. Elastic properties and Windkessel function of the human aorta. *Cardiovascular drugs and therapy*, 9(1):73–83, 1995.

[9] S. Prisco, J. Priestley, B. Weinberg, A. Prisco, M. Hoffman, H. Jacob, M. Flister, J. Lombard, and J. Lazar. Vascular dysfunction precedes hypertension associated with a blood pressure locus on rat chromosome 12. *American Journal of Physiology - Heart and Circulatory Physiology*, 307(8):H1103, 2014.

[10] M. Widlansky, N. Gokce, J. Keaney, and J. Vita. The clinical implications of endothelial dysfunction. *Journal of the American College of Cardiology*, 42(7):1149, 2003.

[11] K. Dharmashankar and M. Widlansky. Vascular endothelial function and hypertension: insights and directions. *Current hypertension reports*, 12(6):448, 2010.

[12] K. Stenmark, N. Davie, M. Frid, E. Gerasimovskaya, and M. Das. Role of the Adventitia in Pulmonary Vascular Remodeling. *Physiology*, 21(2):71, 2006.

[13] J. Ogeng'o, K. Ongeti, M. Obimbo, B. Olabu, and P. Mwachaka. Features of atherosclerosis in the tunica adventitia of coronary and carotid arteries in a black kenyan population. *Anatomy Research International*, 2014:456741, 2014.

[14] C. Schulze-Bauer, P. Regitnig, and G. Holzapfel. Mechanics of the human femoral adventitia including the high-pressure response. *American Journal of Physiology: Heart and Circulatory Physiology*, 282(6):H2427, 2002.

[15] S. Arribas, C. Hillier, C. González, S. McGrory, A. Dominiczak, and J. McGrath. Cellular aspects of vascular remodeling in hypertension revealed by confocal microscopy. *Hypertension*, 30(6):1455, 1997.

[16] C. Xu, C. Zarins, H. Bassiouny, W. Briggs, C. Reardon, and S. Glagov. Differential Transmural Distribution of Gene Expression for Collagen Types I and III Proximal to Aortic Coarctation in the Rabbit. *Journal of Vascular Research*, 37(3):170, 2000.

[17] M. Yanagisawa, H. Kurihara, S. Kimura, Y. Tomobe, M. Kobayashi, Y. Mitsui, Y. Yazaki, K. Goto, and T. Masaki. A novel potent vasoconstrictor peptide produced by vascular endothelial cells. *Nature*, 332(6163):411, 1988.

[18] T. Reichlin, A. Wild, Markus Dürrenberger, A. Daniels, U. Aebi, P. Hunziker, and M. Stolz. Investigating native coronary artery endothelium in situ and in cell

culture by scanning force microscopy. *Journal of Structural Biology*, 152(1):52, 2005.

[19] C. Grant and P. Twigg. Pseudostatic and dynamic nanomechanics of the tunica adventitia in elastic arteries using atomic force microscopy. *ACS nano*, 7(1):456, 2013.

[20] A. Lundkvist, E. Lilleodden, W. Siekhaus, J. Kinney, L. Pruitt, and M. Balooch. Viscoelastic properties of healthy human artery measured in saline solution by AFM-based indentation technique. *Thin Films: Stresses and Mechanical Properties VI*, 436:353, 1997.

[21] J. Beenakker, B. Ashcroft, and T. Lindeman, J.and Oosterkamp. Mechanical properties of the extracellular matrix of the aorta studied by enzymatic treatments. *Biophysical journal*, 102(8):1731, 2012.

[22] J. Peloquin, J. Huynh, and R. Williams. Indentation measurements of the subendothelial matrix in bovine carotid arteries. *Journal of Biomechanics*, 44(5):815, 2011.

[23] J. Hutter and J. Bechhoefer. Calibration of atomic-force microscope tips. *Review of Scientific Instruments*, 64(7):1868, 1993.

[24] T. Kuznetsova, M. Starodubtseva, N. Yegorenkov, S. Chizhik, and R. Zhdanov. Atomic force microscopy probing of cell elasticity. *Micron*, 38(8):824, 2007.

[25] G. Giannakoulas, G. Giannoglou, J. Soulis, T. Farmakis, S. Papadopoulou, G. Parcharidis, and G. Louridas. A computational model to predict aortic wall stresses in patients with systolic arterial hypertension. *Medical Hypotheses*, 65(6):1191, 2005.

[26] A. Mathur, G. Truskey, and W. Monty Reichert. Atomic Force and Total Internal Reflection Fluorescence Microscopy for the Study of Force Transmission in Endothelial Cells. *Biophysical Journal*, 78(4):1725, 2000.

[27] G. Binnig and C. Quate. Atomic Force Microscope. *Physical Review Letters*, 56(9):930, 1986.

[28] D. Abramovitch, S. Andersson, L. Pao, and G. Schitter. A Tutorial on the Mechanisms, Dynamics, and Control of Atomic Force Microscopes. In *2007 American Control Conference*, page 3488. IEEE, 2007.

[29] Z. Shen, H. Kahn, R. Ballarini, and S. Eppell. Viscoelastic properties of isolated collagen fibrils. *Biophysical Journal*, 100(12):3008, 2011.

[30] S. Moreno-Flores, R. Benitez, M. dM Vivanco, and J. Toca-Herrera. Stress relaxation microscopy: Imaging local stress in cells. *Journal of Biomechanics*, 43(2):349, 2010.

[31] C. Üzüm, J. Hellwig, N. Madaboosi, D. Volodkin, and R. von Klitzing. Growth behaviour and mechanical properties of PLL/HA multilayer films studied by AFM. *Beilstein Journal of Nanotechnology*, 3(1):778, 2012.

[32] R. Akhtar, H. Graham, B. Derby, M. Sherratt, A. Trafford, R. Chadwick, and N. Gavara. Frequency-modulated atomic force microscopy localises viscoelastic remodelling in the ageing sheep aorta. *Journal of the Mechanical Behavior of Biomedical Materials*, 64(2):10, 2016.

[33] S. Laurent, J. Cockcroft, L. Van Bortel, P. Boutouyrie, C. Giannattasio, D. Hayoz, B. Pannier, C. Vlachopoulos, I. Wilkinson, and H. Struijker-Boudier. Expert consensus document on arterial stiffness: methodological issues and clinical applications. *European Heart Journal*, 27(21):227, 2006.

[34] C. Tsao, A. Lyass, M. Larson, D. Levy, N. Hamburg, J. Vita, E. Benjamin, G. Mitchell, and R. Vasan. Relation of Central Arterial Stiffness to Incident Heart Failure in the Community. *Journal of the American Heart Association*, 4(11):2189, 2015.

[35] M. Safar, B. Levy, and H. Struijker-Boudier. Current Perspectives on Arterial Stiffness and Pulse Pressure in Hypertension and Cardiovascular Diseases. *Circulation*, 107(22):2864, 2003.

[36] G. McVeigh, A. Bank, and J. Cohn. Arterial Compliance. In *Cardiovascular Medicine*, pages 1811–1831. Springer London, London, United Kingdom, 2007.

[37] K. Hayashi. Mechanical Properties of Soft Tissues and Arterial Walls. In *Biomechanics of Soft Tissue in Cardiovascular Systems*, pages 15–64. Springer Vienna, Vienna, Austria, 2003.

[38] J. Homeister and M. Willis. *Molecular and translational vascular medicine*. Humana Press, New York, United States, 2012.

[39] Marc A. Meyers and Krishan Kumar Chawla. *Mechanical behavior of materials*. Cambridge University Press, 2009.

[40] C. Grant, J. McKendry, and S. Evans. Temperature dependent stiffness and visco-elastic behaviour of lipid coated microbubbles using atomic force microscopy. *Soft Matter*, 2012.

Chapter 3

Nanomechanical Viscoelastic Characterization of Normotensive and Hypertensive Murine Tunica Media

3.1 Introduction

Chapter 2 has demonstrated that the nanomechanical contribution of the tunica adventitia to nanoscale arterial wall stiffness is significantly greater than that of the tunica intima. The same trend has been observed on the bulk scale. [1] Likewise, the contribution of the muscular tunica media to the elastic behaviour of the vascular wall is considerable on the bulk scale. While no significant bulk scale differences in elasticity between the media and adventitia have been determined, the media has been demonstrated to be fourfold stiffer than the intima in uniaxial testing. [2] Additionally, when considering the vascular wall as a hierarchical material it is essential

that viscoelastic properties of the differential layers be determined in order to allow proper consideration of intra and inter-layer hierachical behaviours. Particularly, it may be that at very large or very small pressure loads one layer predominates in terms of arterial behaviour.

Hypertension has been found to induce two major alterations within the tunica media, which may bring about nanomechanical changes. [3] Firstly, a hypertension based increase in synthetic activity of medial VSMCs likely results in impaired elastin synthesis and a concurrent up-tick in collagen. Particularly, the preferential formation of the more elastic Type I collagen has been seen to shift to Types IV and V with no change in the ratio of Type III. [4] These Type IV and V collagens are localized to the VSMCs and are fibrillar collagens, meaning they are involved heavily in formation of larger fibril structures and have also been biochemically connected to fibrous plaques. [5] Secondly, increased arterial thickness is a hallmark characteristic of hypertension and strongly related to increased bulk arterial stiffness. The largest degree of arterial thickening occurs in the tunica media as a function of VSMC hyperplasia. Particularly, this thickening can occur to such an extent that the peripheral media may become hypoxic and undergo subsequent stiffening. This phenomena would produce two-fold stiffening of the arterial wall, firstly as a result of increased intima-media thickness and secondly as a result of hypoxic stiffening. [6, 7]

The findings in Chapter 2 bring forth the idea that impaired Windkesselian behaviour may be a significant detriment associated with altered arterial viscoelasticity for reasons discussed in 1.2. Traditionally, this behaviour has been thought to be passive in nature. [8, 9] However, within recent years, "muscle islands" have been described in the tunica media of various species. It has been postulated that these "islands" likely supplement passive Windkesselian behaviour and also serve to strengthen the aortic wall. [10, 11] The co-localisation of these islands with vasa vasora and adrenergic

nerve terminals suggests that there may be a periodicity to their muscular contraction. Local contracticle behaviour of these islands would significantly increase the strength of the vascular wall and may augment Windkesselian recoil. Aside from any possible active muscular contributions, the tunica media still provides a significant passive contribution to vascular strength and viscoelastic behavior while also being the primary determinant of vascular tone as suggested by its sympathetic innervation.

This chapter details the previously unknown nanomechanical properties of the tunica media. In particular, the nanoscale elastic modulus as well as viscoelastic creep and relaxation have been determined under fluid conditions for the thoracic and abdominal aortas in both the hypertensive and normotensive case.

3.2 Experimental

3.2.1 Tunica Media Sample Preparation

Tunica media samples were initially prepared as described in 2.2.1. Then, each blood vessel was cut into 3-4 mm in length, split open and the tunica intima removed through luminal scraping. The samples were then placed in 0.02% sodium azide (NaN_3) phosphate buffer saline solution pH 7.4 for *in vitro* imaging studies.

Before imaging, all samples were adhered to glass microscope slides (Pearl, China; Cat No. 7101, roughened with a diamond stencil) using artificial tissue glue (Medtech Global LLC, USA) selected to minimize changes in the mechanical properties of the sample. All slides were cleaned with 95% ethanol (v/v) solution after roughening and dried under N_2 before application of the tissue glue. The glue was allowed to set for 15 minutes. Sample hydration was maintained during this time by spotting of ultrapure water onto the en face side of the sample by Eppendorf pipette.

3.2.2 AFM Sample Preparation and Calibration

AFM calibration and sample preparation were completed as detailed in Sections 2.2.2 and 2.2.3 respectively.

3.2.3 AFM Force Spectroscopy and Analysis

AFM force mapping was completed as detailed in Section 2.2.4 with the exception of mapping being completed 20×20 to better sample the tissue. This greater number of sampling sites is a step towards mitigating sampling bias common in AFM force spectroscopy studies. Once again, Hertzian analysis has been used to determine the elastic modulus, E and creep analysis has been conducted as described in Section 2.2.5.

Two-way ANOVA with post-hoc Scheffe's test, performed in Igor Pro 7.11 (WaveMetrics) have been conducted on all data presented in this chapter. All results have statistically significant differences unless otherwise indicated.

3.3 Results and Discussion

3.3.1 Nanoscale Topography of the Tunica Media

Figure 3.1 depicts the representative topography of both the healthy and hypertensive thoracic tunica media. Interestingly, the healthy thoracic media has nodule-like features on a similar size-scale to the "microvesicle" structures observed on the healthy tunica intima during my honours work. This raises the possibility that the previously seen "microvesicles" may actually be a hierarchical manifestation of these structures seen here in the healthy tunica media. In the hypertensive tissue there is an obvious large density of collagen. This confirms that we are in fact seeing collagen infiltration

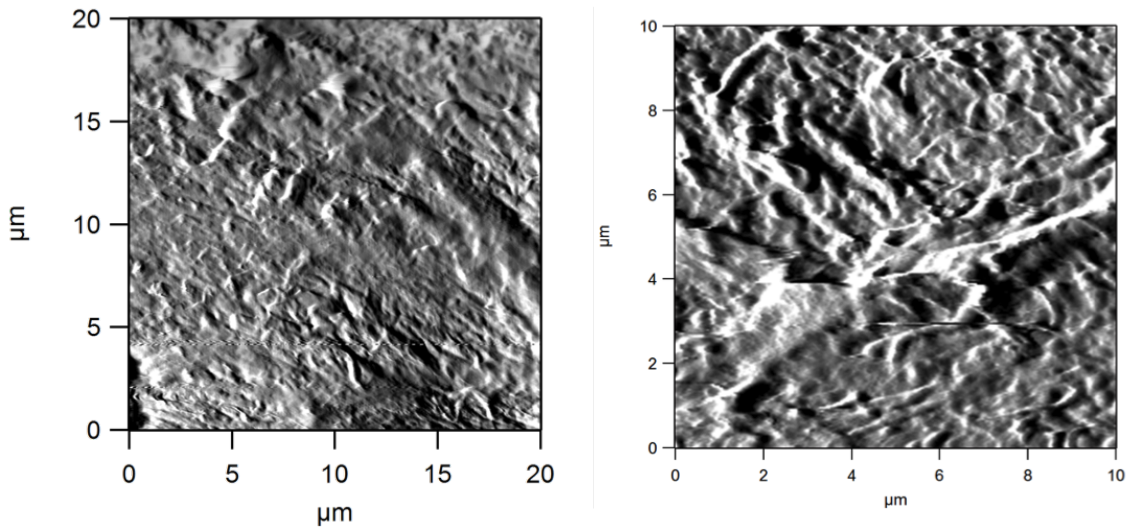

Figure 3.1: Amplitude images of healthy thoracic tunica media (left) and hypertensive thoracic tunica media (right) with readily apparent collagen.

from the sub-endothelial layer into the intima with the progression of hypertension as described in Figure 1.2. For the sake of brevity, all other topographical images from the tunica media have been excepted from this thesis. The images in Figure 3.1 and Figure 3.2 are representative and depict both of the aforementioned conclusions that we have drawn.

In the abdominal media, Figure 3.2, more "micropolyp" like structures seem to be present for the WKY specimens. Otherwise, there seems to be no other significant structural features in the healthy tissue. However, in the hypertensive tissues we observe what would appear to be fibril like structures that might also relate to collagen infiltration. Additionally, a few ellipsoidal structures about 8 μm long by 5 μm wide are present. Unfortunately, it is unlikely that these structures are VSMCs which have been reported to be in excess of 50 μm long in neonate SHR vasculature. [12] Another possibility would be for these structures to be the beginnings of atheromatous plaques. [13] These plaques often arise from pressure-induced damage to the arteries composed of lipids, cell debris, collagens, VSMCs, and many other components.

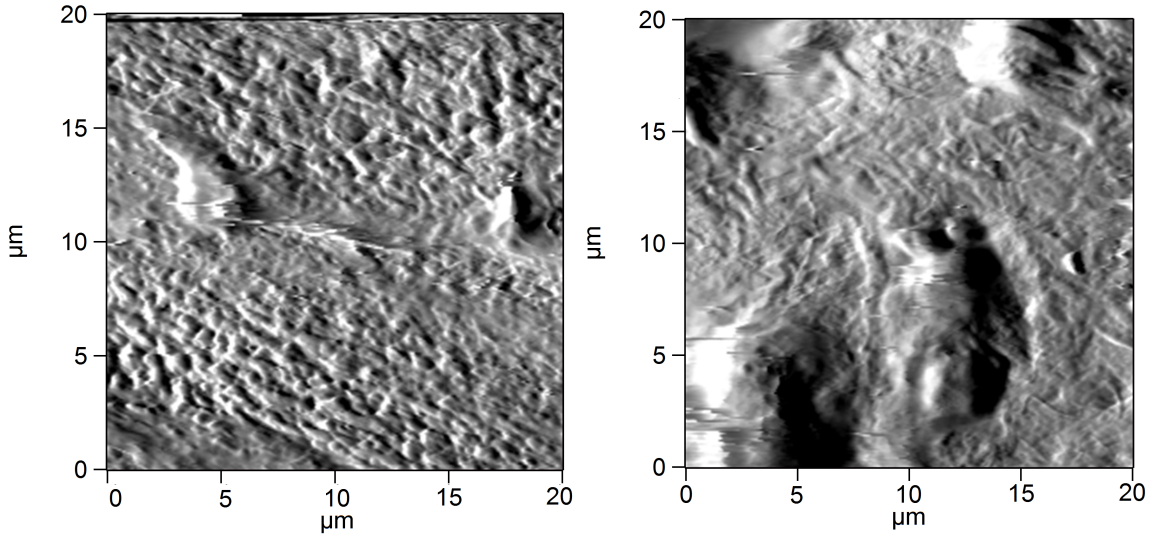

Figure 3.2: Amplitude images of healthy abdominal tunica media (left) and hypertensive thoracic tunica media (right) with greater collagen density and ellipsoidal structures apparent.

3.3.2 Nanoscale Elasticity of the Tunica Media

To allow for a comprehensive comparison of nanoscale elastic properties, force mapping was performed on both the thoracic (proximal) and the abdominal (distal) aorta. Force mapping locations were also incident with imaging sites to allow for correlation of mechanical properties to structures where appropriate.

Figure 3.3 depicts the native elasticity of the thoracic and abdominal tunica media. Firstly, it is worth noting that, in healthy medial tissues, the elasticity is on an order of magnitude with the intima. This relatively small elastic modulus would be suggestive of significant compliance of the tunica media which is in following with prior work suggesting that the tunica adventitia provides the majority of resistance to arterial distension. [1] Here we see that the abdominal media, having a mean elastic modulus of 23.7 kPa vice 12.9 kPa in the thoracic counterpart, is significantly less elastic. This follows the trend observed during my honours work and is discussed to some extent in Chapter 2. The working synopsis here is that thoracic tissues, being closer to

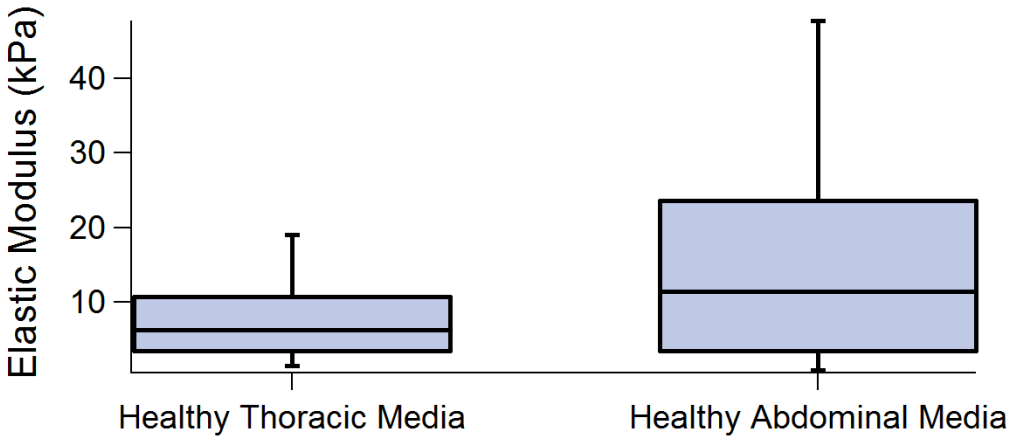

Figure 3.3: Box and whisker plots of elastic modulus for the thoracic and abdominal tunica media in the healthy case demonstrating lesser elasticity of the abdominal media. N=8000 for each box.

the heart, experience much larger pulse pressures due to left ventricular contraction and, consequently, must deal with dissipating the energy of these contractions. If these proximal vessels lacked of significant elasticity then they would be incapable of mitigating the exposure of distal tissues (such as the kidneys) to high pressures and would also incur much more damage themselves.

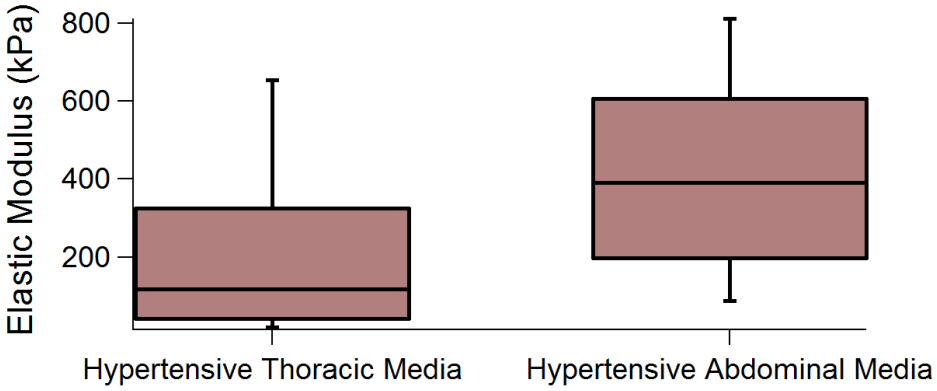

Figure 3.4: Box and whisker plots of elastic modulus for the thoracic and abdominal tunica media in the hypertensive case demonstrating lesser elasticity of the abdominal media N=8000 for each box.

The same trend of increased abdominal media stiffness relative to the thoracic media also holds in the hypertensive case, Figure 3.4. Consequently, the hypertensive thoracic media is still largely responsible for the dissipation of pulsatile pressure waves. Most significant, however, is the more than 10-fold increase in elastic modulus of these tissues with the healthy tissues increasing from 12.9 kPa to 235 kPa and from 23.7 kPa to 477 kPa in the hypertensive thoracic and abdominal media respectively. This degree of stiffening is unprecedented in comparison to our prior findings for the intima and adventitia which, generally, experience less than a 2-fold increase in elastic modulus. This finding provides nanomechanical evidence to argue against the traditional understanding that the tunica adventitia is the site of the most significant hypertensive remodelling under the influence of hypertension. [14] Here we see nanoscale stiffening occurring to such a degree that the hypertensive media has elastic moduli very similar to those of the hypertensive adventitia, while the healthy media much more closely resembles the healthy tunica intima. The combined stiffness of the hypertensive adventitia and media compared to their healthy counter parts will produce a greatly stiffened vessel even prior to consideration of additional compounding factors such as hierarchical changes. This dramatic stiffening, requiring log-scaling of the elasticity, which can be observed in Figure 3.5 implies a few things. To begin, the data presented in this section completes a comprehensive elastic profile of the thoracic and abdominal aorta where the following have been observed:

1. The adventitia is the most inelastic layer in both the native and hypertensive case, as is expected.

2. The intima and media have elasticity on the same order of magnitude in the healthy case.

3. Thoracic tissues are more elastic than their abdominal counterparts.

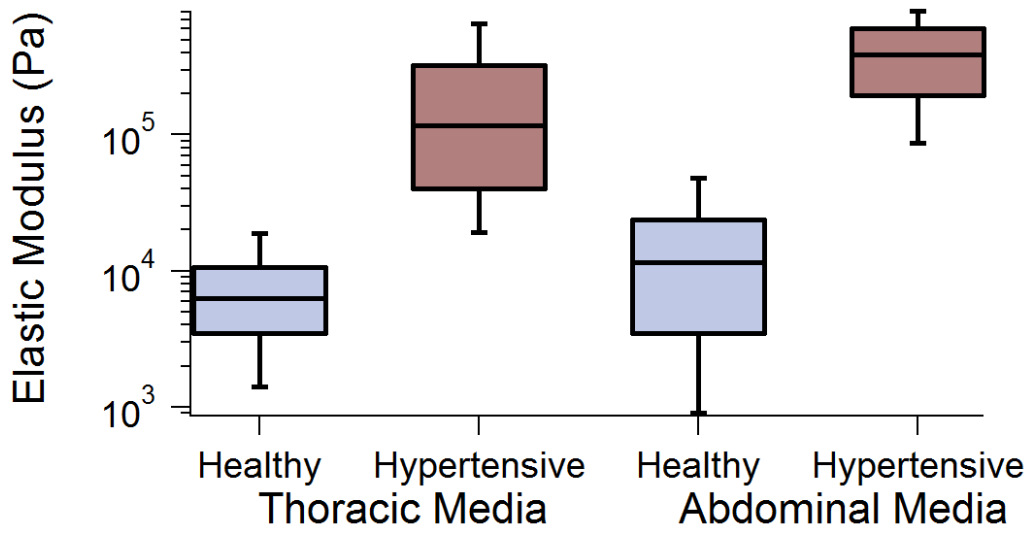

Figure 3.5: Box and whisker plots of elastic modulus for the thoracic and abdominal tunica media both in the hypertensive and healthy case, N=8000 for each box.

4. Stiffening occurs across the differential arterial layers (intima, media, and adventitia).

5. The intima and media undergo a near two-fold hypertensive increases in elastic modulus while the media experiences greater than a ten-fold increase.

Given these findings, the data presented here for the tunica media contribute to the same arguments provided for the intima and adventitia. In order to remain specific to the data at hand, we can now reason that hypertension produces dramatic stiffening of the tunica media. This stiffening represents diminished compliance of the aorta as a whole which is detrimental for a few primary reasons. Namely, this represents an increase in left ventricular afterload, increased likelihood of damage to the aorta itself (ultimately resulting in cyclical stiffening and potentially aneurysm and subsequent rupture), and impaired energy dissipation.

Increased afterload means that the left ventricle will have to generate more force in order to eject blood into the systemic circuit. This is a large factor in the development

of left ventricular hypertrophy, a common manifestation of hypertensive heart and a risk factor for many further complications itself. [15] This relationship is largely the impetus for the work conducted in Chapter 4 and is examined in greater detail there.

The relationship between arterial stiffening and increased blood pressure is inherently difficult to deconvolute. Often this relationship is described as a vicious cycle whereby increased pressures damage the arteries and causes arterial stiffening. Arterial stiffening then results in a decreased distensibility of the artery which limits the potential space available for a volume of blood to occupy which means the pressure must increase. This creates something of a "chicken or the egg" situation. [16] Beyond this, however, is the competing hypertensive remodelling behaviour of pronounced arterial dilation which, in late-stage remodelling, counteracts the stiffening and slows or ceases the gradual increase in pulse-pressures due to hypertension. [17] This being said, the net effect of hypertension induced arterial stiffening is a positive-feedback loop where further stiffening causes increased blood pressures which restarts the cycle.

Finally, impaired ability to decrease pulsatile energy at a more proximal locale will result in exposure of distal tissues and organs, not designed to endure significant stress, to strengthened pressure waves. One common complication is hypertensive retinopathy where damage to the retinal vasculature occurs due to hypertension and may ultimately result in loss of vision. [18] In the kidneys high blood pressure may cause damage to the vasculature, the glomeruli (a filitration apparatus), and to the tubules (the distilling and concentrating apparati of the kidneys). [19, 20] Often hypertensive nephropathy will require haemodialysis and associated morbidity and mortality are high.

3.3.3 Nanoscale Creep Deformation of the Tunica Media

The media exhibits notable bulk-scale heterogeneity in terms of its composition but, at the same time, seems to be fairly homogenous in its bulk scale mechanical

behaviour. [21, 22] To date it is unknown whether this mechanical homogeneity also extends to the nanoscale. Additionally, it has been postulated that the majority of an arteries viscoelastic potential should derive from the tunica media due to its high content of VSMCs intertwined with elastin. As such we could expect the media to act as the primary inhibitor of vascular distension and viscoelastic creep until such a point that distension becomes so significant that adventitial resistence becomes necessary in order to prevent over-stretching of the artery. [1]

The importance of the viscoelastic Windkessel effect discussed extensively in Section 1.2 and the suggestion that the media is the primary source of arterial viscoelasticity makes it an area of particular interest for creep analysis. Interestingly, upon comparing the medial viscoelastic data shown in Figure 3.8 with that of the intima and adventitia represented in Figure 2.6 it is apparent that medial creep deformation occurs on a notably smaller magnitude than the other arterial layers. If this finding scales to the bulk, it would imply that the media does not allow for the most viscoelastic deformation as some might assume but rather is involved with limiting the overall viscoelastic arterial deformation. Particularly, without the lesser viscoelastic deformation of the media, the artery as a whole would be limited then by the adventitia which would allow for more than a two-fold increase in viscoelastic accommodation. Such significant deformation may be sub-optimal in terms of Windkesselian behaviour, energy dissipation, and continued forward blood flow during diastole. This may be analogous to the Frank-Starling rule which governs optimal cardiac fibre extension for contraction. [23] If this is in fact the case then we should be particularly concerned with how hypertension affects the media as it will likely be representative of how hypertension alters the viscoelastic behaviour of the artery as a whole.

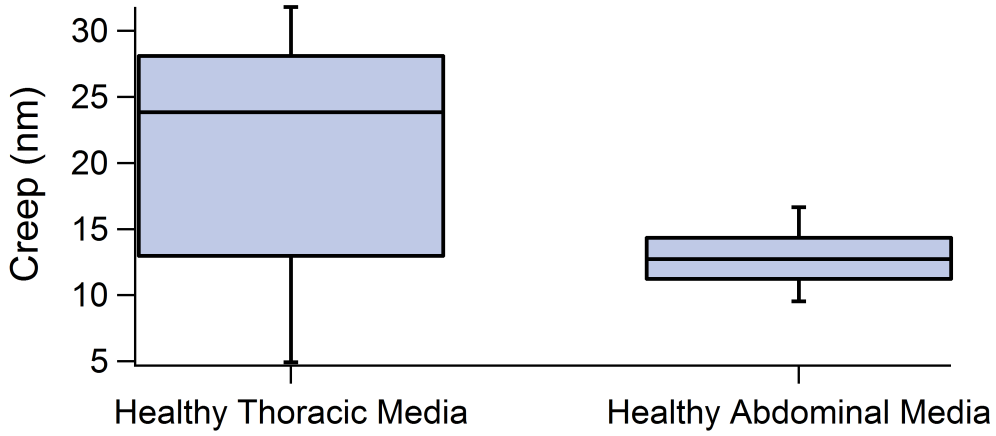

Figure 3.6: Box and whisker plots of creep deformation for the tunica media of the thoracic and abdominal aorta in the healthy case demonstrating lesser elasticity of the abdominal media N=8000 for each box.

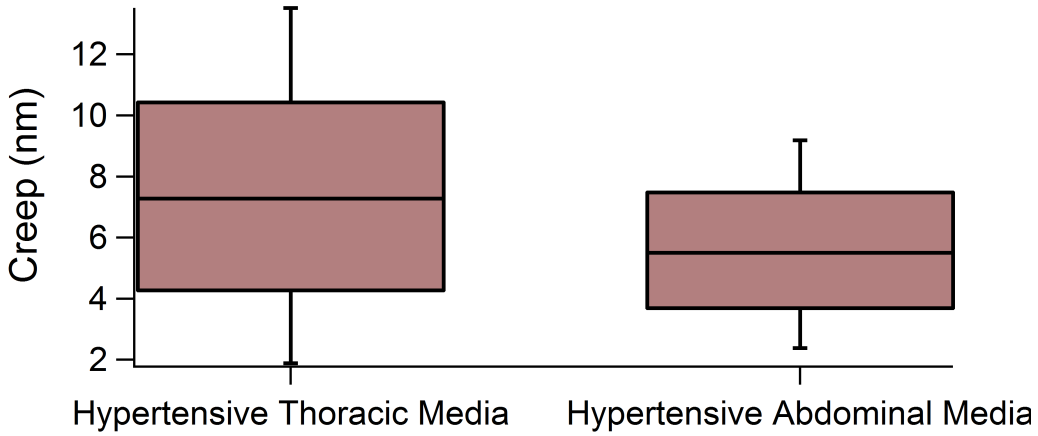

Figure 3.7: Box and whisker plots of creep deformation for the tunica media of the thoracic and abdominal aorta in the healthy and hypertensive case, N=8000 for each box.

As can be seen in Figure 3.6 and Figure 3.7 there is a trend in creep deformation analogous to what was observed in terms of elasticity. The thoracic tissues in both the healthy and hypertensive case exhibit significantly more creep deformation which is representative of a better ability to dissipate energy, continue diastolic bloodflow, and generate more appropriate wave reflections.

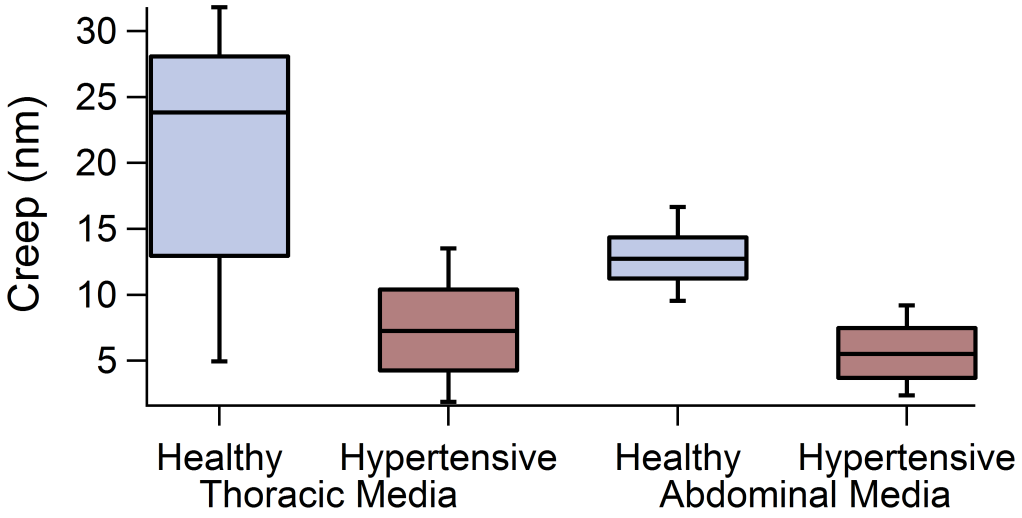

Figure 3.8: Box and whisker plots of creep deformation for the tunica media of the thoracic and abdominal aorta in the healthy and hypertensive case, N=8000 for each box.

Notably we see that creep behaviour has been greatly impaired by hypertension with thoracic media creep falling from 21.3 ± 21.1 nm in the healthy case to 7.16 ± 4.24 nm in the hypertensive while the abdominal creep drops from 12.5 ± 19.5 nm to 5.39 ± 5.81 nm. Once again this implies that hypertensive tissues have significantly impaired viscoelastic function. Much like in the tunicas intima and adventitia, the media seems to have short-term creep characteristics (τ_1) on the order of a tenth of a second with mean values across the different tissues and tensivities ranging from 0.162 s to 0.320 s. The long-term characteristic (τ_2) seems to run on the scale of a second with mean values between 0.930 s and 1.26 s. All mean values and associated

Table 3.1: Elastic moduli, creep characteristic response times of phase I and phase II relaxation for the medial tissues of SHR and WKY

Tissue	E (kPa)	Range (kPa)	Creep (nm)	τ_1 (s)	τ_2 (s)
SHR-TM	235.4	19.2–656	$7.16\pm4.24^{*}$	$0.310\pm0.94^{\ddagger}$	$1.19\pm1.24^{\star}$
WKY-TM	12.85	1.41–19.0	$21.2\pm21.4^{*}$	$0.320\pm0.81^{\ddagger}$	$1.26\pm1.22^{\dagger}$
SHR-AM	477.3	87.5–813	5.39 ± 5.81	0.162 ± 0.50	0.930 ± 1.18
WKY-AM	23.71	0.90–47.7	12.5 ± 9.81	0.243 ± 0.71	$1.22\pm1.05^{\dagger,\star}$

*, ‡, †, and *Indicates statistical equivalence

variances are available in Table 3.1. In the intima, Figure 2.8, we saw lengthening of τ_1 and shortening of τ_2 as a result of hypertension. However, here we see no significant change to τ_1 in the thoracic media with hypertension but do see a shortening in the abdominal media, Figure 3.9. This means that there has been no change to the relative rate of creep accommodation in the thoracic tunica media but that the relative rate in the abdominal tissue has increased. Therefore, the abdominal media will now exhibit the first 64% of its creep behaviour in 0.162 s instead of 0.243 s in the healthy animal even though the overall amount of creep has decreased. With τ_2 however there

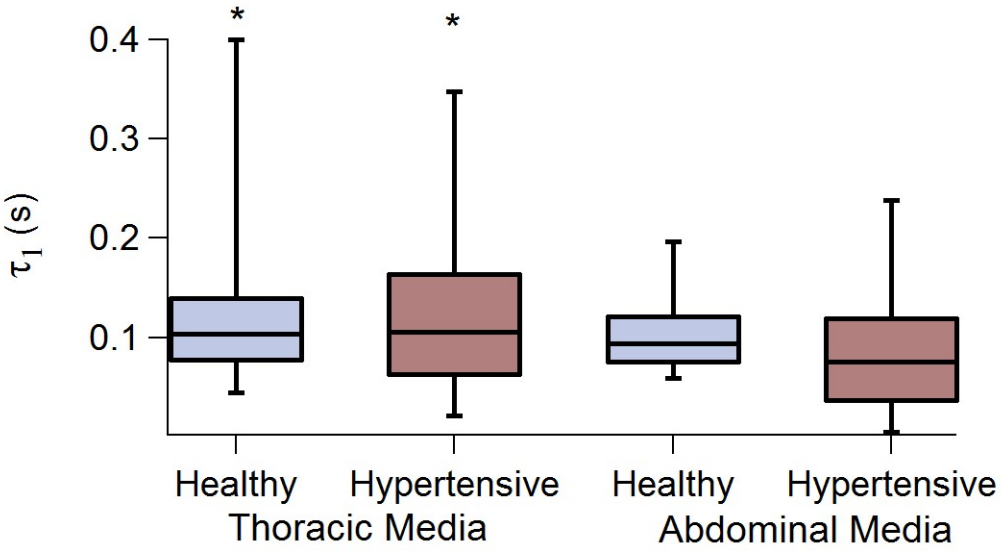

Figure 3.9: Box and whisker plots of the short-term creep characteristic, τ_1, for the tunica media of the thoracic and abdominal aorta in the healthy and hypertensive case, N=8000 for each box.

is a distinction between the healthy and hypertensive thoracic media whereby the characteristic accommodation time for the fast process is shortened. This means that last third of accommodation occurs faster in the hypertensive animal. The same is seen to occur to an even greater degree in the abdominal media. This, combined with the findings for τ_1, would suggest to us that the majority of hypertensive changes to the rate of creep accommodation occur in the last third of the process and function to increase the relative rate. Additionally, this process and the quickening of the faster relaxation process seem to occur more so in the abdominal media than the thoracic.

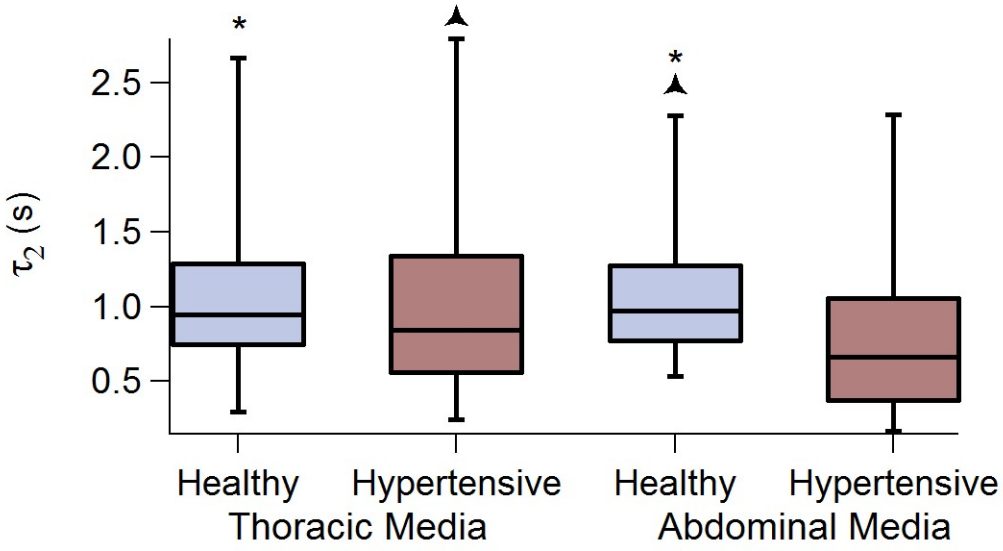

Figure 3.10: Box and whisker plots of the long-term creep characteristic, τ_2, for the tunica media of the thoracic and abdominal aorta in the healthy and hypertensive case, N=8000 for each box.

3.3.4 Relationships Between Elastic Modulus and Creep

Seeing the elastic and viscoelastic data for the differential arterial layers brings about the question of whether or not there exists a relationship between the two. Comparison of force maps depicting elastic moduli and viscoelastic creep from the same location such as in Figure 3.11 depict obvious and recurrent qualitative relationships.

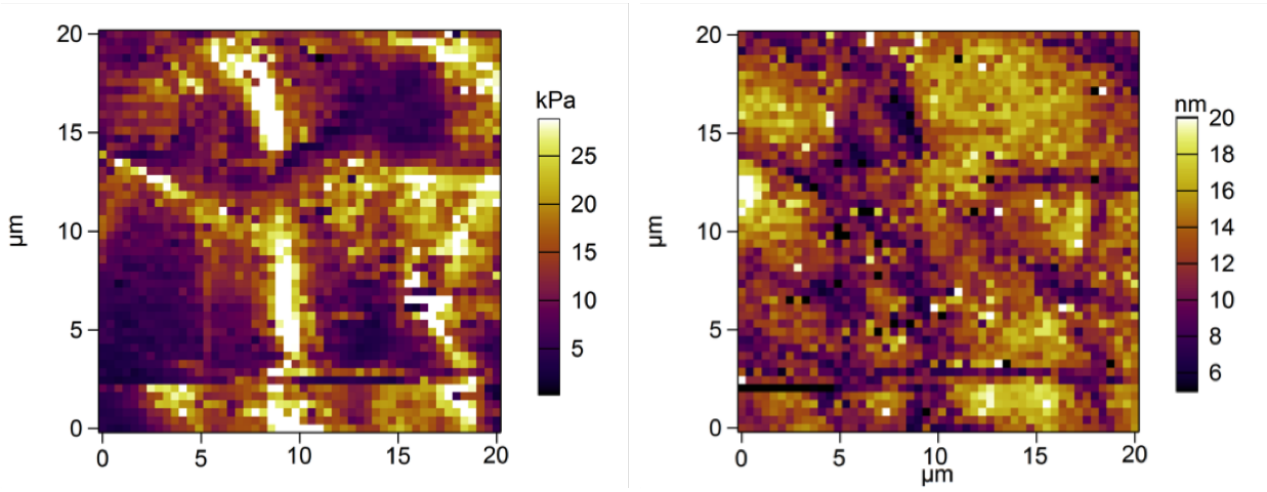

Figure 3.11: Elastic modulus (left) and creep (right) maps taken at the same site on the healthy thoracic tunica media in sequence display visual relationships between the two properties.

Here there are apparent relationships between both elasticity and structure, viscoelasticity and structure, and also between elasticity and viscoelasticity. In terms of the relationship between elasticity and structure we see that stiffer (brighter) points are spatially coherent and seem to correspond to to structures that appear fibrous in nature. At the same time in the areas between these stiffer, fibrous structures are more elastic (darker) areas that may be representative of VSMCs. Comparison to the creep map reveals that these stiffer, fibrous areas correspond to areas of lesser viscoelastic deformation. This aligns with what one would expect, that is that stiffer areas would inherently have a lesser capacity to accommodate to a tip dwelling at constant force.

Figure 3.12 shows another obvious relationship between creep and elasticity. Here there appear to be two crossing fibre structures, possibly collagen or elastin, that are more elastic than the surrounding tissue. The greater elasticity would suggest that these fibres may be elastin or Type III collagen. These fibres are also easily identified on the creep map where they appear as brighter regions, indicating that they demonstrate more creep behaviour than their surroundings. As in Figure 3.11 we

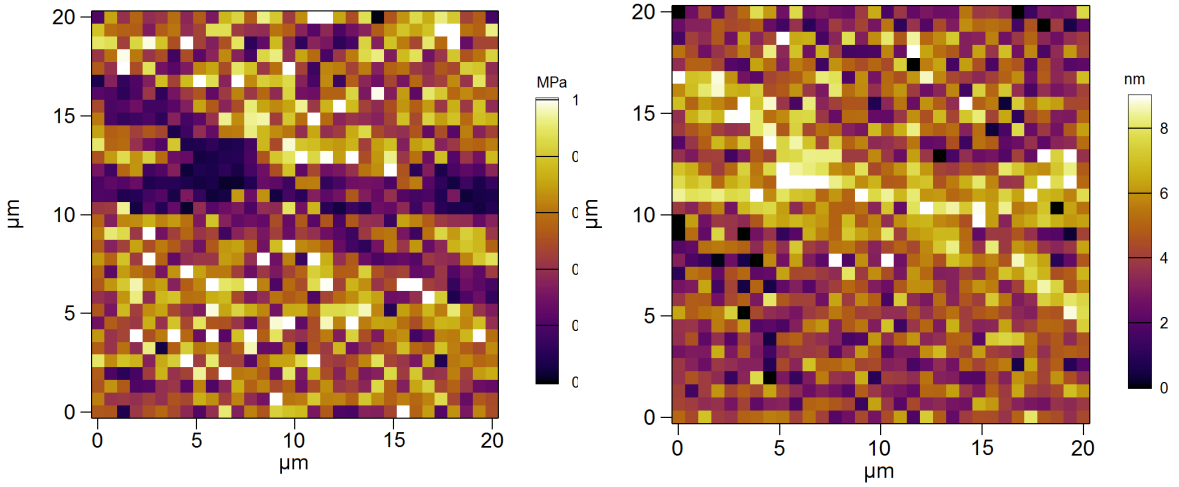

Figure 3.12: Amplitude images of healthy abdominal tunica media (left) and hypertensive thoracic tunica media (right) with greater collagen density and some VSMCs apparent.

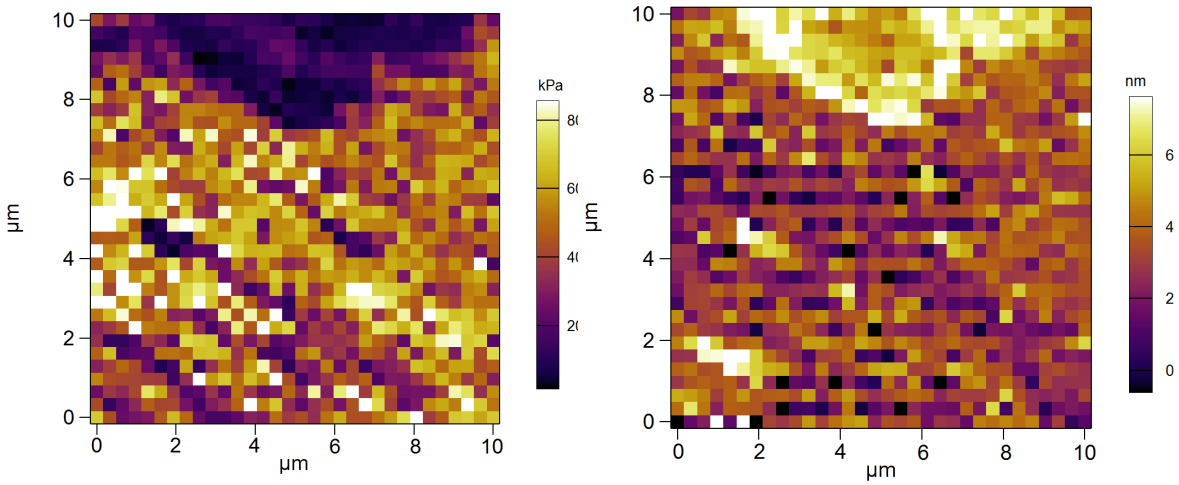

Figure 3.13: Amplitude images of healthy abdominal tunica media (left) and hypertensive thoracic tunica media (right) with greater collagen density and some VSMCs apparent.

see that more elastic regions are also more viscoelastic. Similarly, this is the case in Figure 3.13 where the very elastic hemispherical region exists at the top of the map directly corresponds to a region of significant creep deformation. This hemispherical region may be one end of a VSMC as it is of appropriate width and shape. This is further reinforced by the fact that we would expect VSMCs to be more elastic than the surrounding tissue which is primarily composed of collagen fibrils.

In order to better understand the apparent relationship between viscoelastic creep and elasticity we plot the pointwise distribution of elastic modulus and creep. Figure 3.14 and Figure 3.15 represent the distribution of creep with varying elastic modulus for the thoracic and abdominal intima , respectively, for both the healthy WKY (blue) and hypertensive SHR (right). This introduces a trend where at very low elastic modulii, the creep tends to be quite large and then drops off as we move towards higher elastic moduli. This follows directly from the argument made in the previous paragraph. However, we do see a few interesting behaviours. The distribution for the hypertensive thoracic intima is widely dispersed compared to the relatively tight distributions of the others. Interestingly, this distribution has held up to further data collection and analysis. This suggests that this "bad" distribution may be a result of hypertension whereby hypertension heterogenizes the tissue so much that no relationship is apparent. Physiologically speaking, this may result from differential effects of hypertension on differential tissue components. I.E. endothelial cells may respond differently than the subendothelial layer of collagen and so on. There is some evidence to support this "differential response" present in the distributions of both the healthy and hypertensive abdominal intima where we see two somewhat discrete distributions. One distribution tends sharply towards values of much higher elastic moduli as creep nears zero while the second shows a much more gradual increase in elastic moduli associated with smaller creep deformations. The health thoracic

intima does not display this behaviour and seems to have only one distribution. This may relate to the requirement of the thoracic tissue to regulate the Windkessel effect and also to dissipate energy. Incidentally one would expect these behaviours to be optimized in the case where tissues demonstrate homogeneous viscoelastic behaviour.

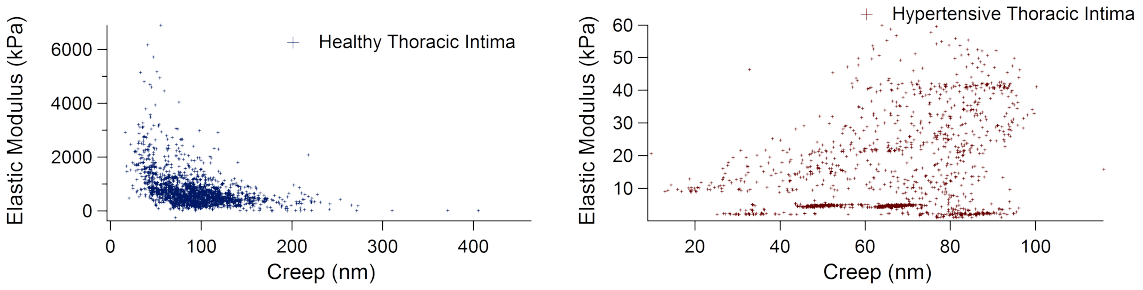

Figure 3.14: Relationship between elastic modulus and creep for the healthy (left) and hypertensive (right) thoracic intima.

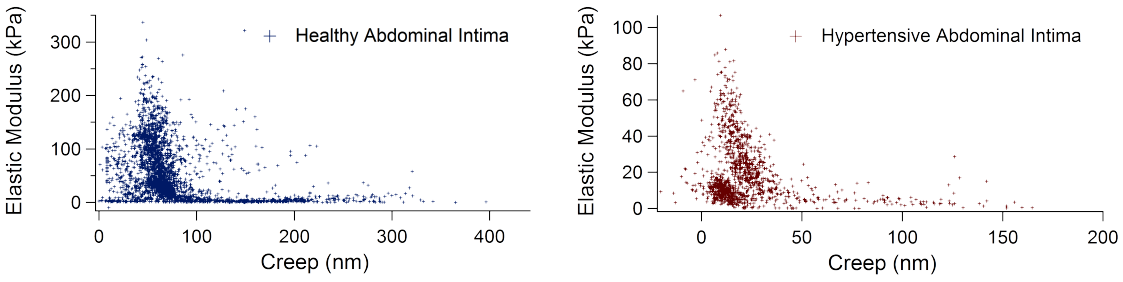

Figure 3.15: Relationship between elastic modulus and creep for the healthy (left) and hypertensive (right) abdominal intima.

Moving towards the tunica media we see no significant alteration in the form of the distribution though we do see that the distribution in the healthy case is "looser" than that in the hypertensive. This lack of major difference is significant as we expected the tunica media to the be the layer limiting viscoelastic behaviour of the tissues, this is discussed in Section 3.3.3. This means that in the hypertensive animal the tunica media likely retains a homogenous viscoelastic response but at the same time, has a mitigated creep capacity. Interestingly, changes in the magnitude of creep can also be imagined

to impair behaviours like the Windkessel effect as the time component, identified in this work by the creep characteristic τ, is intrinsically linked to the magnitude of the viscoelastic deformation, equation 2.2. This means that while the response may be heterogeneous in nature, the incredibly important timing of viscoelastic behaviours will be altered by changes in the magnitude of creep.

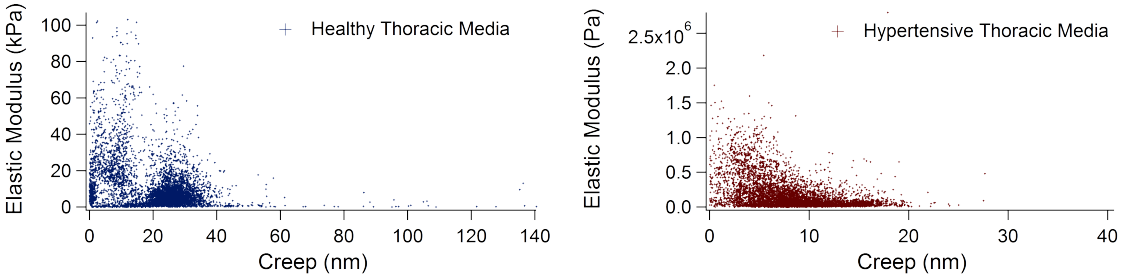

Figure 3.16: Relationship between elastic modulus and creep for the healthy (left) and hypertensive (right) thoracic media.

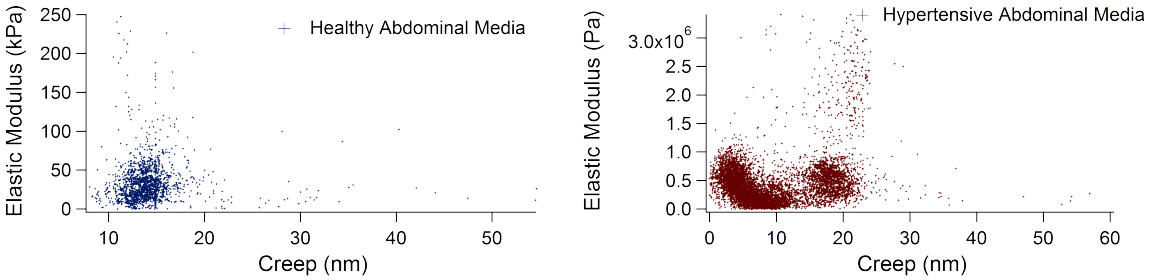

Figure 3.17: Relationship between elastic modulus and creep for the healthy (left) and hypertensive (right) abdominal media.

In the tunica adventitia we see a shockingly similar form for the distributions in both the healthy and hypertensive thoracic tissues that seem to display only one distributive trend. However, in the abdominal tissue the hypertensive distribution is dispersed widely, much as in the hypertensive thoracic intima, Figure 3.14. The occurrence of "scattered distributions" in these two tissues is interesting for the following reasons: i) We have seen the thoracic tunica intima to undergo significantly larger

alterations due to hypertension than most other tissues, likely due to its proximity to the heart and subsequent exposure to large pulse pressures; and ii) We expect that the abdominal adventitia likely undergoes notable hypertension remodelling as a compensatory mechanism as discussed in Chapter 2. This brings further support to the argument that these two distributions are likely related to the effects of hypertension and are not unfounded aberrations.

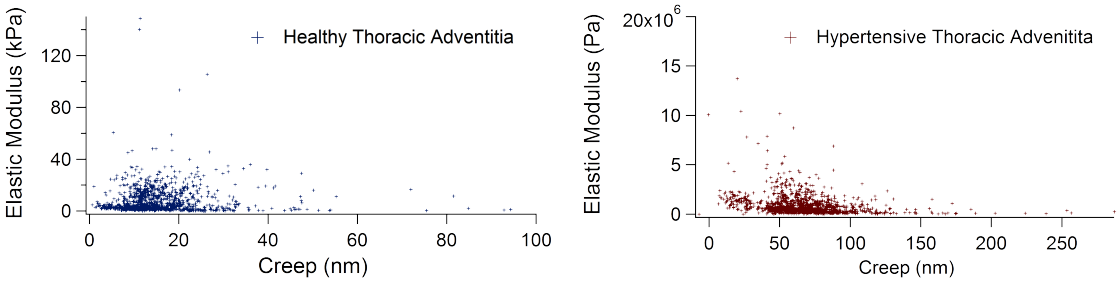

Figure 3.18: Relationship between elastic modulus and creep for the healthy (left) and hypertensive (right) thoracic adventitia.

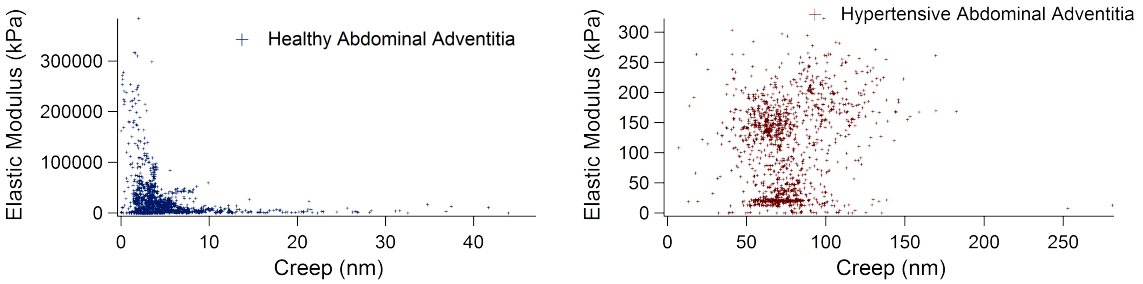

Figure 3.19: Relationship between elastic modulus and creep for the healthy (left) and hypertensive (right) abdominal adventitia.

While the shape of the distributions allow for the presentation of some possible relationships with a qualitative base they are not sufficiently discrete or well-defined to allow for reasonable mathematical fitting. This is not unexpected as biological tissues are, almost without exception, heterogeneous in nature and the data presented in this work finds the aorta to have significant structural and mechanical heterogeneity even

on the nanoscale. Unfortunately, this means that no concise, mathematical relationship can be drawn between elastic modulus and creep as of yet and that other viscoelastic parameters such as the creep characteristics, Chapter 2, must be investigated.

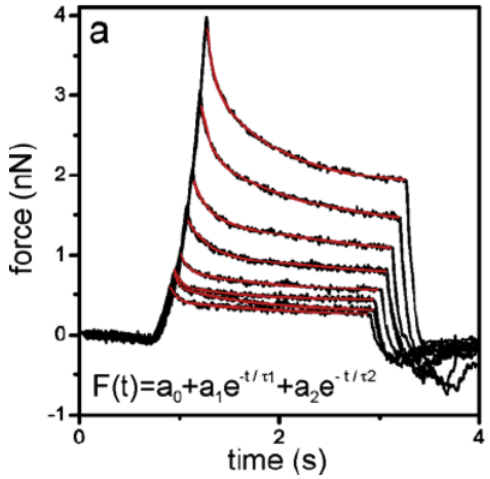

Figure 3.20: Force-relaxation plots showing decay of force over time for a tip held at constant indentation depth by the piezo. (Adapted with permissions from Moreno-Flores et al (2010). Copyright IOP Publishing 2010.) [24]

The determination of other advanced viscoelastic parameters such as the viscosity, η, and the compressive moduli, k, require both creep deformation experiments (conducted here) and also force or stress-relaxation experiments, Figure 3.20. In such an experiment the force exerted by the tip on the sample is no longer held constant. Instead there is a constant strain held on the tissue (indentation depth in this case) while we observe changes (usually detorioration) in force with time. Unfortunately, experiments of this variety are not possible on the AFM system used in this work.

3.4 Conclusions

Here our minimal nanoindentation approach has enabled differentiation of the tunica media from the tunicas intima and adventitia. Additionally, it has found this layer to be mechanically distinct and also to undergo dramatic hypertensive remodelling

which vastly affects its mechanical behaviours. The healthy tunica media, with a mean modulus of 12.85 kPa and 23.71 kPa for the thoracic and abdominal tissues respectively, has been found to have an elasticity on the same order as the healthy tunica intima. On the other hand, the hypertensive tunica media, with moduli of 235.4 kPa and 477.3 kPa for the thoracic and abdominal tissues respectively, were found to have an elasticity more on par with that of the hypertensive tunica adventitia. These values, along with the associated elasticity ranges are given in Table 3.1 and depicted in Figure 3.5.

That the elasticity of the tunica media increases from that of the relatively mechanically inert tunica intima in its native state to be on an order with that of the tunica adventitia in hypertension is significant. In the intima and adventitia we had seen approximately a two-fold stiffening. Here we are observing ten-fold or greater stiffening. This means that while the adventitia provides the majority of resistance to excessive distension in the normotensive aorta, the media adds significant resistance in the hypertensive case. [1] With hypertension then, the pulse pressure must be significant enough to overcome the combined resistance of the hypertensive adventitia and also the hypertensive media to allow for any reasonable amount of aortic distension. Without this distension, Windkesselian behaviour is both mitigated and altered in nature. Concisely put, the tunica media experiences the most significant nanoscale elastic changes due to hypertension which, in all likelihood, strongly affects overall aortic distensibility.

Again we observed an increase in elastic modulus in the abdominal tunica media c.f. that of the thoracic aorta in both the healthy and hypertensive animal. This follows with our argument presented in Chapter 2 that the abdominal tissues, being less proximal to the heart, have less requirement to deal with large pulse pressures resulting from left ventricular contraction, and therefore do not require significant elasticity to

absorb and disperse this energy. This allows us to comprehensively conclude that this is the case for the aorta as a whole, as we observe this to be the case across all three differential layers.

The tunica media has been noted to likely be the primary determinant of whole-artery viscoelasticity. [22] The data presented in Section 3.3.3 shows agreement with this as we find the creep deformation of the tunica media to have mean values of 21.2 nm and 7.16 nm in the healthy and hypertensive thoracic media respectively with 12.5 nm and 5.39 nm in the healthy and hypertensive abdominal media respectively. These values are, at best, a fraction of the creep observed in tunicas intima and adventitia from the same site and rat strain. From this we can conclude that the tunica media, having the smallest viscoelastic capacity of all three layers, is likely the predominant layer in terms of limiting viscoelastic behaviour as put forth for the bulk-scale tissue by Clark and coworkers. [22]

In addition to decreased elasticity of abdominal tissues we also see lesser creep deformation. This is readily apparent in Figure 3.8 where the abdominal tissue in both the healthy and hypertensive strains show less creep deformation than the thoracic analogue. Again, this can be justified by the lesser need of the abdominal tissues to dissipate energy as energy dissipation is primarily due to viscous behaviour and not elastic behaviour.

In this chapter we have also investigated the relationship between elasticity and viscoelasticity and have found a qualitative, but complicated relationship to exist. Hypertension has been seen to affect this relationship differently in different tissues. This has been reasoned to be caused by different components of the layers (collagen, elastin, VSMCs, etc.) responding differently to hypertension which would give rise to varied responses in areas of differing composition. Unfortunately, this makes for a very complex relationship which requires a comparably complex analysis.

The above being noted we have found the tunica media to undergo dramatic hypertensive stiffening. This stiffening may result in the media becoming a significant limiting factor in the distensibility of the aorta in addition to the adventitia which assumes this role alone in the healthy animal. The media has also been found to be the predominant layer in terms of limiting aortic viscoelasticity and, at the same time, is found to have the same impaired by hypertension. This means that hypertension has a negative effect on the viscoelastic capacity of the aorta as a whole.

Bibliography

[1] C. Schulze-Bauer, P. Regitnig, and G. Holzapfel. Mechanics of the human femoral adventitia including the high-pressure response. *American Journal of Physiology: Heart and Circulatory Physiology*, 282(6):H2427, 2002.

[2] T. Khamdaeng, J. Luo, J. Vappou, P. Terdtoon, and E.E. Konofagou. Arterial stiffness identification of the human carotid artery using the stress–strain relationship in vivo. *Ultrasonics*, 52(3):402, 2012.

[3] P. Hadjiisky, N. Peyri, and Y. Grosgogeat. Tunica media changes in the spontaneously hypertensive rat (SHR). *Atherosclerosis*, 65(1):125, 1987.

[4] R I Bashey, R Cox, J McCann, and S A Jimenez. Changes in collagen biosynthesis, types, and mechanics of aorta in hypertensive rats. *The Journal of laboratory and clinical medicine*, 113(5):604–11, 1989.

[5] B. Shekhonin, S. Domogatsky, V. Muzykantov, G. Idelson, and V. Rukosuev. Distribution of type I, III, IV and V collagen in normal and atherosclerotic human arterial wall: immunomorphological characteristics. *Collagen and Related Research*, 5(4):355, 1985.

[6] H. Turto, S. Lindy, and J. Uitto. Increased collagen prolyl hydroxylase activity in the aortic wall of rabbits exposed to chronic hypoxia. *atherosclerosis-journal.com*, 33(4):379, 1979.

[7] H. Senzaki, M. Akagi, and T. Hishi. Age-associated changes in arterial elastic properties in children. *Korean Circulation Journal*, 40(4):153, 2002.

[8] A. Levin. The cardiovascular effects of aortic clamping and unclamping. *Southern African Journal of Anaesthesia and Analgesia*, 16(2):62–71, 2010.

[9] A. Avolio. Arterial Stiffness. *Pulse*, 1(1):14, 2013.

[10] J. Ogeng'o, A. Malek, and S. Kiama. *Folia Morphologica*, volume 69. Via medica, 2010.

[11] J. Ogeng'o, A. Malek, S. Kiama, and B. Sci. Muscle "islands" in the tunica media of the goat thoracic aorta. *Brazilian Journal for Morphological Sciences*, 26(1):179, 2009.

[12] S. Arribas, C. Hermida, M. González, Y. Wang, and A. Hinek. Enhanced survival of vascular smooth muscle cells accounts for heightened elastin deposition in arteries of neonatal spontaneously hypertensive rats. *Experimental Physiology*, 95(4):550, 2010.

[13] J. Kaski. Atheromatous plaque location and arterial remodelling. *European Heart Journal*, 24(4):291, 2003.

[14] B. van Varik, R. Rennenberg, C. Reutelingsperger, A. Kroon, P. de Leeuw, and L. Schurgers. Mechanisms of arterial remodeling: lessons from genetic diseases. *Frontiers in genetics*, 3(13):290.

[15] Jonathan C. L. Rodrigues, Stephen Rohan, Amardeep Ghosh Dastidar, Adam Trickey, Gergely Szantho, Laura E. K. Ratcliffe, Amy E. Burchell, Emma C. Hart, Chiara Bucciarelli-Ducci, Mark C. K. Hamilton, Angus K. Nightingale, Julian F. R. Paton, Nathan E. Manghat, and David H. MacIver. The Relationship Between Left Ventricular Wall Thickness, Myocardial Shortening, and Ejection Fraction in Hypertensive Heart Disease: Insights From Cardiac Magnetic Resonance Imaging. *The Journal of Clinical Hypertension*, 18(11):1119–1127, 2016.

[16] M. AlGhatrif and E. Lakatta. The conundrum of arterial stiffness, elevated blood pressure, and aging. *Current hypertension reports*, 17(2):12, 2015.

[17] M. AlGhatrif, J. Strait, C. Morrell, M. Canepa, and J. Wright. Attenuated aortic dilatation, not increased wall stiffness best explains the rise in pulse pressure in women with aging: results from the Baltimore Longitudinal Study. *Circulation*, 128(22):A18061, 2013.

[18] T. Wong and P. Mitchell. Hypertensive Retinopathy. *New England Journal of Medicine*, 351(22):2310–2317, 2004.

[19] M. Murea and B. Freedman. Essential hypertension and risk of nephropathy: a reappraisal. *Opinions in Nephrology and Hypertension*, 19(3):245, 2010.

[20] B. Rutkowski, L. Tylicki, and J. Manitius. Hypertensive nephropathy–an increasing clinical problem. *Mineral and Electrolyte Metabolism*, 25(1):68, 1999.

[21] P. Dobrin. Distribution of lamellar deformations: implications for properties of the arterial media. *Hypertension*, 33(3):806, 1999.

[22] J. Clark and S. Glagov. Transmural organization of the arterial media. The lamellar unit revisited. *Arteriosclerosis*, 5(1):19.

[23] J. Chaui-Berlinck and L. Monteiro. Frank–Starling mechanism and short-term adjustment of cardiac flow. *Journal of Experimental Biology*, 220(23):4391, 2017.

[24] S. Moreno-Flores, R. Benitez, M. dM Vivanco, and J. Toca-Herrera. Stress relaxation microscopy: Imaging local stress in cells. *Journal of Biomechanics*, 43(2):349, 2010.

Chapter 4

Nanomechanical Viscoelastic Characterization of Normotensive and Hypertensive Murine Heart Tissues

4.1 Introduction

Hypertension has multifarious and far reaching effects not only upon vasculature, but also the heart itself. Rather than just being coincident, this is a linked pathology. Arterial stiffening in addition to normal cardiac remodelling with age induces significant geometric changes within the ventricles. [1, 2] These alterations to the heart fall under the umbrella of hypertensive heart disease which represents a multitude of biochemical, structural, and mechanical adaptations in response to hypertension. [3, 4] Common amongst these adaptions are left-ventricular hypertrophy, contractional left-ventricular dysfunction, and decreased coronary holding. The end-state of hypertensive heart

is known as congestive heart failure (CHF). CHF is characterized by a progressive inability of the heart (normally the left ventricle in hypertensive heart), to generate pumping behaviour sufficiently strong enough to overcome left-ventricular afterload. This results in blood backing up into pulmonary circulation and affecting oxygenation. Ultimately, excessive filling of the left-ventricle causes lengthening of cardiac muscle beyond the optimal Frank-Starling range, and contractions weaken progressively, which worsens the situation. [5, 6]

There exists a strong relationship between hypertensive conditions and ischaemic heart disease with hypertension being implicated in 47% of cases. [7] The changes throughout the differential layers of the heart wall during left ventricular hypertrophy are understood to be the bridging phenomena between the two conditions. Particularly it is known to affect coronary blood flow and decrease coronary reserve. Such has been found to be the case in the SHR animal which exhibits increased coronary vascular resistance and impaired coronary flow. [8] On a broader scale, this is significant considering that each increase of 20 mmHg in systolic blood pressure or 10 mmHg in diastolic blood pressure beyond 115 and 75 mmHg respectively is associated with a two-fold increase in death rate from coronary disease. [9]

The elastic and viscoelastic behaviour of the heart are expected to be determined predominantly by the structural and geometric arrangements of ventricular constituents. [10] In particular, the subendocardial layer undergoes notable early fibrosis in response to heightened pressures. This fibrosis occurs primarily through fibrillogenesis of the fibrillar Types I and III collagen. The relatively inelastic collagen may impair cardiomyocyte force generation by limiting muscular distension. Concerning as subendocardial fibrosis may be, we must also consider whole-ventricular stiffness which has been directly linked to increased arterial load. [11] Likely, ventricular stiffening relates to cardiac fibrosis but, to the author's knowledge, no investigation to localize

nanomechanical changes across the differential heart layers has been accomplished yet. The work within this chapter seeks to evaluate the elastic and viscoelastic behaviours of the endo and epicardial layers under the presumption that the majority of stiffening occurs within the myocardium. This being the likely case, it is unknown whether mechanical changes will be seen in the innermost and outermost layers or are localized exclusively to the myocardium.

The epicardium has been found to accumulate visceral fat in hypertensive pathologies. [12, 13] This fat accumulation has been found to lessen circumferential shortening of the heart. [14] However, no research into the implications of this finding in terms of nanoscale cardiac mechanics has been conducted. It would also be of interest to investigate the effects of hypertension on the larger coronary arteries, i.e. those before significant branching which run along the sulcii of the heart on top of the epicardium. [15] Alterations to these vessels could then be compared the work discussed in earlier chapters to determine if hypertension affects these vessels in a similar manner as systemic vasculature. Early return of wave reflections as discussed Chapter 2 in addition to arterial stiffness being linked to coronary artery disease give reason to believe this may be the case. [16] The question then arises whether the nanomechanical properties of the coronary arteries might also change in response to systemic hypertension, provided we can find and perform force spectroscopy on these vessels.

4.2 Experimental

4.2.1 Heart Sample Preparation and AFM Calibration

The samples were prepared and mounted as described in Section 2.2.1 and AFM calibration was completed as detailed in Section 2.2.2. However, on occasion the heart tissues had to have excess tissue removed from beneath the en face side in order to

decrease height sufficiently to allow for room between the AFM head and sample. This can be reasonably expected to have negligible effect upon the target tissue mechanics due to the fact that minimal indentation methods such as the one used here need not account for substrate effects. [17] Imaging was also attempted on a cross-section of the heart wall but significant variances in roughness across the differential layers made this approach inaccessible.

4.2.2 AFM Force Spectroscopy and Analysis

AFM force mapping was completed as detailed in Section 2.2.4 with the exception of mapping being completed 20×20 and a trigger force of 20 nN being used as we wish to hopefully achieve mechanical contributions from the subendocardial layer. This greater number of sampling sites is a step towards mitigating sampling bias common in AFM force spectroscopy studies. Once again, Hertzian analysis has been used to determine the elastic modulus, E. Once again, creep analysis has been conducted as described in Section 2.2.5 though a holding force of 20 nN was now used.

Two-way ANOVA with post-hoc Scheffe's test, performed in Igor Pro 7.11 (WaveMetrics), have been conducted on all data presented in this chapter. All results have statistically significant differences unless otherwise indicated.

4.3 Results

4.3.1 Nanoscale Topography of the Heart

The work conducted in this chapter is concerned with the morphology, elastic, and viscoelastic behaviours of the endocardium and epicardium. Before conducting force spectroscopy, cursory imaging was carried out in order to search for interesting structural features and to hopefully identify coronary arteries. Unfortunately, little

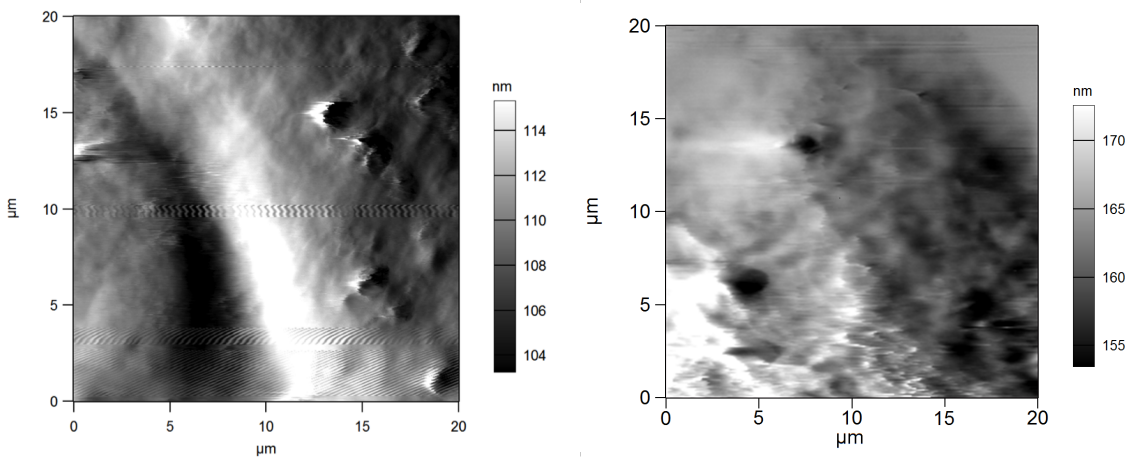

Figure 4.1: Amplitude images of healthy left ventricular endocardium (left) and hypertensive left ventricular endocardium (right) show relative smoothness of both tissues with possible underlying fibrillar structures in the hypertensive endocardium.

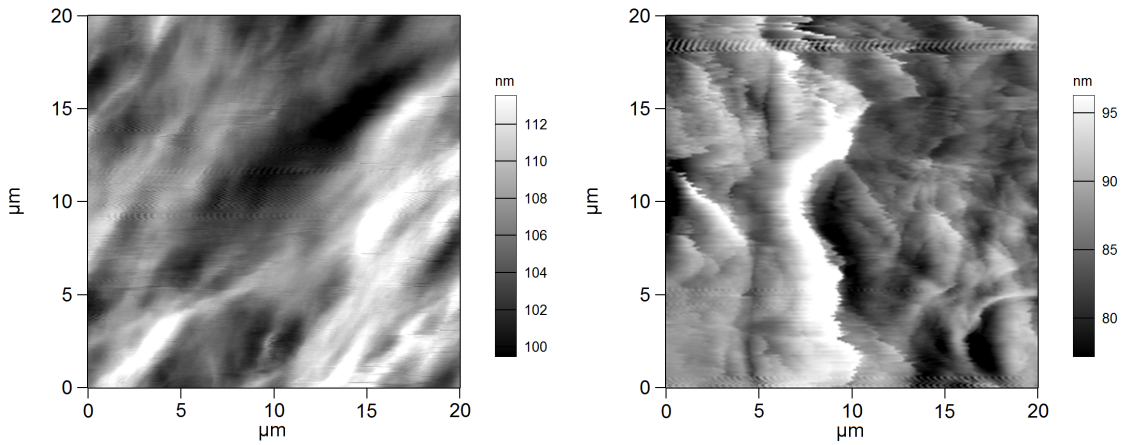

Figure 4.2: Amplitude images of healthy left ventricular epicardium (left) and hypertensive left ventricular epicardium (right) demonstrating increased bulbosity in the hypertensive case.

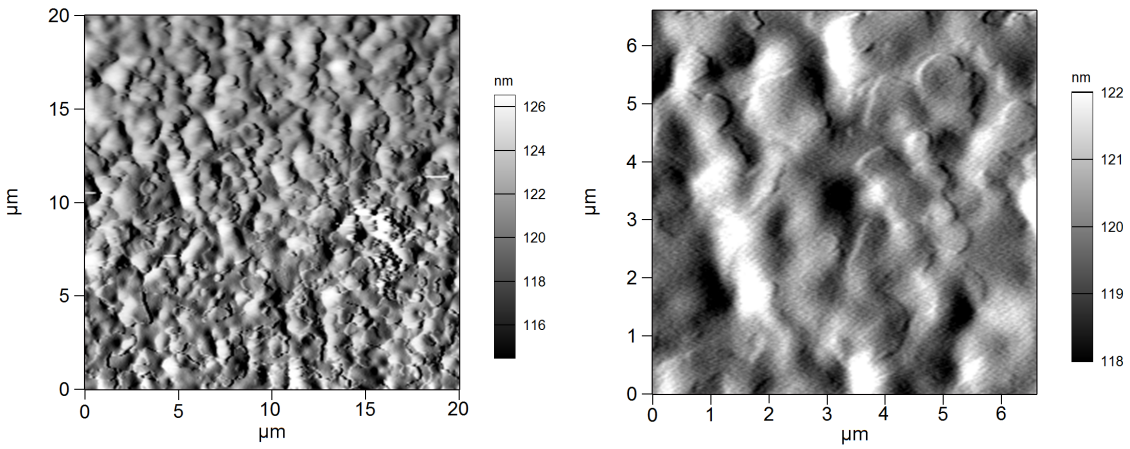

Figure 4.3: Amplitude images of hypertensive left ventricular myocardium showing what may be surface features of VSMCs.

of structural or functional significance was observed and the tissues, due to their bulbosity when hydrated, proved difficult to image upon.

In Figure 4.1 we can observe the relative smoothness of the endocardial layer in both the healthy and hypertensive species. This relative nanoscale smoothness runs counter-current to what is observed on larger scales where the left ventricular endocardium is however known to exhibit fairly significant roughness on the bulk-scale as is evidenced by the aforementioned bulbosity. [18] In contrast to this, the inner walls of the other heart chambers are known to be smooth as roughening would promote turbulence and increase energy loss. [18] It has been suggested that left ventricular endocardial roughness may aid in ejecting blood from the apical portion of the ventricle. [19] Moving from the healthy ventricle (left) to the hypertensive (right) we can see that there has been some small increase in roughness and, upon close inspection, there seems to be underlying fibrillar structures present in the hypertensive tissue. These structures may arise from the underlying subendocardial layer.

In the epicardium, Figure 4.2, no significant structural features are apparent. However, the hypertensive epicardium (right) generally seems to be more bulbuous

than the healthy. This may be inflammation occurring in the epicardial layer in response to left ventricular myocardial hypertrophy.

Figure 4.3 shows the morphology of hypertensive left ventricular myocardial tissue. There appear to be somewhat regular shapes throughout. Unfortunately, due to difficulty isolating and imaging upon the myocardium we were unable to confirm whether these structures are present in the WKY or even if they are ubiquitous throughout the SHR. Unfortunately, cardiac myocytes in the SHR have been reported to be in excess of 20 μm wide and in the vicinity of 100 μm long. [20] This would immediately disqualify the structures observed here from being myocytes. In fact, they would likely be structures present on the surface of these myocytes. These structures may be ion channels (likely sodium or potassium) or sarcoglycans. [21, 22]

4.3.2 Nanoscale Elastic Properties of Heart Tissues

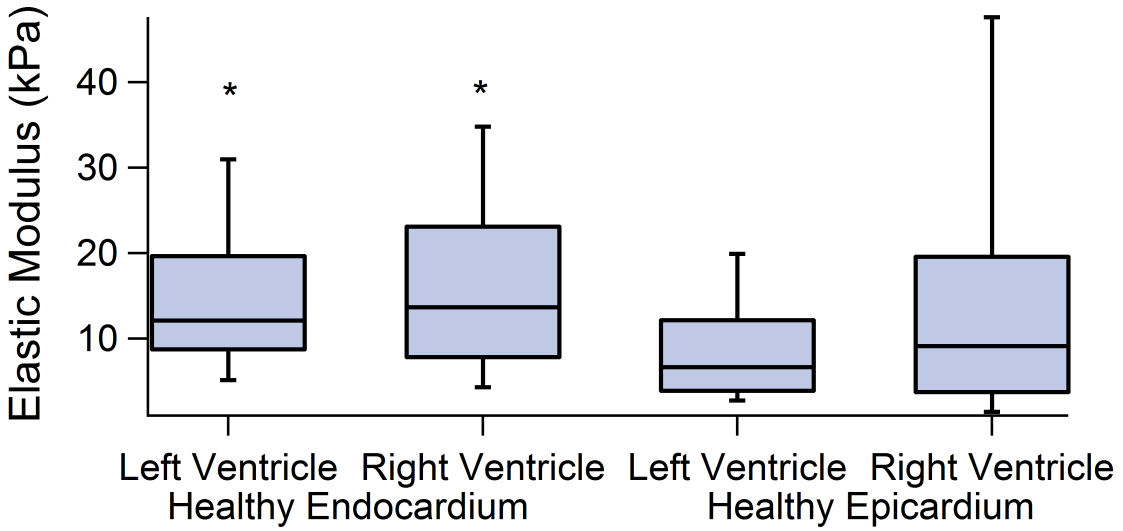

Figure 4.4: Box and whisker plots of elastic modulus for the endo and epicardium of each the left and right ventricles for the healthy case. N=8000 for each box.

The native nanoscale elasticity of the healthy epicardial and endocardial spaces of the left and right ventricles, Figure 4.4, tell us that there is no significant difference

in nanoscale elasticity between the left and right ventricular endocardium. The right ventricular epicardium is mildly stiffer than that of the left ventricle. It also appears that the epicardial tissues are slightly more elastic than their endocardial counterparts. The associated mean values and ranges can be found in Table 4.1.

In the hypertensive case, Figure 4.5, the left and right ventricular endocardia no longer exhibit the same elasticity. Now the left ventricles endocardium is significantly stiffer than that of the right. This is precisely what one might expect as a result of hypertension as the left ventricle deals with the increased cardiac afterload ultimately resulting from stiffer arteries. Again the epicardium in the right ventricle is seen to be stiffer than in the left. It also seems that the left ventricular epicardium is more elastic than the endocardium but there is no significant difference between the endo and epicardium of the right ventricle. The relevant numbers are provided in Table 4.2.

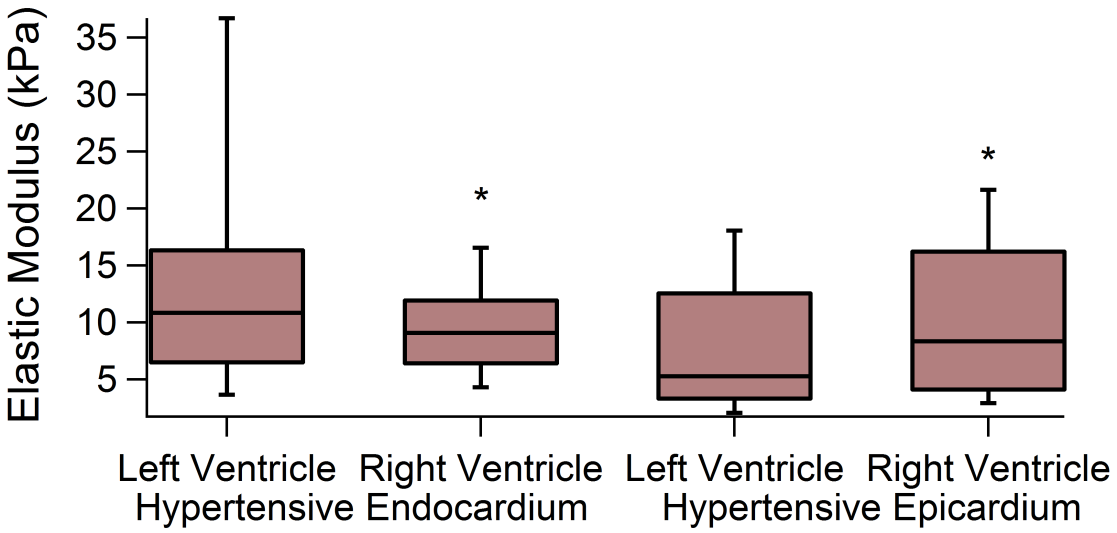

Figure 4.5: Box and whisker plots of elastic modulus for the endo and epicardium of each the left and right ventricles for the hypertensive case. N=8000 for each box.

When we directly compare the elastic moduli of healthy endocardial tissues with their hypertensive analogues in Figure 4.6 we observe something interesting. It seems that the elastic modulus of the hypertensive tissues is less than that of the healthy

tissues. This would mean that the hypertensive tissues are in fact more elastic. This is a rather counter-intuitive finding as we would expect to see stiffer endocardial tissues due to exposure to higher afterload. At the very least we would expect this in the left, if not the right, ventricle as arterial stiffening is known to induce remodelling and thickening of the heart wall in addition to cardiac fibrosis. [1, 23, 24]

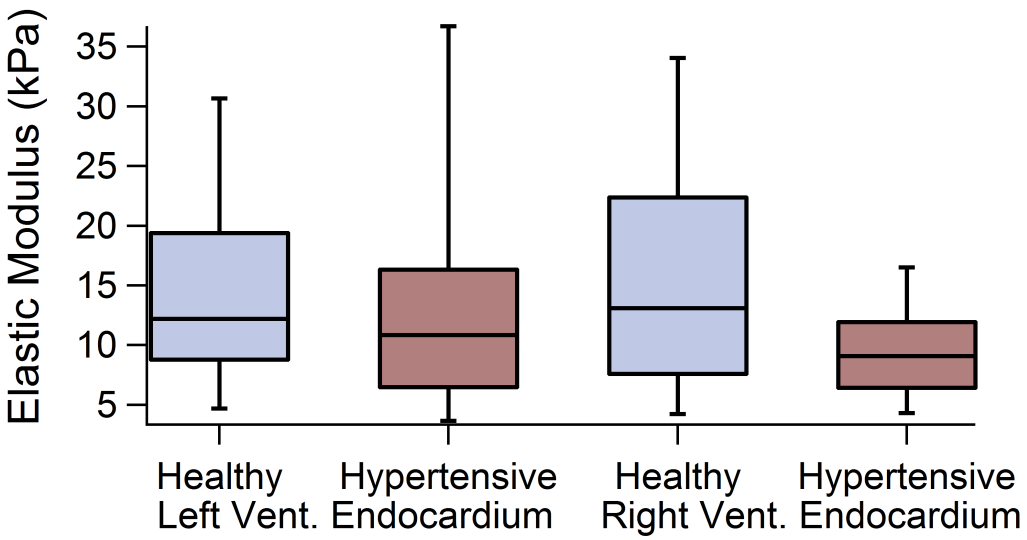

Figure 4.6: Box and whisker plots comparing the elastic modulus of the endocardium for each the left and right ventricles between the healthy and hypertensive case. N=8000 for each box.

Again, in the epicardial layer, we see that the hypertensive tissues exhibit greater elasticity than their healthy counterparts. However, the difference here is minute at best though still statistically significant. The incidence of greater nanoscale elasticity in hypertensive heart tissues seems to run countercurrent to what is known to occur on the bulk scale. This is particularly interesting as bulkscale ventricular stiffening is known, or at least strongly suspected, to be induced by myocardial and subendocardial fibrosis. Both mechanisms are known to have a nano or microscale pathogenesis predominantly related to changes in the composition of the extracellular matrix and collagen fibrillogenesis. In the healthy heart in excess of 85% of the collagen is Type

I which likely plays a role in resisting excessive distension or filling while roughly a tenth is Type III collagen which is predominantly concerned with maintaining wall elasticity. [25] The formation, degradation, and proportion of the different forms of fibrillar collagen within the heart is carried out almost exclusively by cardiac fibroblasts. [26] Inflammatory behaviours, such as those induced by increased afterload, of cardiac tissues can alter the action of these fibroblasts. These changes may ultimately have far reaching structural and functional implications for the heart. Generally, with fibrosis increased collagen deposition is observed in the perimysia (the sheaths surrounding cardiac muscle fibres) which has a net effect of stiffening the ventricle.

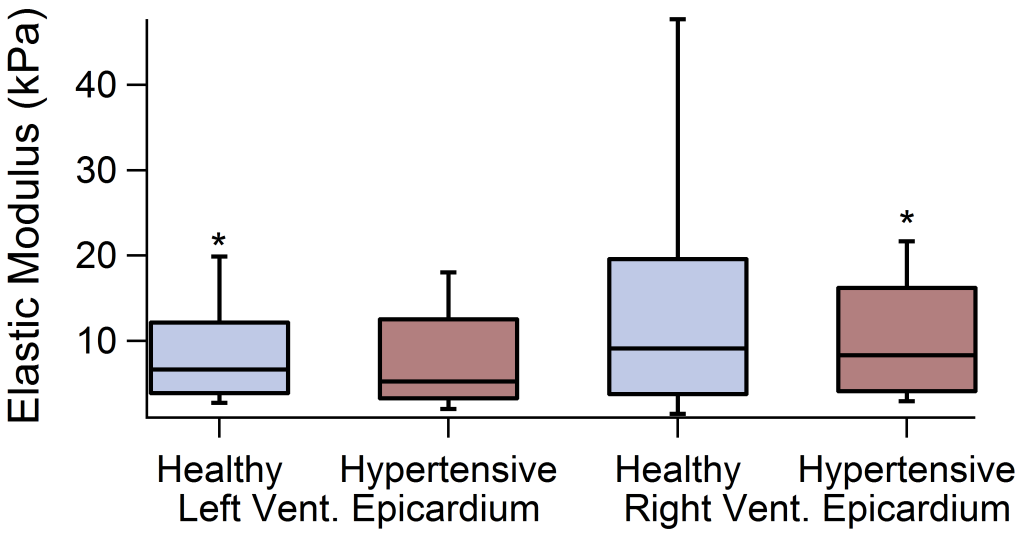

Figure 4.7: Box and whisker plots comparing the elastic modulus of the epicardium for each the left and right ventricles between the healthy and hypertensive case. N=8000 for each box.

However, in the hypertensive case, it is likely that fibrosis is not an isolated pathology and rather often occurs in the presence of subendocardial and myocardial ischaemia. [27, 28] Ischaemic myocardiopathies generally induce, as a first step, loss of myocotes through cell death most frequently occurring in the subendocardial layer as this region is most prone to ischaemia during ventricular contraction. Also as a

result of wall thickening, coronary circulation must probe ever deeper to perfuse these tissues. Following this loss, fibrosis may follow cell death occurring from an ischaemic state and function as a reparative process. [29] This provides a possible explanation for our observation of greater nanoscale elasticity in the hypertensive heart. It could be construed that, about the time period at which we are conducting force spectroscopy where the SHR are at 12-14 weeks of development, noticeable myocyte loss has occurred as a result of hypertension induced myocardial ischaemia but reparative fibrosis has not yet occurred to a large extent. This would mean that indentation is occurring on tissues with fewer myocytes per unit volume with no significant fibrosis as of yet. It could be expected that a heart with lesser myocyte density would exhibit greater elasticity and so more elastic tissues are observed in the hypertensive case than in the healthy. Provided this is true, ventricular elasticity would then be expected to decrease sharply if this tissues were re-examined in the following weeks when reparative fibrosis predominates. If this is the case then these findings would help to establish a timeline for significant myocyte loss due to hypertension induced myocardial ischaemia in the SHR.

4.3.3 Nanoscale Viscoelastics of Heart Tissues

Though less intuitive than in the arteries, viscoelasticity plays an important role in the diastolic behaviour of the heart. [30] Consider the period where ventricular filling has finished but contraction has yet to occur. During this phase the blood within the ventricle has settled to some degree and the force being exerted on the walls of the ventricle is constant and uniform. This raises the question, how does the ventricle respond? It turns out that the respondent behaviour is multifactorial, primarily being convoluted by the presence of concurrent ventricular relaxation both during and just after the filling phase. [31] This means that, in the widely accepted

viscoelastic model of the heart, intraventricular pressure is determined not only by the contained volume but also the strain rate on the chamber wall. Conversely, in an elastic model we would assume a relaxed ventricle to experience a pressure exerted solely by the volume alone. Traditional bulk-scale experiments usually attempt to tease out viscoelastic information by exposing fully relaxed ventricles to different filling rates for a given volume. Given our concern with viscoelastic behaviour of the heart, it is of interest whether this behaviour arises from the nanoscale or is perhaps a larger scale phenomenon.

Viscoelasticity not only factors into relaxation behaviours of the chambers but also in diastolic recoil. [32] Interestingly, diastolic recoil arises when fibres surrounding a bundle of cardiac myocytes release the energy they had stored during systolic compression. This ultimately creates a suction effect which assists in filling. The story of viscoelasticity within the heart also returns to collagen as perimysial (those surrounding the aforementioned muscle bundles) collagen fibres could ultimately limit the viscoelastic potential of the tissue on their scale. Consequently, a hierarchical argument could be used to to scale this limiting behaviour to a functional scale. [33]

The ventricles of the healthy heart, Figure 4.8, exhibit creep on the same order as the tunica media (proposed to be the layer responsible for limiting whole artery viscoelasticity). Creep is spread more widely and has a great mean value, 31.6±45.8 nm, in the left ventriclular endocardium than in the right, 18.1±19.6 nm. This can be reasonably justified by the greater pressures incident in the left ventricle which would promote adaptations encouraging increased chamber distensibility in order to try and minimize intraventricular pressure during diastole. This increased viscous distension might also allow for viscoelastic recoil coinciding with systolic contraction to promote a larger ejection force. The epicardium seems to exhibit no physiologially significant relationships between its function and the creep data presented here. This

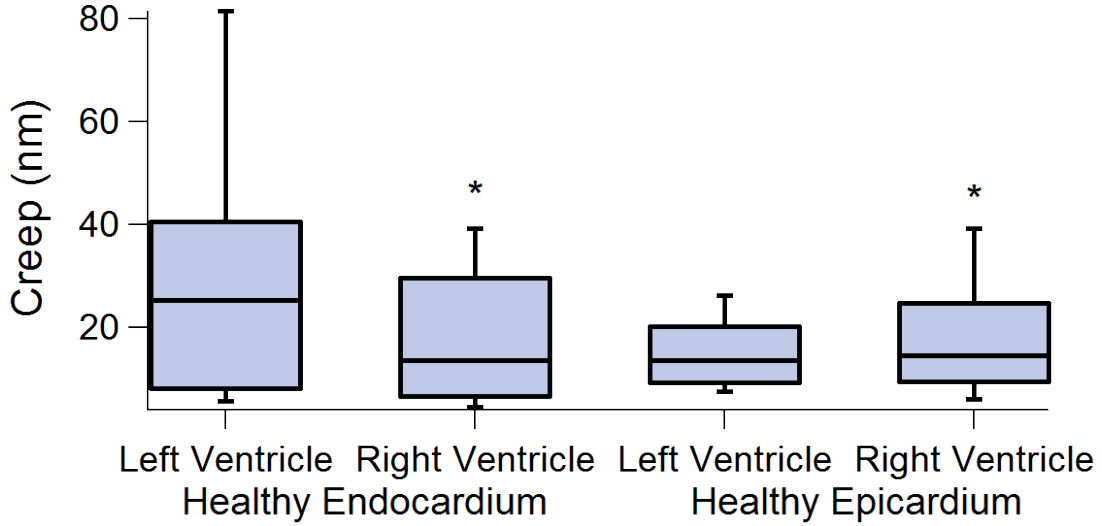

Figure 4.8: Box and whisker plots showing the creep deformation of the endo and epicardium for each the left and right ventricle of the healthy case. N=8000 for each box.

may be telling that the epicardium has no true requirement for viscoelastic behaviour (as would be expected physiologically).

In the ventricles of the SHR, Figure 4.9, we can see that there exists a wider disparity between the viscoelastic creep of the left and right ventricles both for the endo and epicardium. Specifically speaking, the left ventricular tissues exhibit a greater viscoelastic potential which is precisely what might be expected as is justified in the previous paragraph. However, we see it here for not only the endocardium but also the epicardium which was not the case in Figure 4.8. It may then be the case that increased left ventricular pressure due to hypertension combined with the loss of myocardial mass discussed in Section 4.3.2 is sufficient enough to produce mechanical adaptation in the normally mechanically inert epicardium. [34]

Direct juxtaposition of WKY and SHR endocardial creep, Figure 4.10, demonstrates that the viscoelastic capacity in the hypertensive tissue is significantly reduced in both the left (31.6 $\pm$ 45.8 nm healthy c.f. 18.1 $\pm$ 17.6 nm hypertensive) and right (18.1 $\pm$

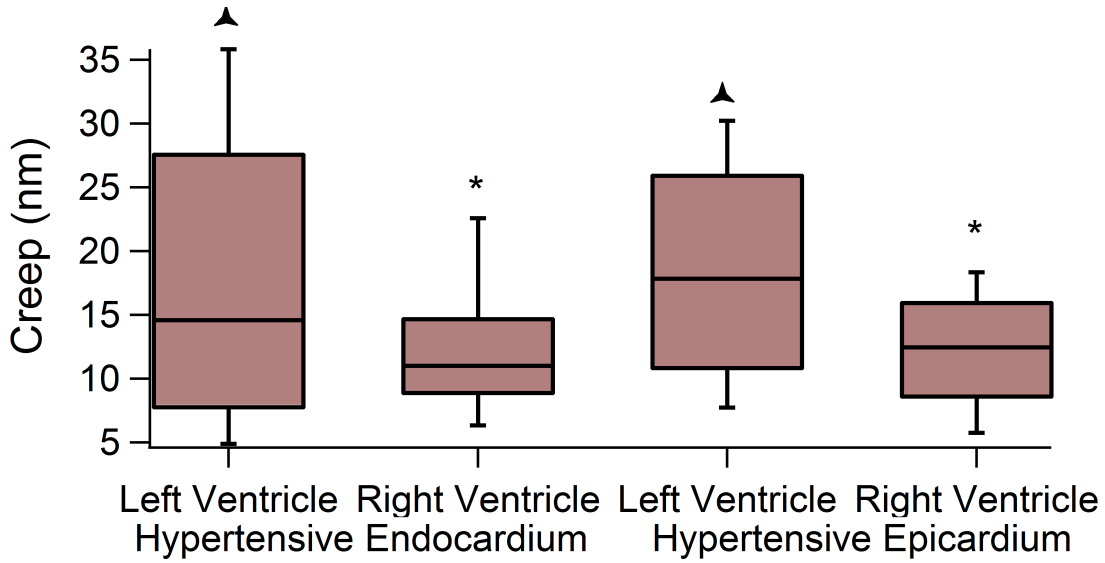

Figure 4.9: Box and whisker plots showing the creep deformation of the endo and epicardium for each the left and right ventricle of the Hypertensive case. N=8000 for each box.

19.6 nm healthy c.f. 12.5 ± 24.8 nm hypertensive) ventricles. Consequently, we can reason that hypertension impairs nanoscale viscoelastics of the ventricles which may have deleterious effects upon cardiac suction and end-diastole relaxation behaviour within these chambers.

Comparison of the epicardial layers, however, does not present any consistent trend across the left and right ventricles, Figure 4.11. Here we see that creep behaviour has increased in the hypertensive left ventricle which has been supported by arguments provided earlier in this section while in the right ventricle we observe creep impairment due to hypertension. One possible supporting rationale might result from increased coronary neovascularization occurring on the hypertrophied left ventricle in order to augment perfusion to this important yet pathological region. This neovascularization, combined with sub-optimal wave reflection timing (discussed in Section 1.2) might effectively decrease oxygen supply to the right ventricle which has not experienced significant hypertrophy and subsequent neovascularization. Resulting right ventricular

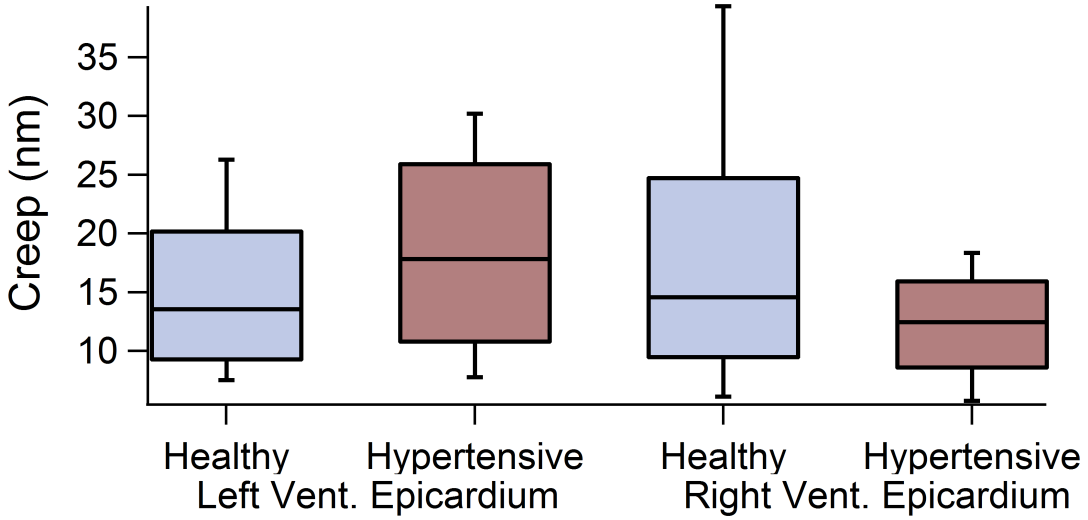

Figure 4.10: Box and whisker plots comparing the creep deformation of the epicardium for each the left and right ventricles between the healthy and hypertensive case. N=8000 for each box.

ischaemia might then be expected to produce a less viscoelastic tissue through changes in fibroblast based fibrillogenesis to alter the amount and proportion of Types I and III collagen.

Table 4.1: Elastic moduli, creep characteristic response times of phase I and phase II relaxation for the epi and endocardial tissues of the healthy WKY rat.

Tissue	E (kPa)	Range (kPa)	Creep (nm)	τ_1 (s)	τ_2 (s)
WKY-LV Endo.	17.8	5.16–31.0	31.6±45.8	0.15±0.44	$1.31\pm1.87^{\dagger}$
WKY-RV Endo.	18.9	4.31–34.8	18.1±19.6	0.29±0.78	$1.41\pm2.14^{\dagger}$
WKY-LV Epi.	11.0	2.76–19.9	15.1±22.4	$0.23\pm0.62^{*}$	1.72±2.16
WKY-RV Epi.	21.5	1.45–47.6	18.5±19.2	$0.19\pm0.52^{*}$	1.41±1.70

*, † Indicates statistical equivalence

In order to tease out further information about the viscoelasticity of these tissues we once again can delve into their bi-exponential behaviour. For each exponential term, Equation 2.2, of the creep accommodation which occurs, the associated creep characteristic, τ_1 or τ_2, inform us about the time-scale along which each relaxation process occurs. Looking at Figure 4.12 we can see that for the ventricular endocardia

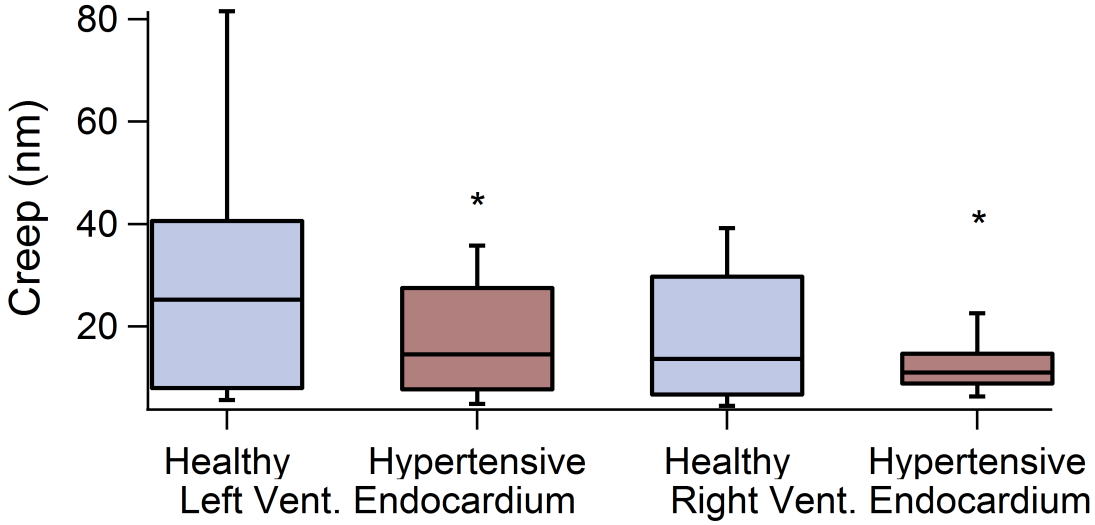

Figure 4.11: Box and whisker plots comparing the creep deformation of the endocardium for each the left and right ventricles between the healthy and hypertensive case. N=8000 for each box.

Table 4.2: Elastic moduli, creep characteristic response times of phase I and phase II relaxation for the epi and endocardial tissues of the healthy WKY rat.

Tissue	E (kPa)	Range (kPa)	Creep (nm)	τ_1 (s)	τ_2 (s)
SHR-LV Endo.	16.4	3.66–36.7	18.1±17.6	0.27±0.72	0.148±1.88
SHR-RV Endo.	9.80	4.31–16.5	12.5±24.8	0.18±0.48	1.43±2.01
SHR-LV Epi.	8.49	2.06–18.1	18.1±29.1	0.16±0.55	1.24±1.76
SHR-RV Epi.	10.8	2.92–21.7	12.0±13.2	0.28±0.76	1.41±2.01

*Indicates statistical equivalence

the short-term relaxation with time component given by τ_1 once again occurs on the order of a tenth of a second. There appear to be no large differences, Table 4.1 and Table 4.2, in behaviour between the left and right ventricles in this figure. However, the short-term relaxation seems to occur over a longer time period in the SHR than in the normotensive WKY. This is the case for both the left and the right ventricle. The same trend seems to carry over to the long-term relaxation seen in Figure 4.13 as, once again, the hypertensive analogues seem to experience their long-term relaxation over a longer period of time. Notably, this relaxation process occurs on the order of a second vice a tenth of that for the short-term process. There is also fairly uniform variance

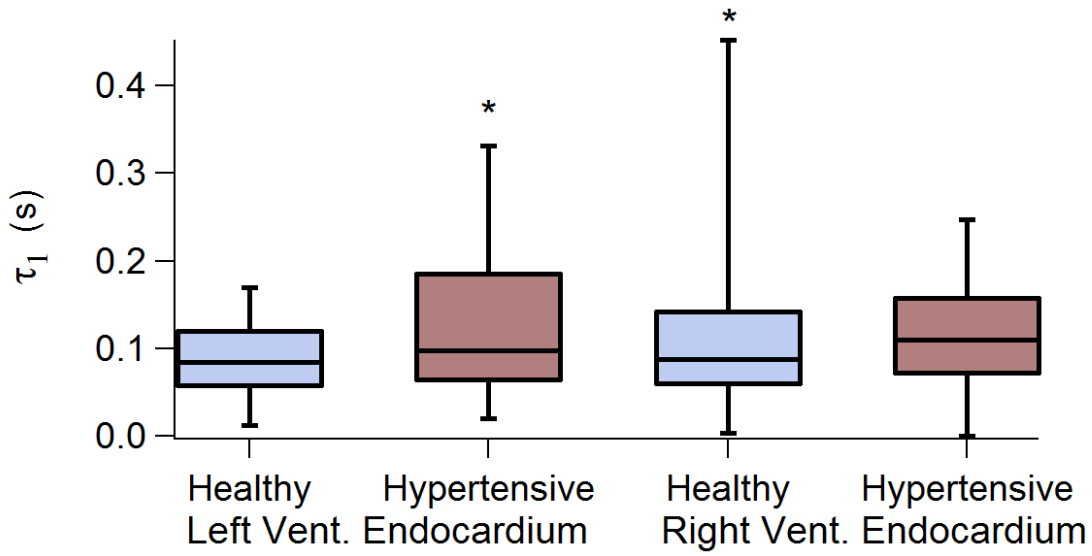

Figure 4.12: Box plots showing distribution of short-term relaxation times, τ_1, for healthy and hypertensive ventricular endocardia. N=8000 per box.

across the ventricles and strains as we see very similar error bars with relaxation times between approximately 1.75 and 4 seconds in 10% of the measurements depicted. Since Figure 4.10 shows a consistent hypertensive decrease in creep behaviour of the endocardium while Figure 4.12 and Figure 4.13 show consistent increases in both short and long-term relaxation creep characteristics, we can say that not only does the tissue exhibit lesser viscoelastic accommodation, but also that this accommodation takes longer to occur, particularly the first two thirds which are represented by the short-term characteristic, τ_1, where we see a more significant increase.

As we move to the epicardia, Figure 4.14, we notice that the short term relaxations are still on the order of 0.10 seconds but that the trend has changed. Hypertensive tissues no longer seem to undergo longer relaxation times but rather seem to complete their short term relaxation process more quickly than their healthy counterparts, particularly in the left ventricle. This is also the case for the long-term relaxation where we observe significantly reduced relaxation times, especially in the left ventricle. This is an interesting finding as Figure 4.11 demonstrates that there is no consistent

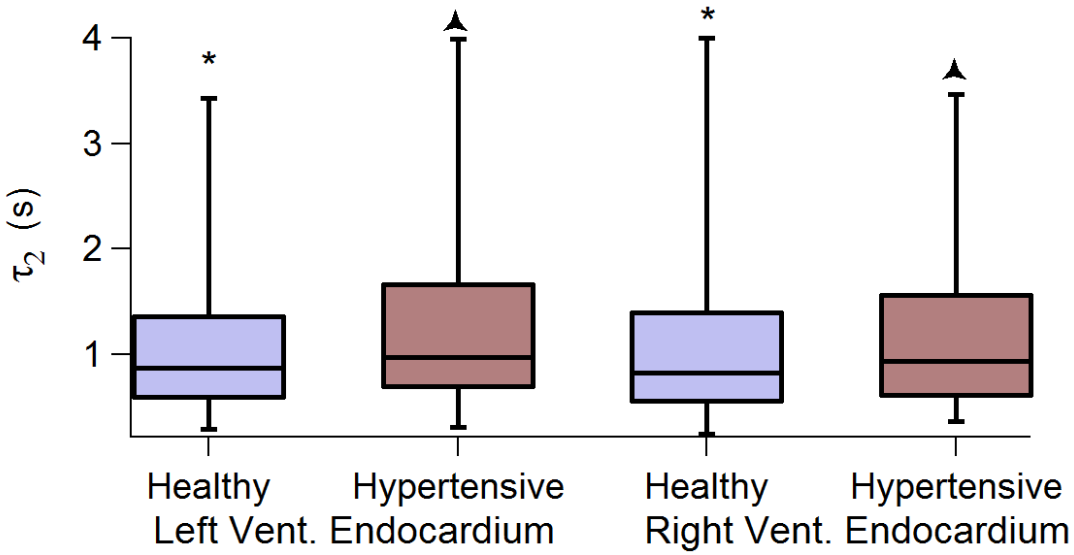

Figure 4.13: Box plots showing distribution of long-term relaxation times, τ_2, for healthy and hypertensive ventricular endocardia.N=8000 per box.

trend in creep magnitude between healthy and hypertensive tissues in the epicardium. This would tell us that while the magnitude of creep occurring, as a generalization, does not change, the timeline along which the final third of this relaxation occurs takes place decreases. This would indicate that the epicardia undergo the same degree of creep accommodation, but at a much faster rate than in the normotensive animal.

That the endocardium undergoes changes that decrease the amount of creep and also lengthen the time over which this accommodation occurs tell us that the rate of creep deformation of these tissues in response to a constant force is impaired on two levels. Seeing that the time-scale of relaxation in the epicardia is shortened while there is no consistent or generalized alteration to creep magnitude indicates that hypertension affects cardiac tissues differentially. This is likely related to differing responses of the various tissue components as has been previously discussed in this work.

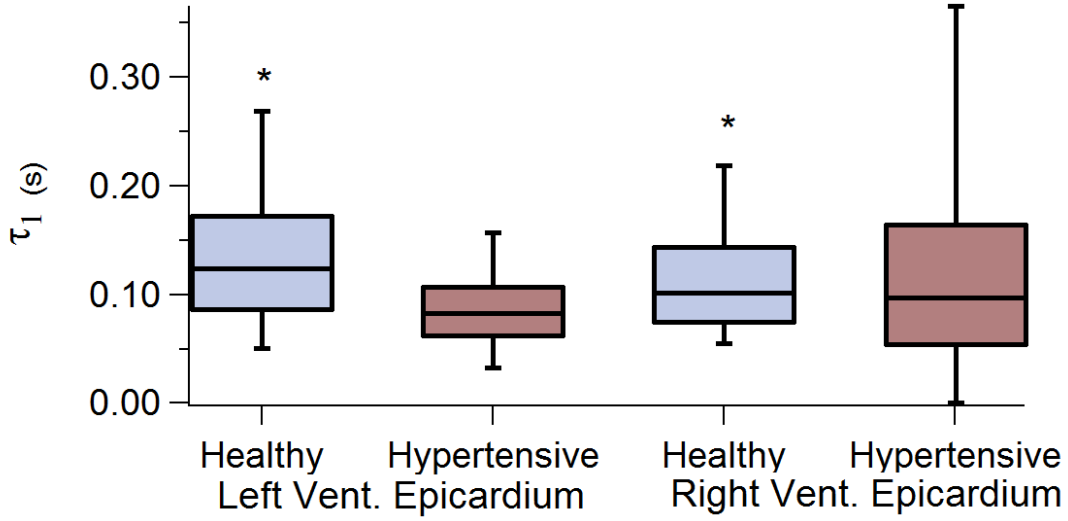

Figure 4.14: Box plots showing distribution of short-term relaxation times, τ_1, for healthy and hypertensive ventricular epicardia.

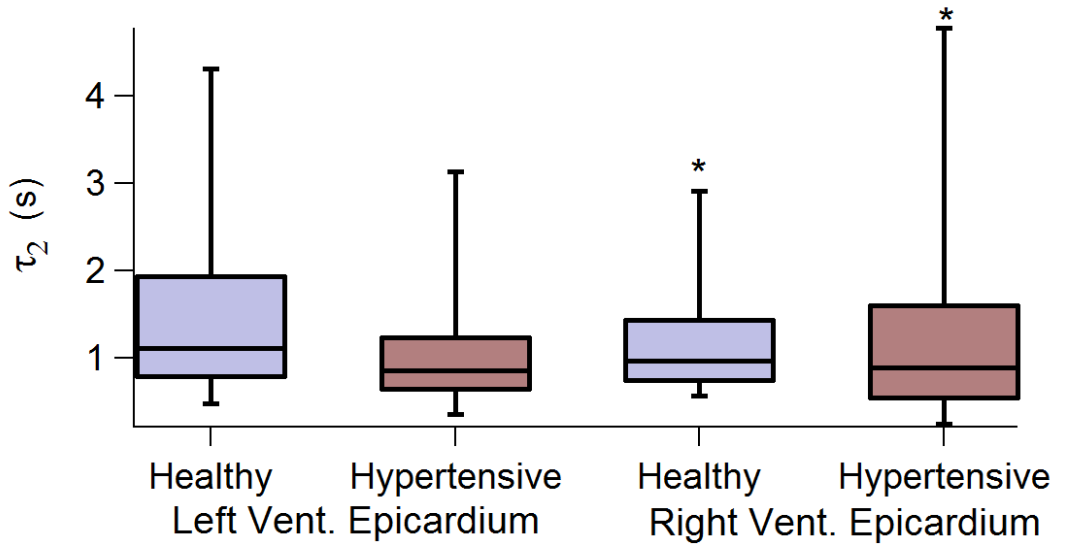

Figure 4.15: Box plots showing distribution of long-term relaxation times, τ_2, for healthy and hypertensive ventricular epicardia.

4.4 Conclusions

Here the use of nanoindentation force spectroscopy has enabled investigation of the native and hypertensive nanomechanics of the epicardium and endocardium. Moreover, it is likely that the behaviour of the myocardium contributes to the observed behaviours of each aforementioned layer and therefore has been characterized in some indirect capacity.

While the effects of hypertension upon the heart are less direct and much less intuitive than in vasculature they are still significant. Left ventricular hypertrophy in particular has been associated with bulk-scale mechanical changes in the heart that some have linked, hierarchically, to changes occurring in the orientation, type, and proportion of collagen fibrils at the level of cardiomyocytes. The work detailed in this chapter provides nanomechanical evidence extracted from hydrated tissues. Our findings elucidate these mechanical changes to have a nanoscale origination. Nanomechanical differences between the left and right ventricles, the epi and endocardium, and healthy and hypertensive tissues have been elucidated.

Endocardial elasticization has been observed a result of hypertension in both ventricles. We suspect this may relate strongly to an interplay of endocardial fibrosis and myocyte death, both a result of ventricular hypertrophy and sub-optimal perfusion resulting from both the hypertrophy itself and also from altered wave-reflect timing. This is conceived to occur in what can be delineated as two distinct phases. Firstly, myocote loss occurs due to an ischaemic state which decreases myocyte density in the subendocardium. Force spectroscopy at this time would occur upon tissues with a decreased number of myocytes for a constant, or increased tissue volume. It could be construed that a tissue of this nature would allow greater indentation for a given force and so would demonstrate more significant elasticity. Sometime after this period of myocyte loss we would expect to see significant fibrosis occurring through fibroblast

mediated fibrillogenesis. Once the tissue has become fibrotic we would expect to see much less elastic indentations. This being said, this may provide a time line at which subendocardial myocyte loss occurs and fibrosis has yet to occur significantly as the rats used in this work were all 12-14 weeks. This same behaviour is observed though to a much smaller magnitude in the epicardium as may be expected since ischaemia and subsequent myocyte loss will occur first in the subendocardial layer.

During our investigation of creep behaviour we found the epicardium to exhibit no consistent or meaningful trends. This is not unexpected as the epicardium is not expected to have a significant viscoelastic function as both the endocardium and thicker myocardium, being more internal and mechanically relevant, are predominantly responsible for cardiac suction behaviour. Our finding of decreased viscoelastic creep in the endocardium of the hypertensive creature then sits well and is likely indicative, should it scale to the bulk, of impaired cardiac suction. At the same time, we notice that the right ventricle exhibits much less viscoelasticity in both strains of rats. Being concerned solely with pulmonary circulation there would exist no major requirement for negative right ventricular pressures to create a suction effect. Analysis of short and long-term creep characteristics also indicates that the endo and epicardial viscoelastics are affected deferentially by hypertension. Specifically, the rate of endocardial accommodation is decreased while we see an increase in the epicardium.

The above being said, it is apparent that the heart undergoes nanomechanical changes as a result of the structural remodelling that occurs with hypertension. Much like in the aorta then, we can now reasonably suggest hypertension to have a nanoscale pathogenesis bringing about conditions such as left ventricular hypertrophy, myocardial ischaemia, and cardiac fibrosis.

Bibliography

[1] M. Roman, A. Ganau, P. Saba, R. Pini, T. Pickering, and R. Devereux. Impact of Arterial Stiffening on Left Ventricular Structure. *Hypertension*, 36(4):489, 2000.

[2] S. Laurent, P. Boutouyrie, R. Asmar, and I. Gautier. Aortic stiffness is an independent predictor of all-cause and cardiovascular mortality in hypertensive patients. *Hypertension*, 37(5):1236, 2001.

[3] F. Angeli, G. Reboldi, M. Trapasso, A. Aita, D. Turturiello, and P. Verdecchia. Hypertensive Heart Disease. pages 189–212. Springer, New York, United States, 2018.

[4] J. Capasso, T. Palackal, and G. Olivetti. Left ventricular failure induced by long-term hypertension in rats. *Circulation Research*, 66(5):1400, 1990.

[5] D. Levy, M. Larson, R. Vasan, W. Kannel, and K. Ho. The Progression From Hypertension to Congestive Heart Failure. *JAMA: The Journal of the American Medical Association*, 275(20):1557, 1996.

[6] D. Westermann, M. Kasner, and P. Steendijk. Role of left ventricular stiffness in heart failure with normal ejection fraction. *Circulation*, 117(16):2051, 2008.

[7] C. Lawes, S. Vander Hoorn, and A. Rodgers. Global burden of blood-pressure-related disease, 2001. *Lancet*, 371(9623):1513, 2008.

[8] D. Susic, E. Nunez, and K. Hosoya. Coronary hemodynamics in aging spontaneously hypertensive and normotensive Wistar Kyoto rats. *Hypertension*, 16(2):231, 1998.

[9] S. Lewington, R. Clarke, N. Qizilbash, R. Peto, and R. Collins. Age-specific relevance of usual blood pressure to vascular mortality: a meta-analysis of individual

data for one million adults in 61 prospective studies. *Lancet*, 360(9349):1903, 2002.

[10] J. Jalil, C. Doering, J. Janicki, and R. Pick. Fibrillar collagen and myocardial stiffness in the intact hypertrophied rat left ventricle. *Circulation*, 64(6):1041, 1998.

[11] B. Borlaug, C. Lam, V. Roger, R. Rodeheffer, and M. Redfield. Contractility and Ventricular Systolic Stiffening in Hypertensive Heart Disease: Insights Into the Pathogenesis of Heart Failure With Preserved Ejection Fraction. *Journal of the American College of Cardiology*, 54(5):410, 2009.

[12] A. Sironi, A. Gastaldelli, A. Mari, and D. Ciociaro. 2004.

[13] G Iacobellis, D Corradi, AM Sharma Nature Reviews Cardiology, and undefined 2005. Epicardial adipose tissue: anatomic, biomolecular and clinical relationships with the heart. *nature.com*.

[14] A. M. Sironi, A. Pingitore, S. Ghione, D. De Marchi, B. Scattini, V. Positano, E. Muscelli, D. Ciociaro, M. Lombardi, E. Ferrannini, and A. Gastaldelli. Early Hypertension Is Associated With Reduced Regional Cardiac Function, Insulin Resistance, Epicardial, and Visceral Fat. *Hypertension*, 51(2):282–288, 2008.

[15] M. Kozàkovà, F. Galetta, L. Gregorini, and G. Bigalli. Coronary vasodilator capacity and epicardial vessel remodeling in physiological and hypertensive hypertrophy. *Hypertension*, 36(3):343, 2000.

[16] T. Weber, J. Auer, M. O'Rourke, and E. Kvas. Arterial stiffness, wave reflections, and the risk of coronary artery disease. *Circulation*, 109(2):184, 2004.

[17] A. Mathur, G. Truskey, and W. Monty Reichert. Atomic Force and Total Internal Reflection Fluorescence Microscopy for the Study of Force Transmission in Endothelial Cells. *Biophysical Journal*, 78(4):1725, 2000.

[18] V. Vedula, J. Seo, A. Lardo, and R. Mittal. Effect of trabeculae and papillary muscles on the hemodynamics of the left ventricle. *Theoretical and Computational Fluid Dynamics*, 30(1):3, 2016.

[19] A Pasipoularides. *Heart's vortex: intracardiac blood flow phenomena*. People's Medical Publishing House, Connecticut, United States, 2009.

[20] S. Bishop, S. Oparil, R. Reynolds, and J. Drummond. Regional myocyte size in normotensive and spontaneously hypertensive rats. *Hypertension*, 1(4):378, 1979.

[21] E. Balse, D. Steele, H. Abriel, A. Coulombe, D. Fedida, and S. Hatem. Dynamic of Ion Channel Expression at the Plasma Membrane of Cardiomyocytes. *Physiological Reviews*, 92(3):1317, 2012.

[22] M. Wheeler, M. Allikian, A. Heydemann, and E. McNally. The sarcoglycan complex in striated and vascular smooth muscle. *Cold Spring Harbor Symposia on Quantitative Biology*, 67(1):389, 2002.

[23] B. Burlew and K. Weber. Cardiac Fibrosis as a Cause of Diastolic Dysfunction. *Herz*, 27(2):92, 2002.

[24] K. Weber. From inflammation to fibrosis: a stiff stretch of highway. *Hypertension*, 43(4):716, 2004.

[25] K. Weber. Cardiac interstitium in health and disease: the fibrillar collagen network. *Journal of the American College of Cardiology*, 13(7):1637, 1989.

[26] R. Brown, S. Ambler, M. Mitchell, and . Long. The Cardiac Fibroblast: Therapeutic Target in Myocardial Remodeling and Failure. *Annual Review of Pharmacology and Toxicology*, 45(1):657, 2005.

[27] C. Beltrami, N. Finato, M. Rocco, G. Feruglio, C. Puricelli, E. Cigola, F. Quaini, E. Sonnenblick, G. Olivetti, and P. Anversa. Structural basis of end-stage failure in ischemic cardiomyopathy in humans. *Circulation*, 89(1):151, 1994.

[28] C. Rosendorff, H. Black, C. Cannon, B. Gersh, J. Gore, J. Izzo, N. Kaplan, C. O'Connor, P. O'Gara, and S. Oparil. Treatment of Hypertension in the Prevention and Management of Ischemic Heart Disease: A Scientific Statement From the American Heart Association Council for High Blood Pressure Research and the Councils on Clinical Cardiology and Epidemiology and Prevention. *Hypertension*, 50(2):e28, 2007.

[29] P. Kong, P. Christia, and N. Frangogiannis. The pathogenesis of cardiac fibrosis. *Cellular and Molecular Life Sciences*, 71(4):549, 2014.

[30] H. Kanai. Propagation of spontaneously actuated pulsive vibration in human heart wall and in vivo viscoelasticity estimation. *IEEE Transactions on Ultrasonics*, 52(11):1931, 2005.

[31] S. Nikolic, K. Tamura, and T. Tamura. Diastolic viscous properties of the intact canine left ventricle. *Circulation*, 67(2):352, 1990.

[32] A. Moreo, G. Ambrosio, B. Chiara, and M. Pu. Influence of myocardial fibrosis on left ventricular diastolic function: non-invasive assessment by CMR and echo. *Circulation*, 2(6):437, 2000.

[33] D. Kass, J. Bronzwaer, and W. Paulus. What mechanisms underlie diastolic dysfunction in heart failure? *Circulation Research*, 94(12):1533, 2004.

[34] P. Palmiero, A. Zito, M. Maiello, M. Cameli, P. Modesti, M. Muiesan, S. Novo, P. Saba, P. Scicchitano, R. Pedrinelli, and M. Ciccone. Left ventricular diastolic function in hypertension: methodological considerations and clinical implications. *Journal of Clinical Medicine Research*, 7(3):137, 2015.

Chapter 5

Conclusions

5.0.1 Hypertension-Induced Nanomechanical Dysfunction Across the Arterial Wall

Minimal nanoindentation AFM techniques have been used to investigate the differental viscoelastics of a variety of hydrated cardiovascular tissues. Prior work, reviewed in Chapter 2, has found the nanoscale elasticity of the tunica adventitia to be an order of magnitude greater than that of the intima. This had also been found to be the case on the bulk-scale where the adventitia is understood to support the majority of the vascular load. [1] In that work thoracic tissues were also seen to demonstrate greater stiffness than those of the abdomen. Across both the intima and adventitia there was an occurrence of significant hypertension-induced nanoscale stiffening. In this work we found the muscular tunica media to be mechanically distinct from the intima and adventitia and was also seen to be stiffer in the thoracic region than the abdominal. The healthy tunica media was found to exhibit elasticity comparable to the tunica intima. However, hypertensive remodelling was observed in the form of significant collagen infiltration which produced a ten-fold stiffening of the tissue. This is by far

the most significant hypertensive alteration across the three arterial layers.

Profuse nanoscale stiffening across the differential arterial layers can be expected to decrease aortic distensibility and contributes to cyclical pressure induced stiffening where stiffening brings about greater pressures which in turn cause further tissue damage and subsequent stiffening. This progressive insult can lead to conditions such as aortic aneurysm and subsequent rupture.

More significant than alterations to elasticity are those to the viscoelastic behaviours of the arteries. These behaviours including the Windkessel effect, discussed in Section 1.2, also demonstrated distinctions between thoracic and abdominal tissues as well as amongst the three arterial layers. The tunica media was found to exhibit the smallest viscoelastic deformation of the three layers and, consequently, is considered to the the primary determinant of whole-artery viscoelasticity. The media, like the intima and adventitia, demonstrates significantly reduced viscoelastic creep in hypertensive tissues. It then follows that hypertension negatively impacts the viscoelastic capacity of the aorta as a whole. Specifically, these changes are likely indicative of mitigated and temporally altered Windkessel behaviour as indicated by the changes in τ_1 and τ_2. Changes of this nature hinder the ability of the aorta to dissipate pulsatile energy, increase cardiac afterload, alter the sensitive timing of wave reflections returning to perfuse the coronary circuit, and impair continued diastolic blood flow.

5.0.2 Hypertensive Remodelling in the Heart Induces Nanomechanical Dysfunction

The structure and function of the heart is also intrinsically linked to that of the arteries, particularly those proximal to the left ventricle such as the aorta. This is even more so the case in hypertensive pathologies. Here, direct investigation of the epi and endocardial layers with likely indirect contributions from the myocardium have

shown mechanical alterations to occur as a result of hypertension in addition to some mechanical distinction between different tissues that exist throughout. Particularly speaking, we observe endocardial (and likely subendocardial) elasticization occurring in the SHR strain at 12-14 weeks. As an explanation for this seemingly counterintuitive finding, we suggest that myocyte loss due to subendocardial ischaemia, prior to the onset of fibrosis, will produce a tissue with decreased cellular density that can be reasonably expected to exhibit greater elasticity. Both myocardial ischaemia and cardiac fibrosis are intrinsically connected to the development of left ventricular hypertorphy, a common presentation of hypertensive heart. Unsurprisingly, the epicardium was found to exhibit no significant trends in its elastic behaviour which likely follows from the relative mechanical unimportance of this layer.

The heart not only undergoes elasticizing changes with hypertension but has also been found to experience viscoelastic changes in addition to having mechanical distinct ventricular behaviours even prior to hypertension. Though there exists far less research in the domain of cardiac viscoelasticity it is understood to be primarily involved in the cardiac suction effect in which collagen fibres play a significant role. Irrespective of tissue health, the right ventricle is much less viscoelastic in nature in both strains of rats in terms of its endocardial behaviour which likely relates to the differing requirements for a suctioning behaviour in order to pump for pulmonary circulation c.f. systemic circulation. Hypertensive remodelling produces a far less viscoelastic endocardium in the left ventricle, which would reasonably impair cardiac suction behaviour. It could be possible that this impairment results from alterations to collagen type, proportion, and distributon in the perimysium which would serve to essentially constrain the viscoelastic behaviour arising from myocytes. Ultimately, a lesser negative pressure in the ventricle could decrease venous return which would subsequently decrease cardiac output.

5.0.3 Qualitative Relationships Between Nanoscale Elasticity and Viscoelasticity

Investigation of the relationship between arterial elasticity and viscoelasticity suggests a convoluted, qualitative relationship. Interestingly, it appears that hypertension alters these distributions differentially in varying tissues. Reasonably, this may be due to different components of the tissue exhibiting different responses to hypertension. I.E. collagen fibres may respond differently than elastin and so on. Compositionally different sites would then be expected, to show different responses to hypertension for this reason.

5.1 Future Directions

5.1.1 Arterial De-stiffening and Risk Mitigation

In hypertensive populations, mitigation of cardiovascular risk is inherently intertwined with decreased systolic blood pressure. [2] Unfortunately, even following reduction of hypertensive blood pressures, residual cardiovascular risk remains. This residual risk relates to our prior discussion of the positive-feedback cycle present between stiffer arteries and increasing blood pressures. De-stiffening of hypertensively remodelled arteries is necessary to diminish this residual risk. [3]

While antihypertensives primarily function to directly decrease arterial blood pressure, there is some evidence to suggest that certain antihypertensives may also action de-stiffening of damaged vasculature. [4] AFM based nano-indentation methods would allow for further investigation of this suspected phenomenom. Subsequent elucidation of the mechanism of antihypertensive based direct tissue re-elasticization. Such investigation would likely require local exposure of tissues to antihypertensive

medications followed by nanomechanical analysis in order to eliminate the potential for secondary de-stiffening deriving from decreased blood pressures.

Determination of which antihypertensives, if any, demonstrate direct de-stiffening properties has far reaching implications. Firstly, elucidation of the chemical functionalities which contribute to these effects might allow for two important advances: (i) de-stiffening therapy in non-hypertensive individuals in order to reverse age-induced arterial stiffening, and (ii) mitigation of residual risk in post-hypertensive individuals whereby a return to native arterial elasticity is achieved while normal blood pressure ranges are maintained. Secondly, if a selective pharmaceutical inhibitor of collagen cross-linking can be identified we may be able to stall arterial stiffening which occurs naturally with age. [5]

5.1.2 Nanomechanical and Topographical Investigation of the Myocardium

The myocardium is the primary site of remodelling in hypertensive heart pathologies. However, due to the geometric arrangement of myocytes, the bulbosity of the tissue, and difficulties with cross-sectional AFM imaging of the myocardium this important layer proved inaccessible for direct imaging. While increased indentation depths on the endo and epicardium in this work likely provided some indirect information on this tissues behaviour future work should seek to provide direct confirmation.

During this work, topographical analysis should be conducted on both the healhy and hypertensive myocardium in order to hopefully identify changes in myocyte size and/or density. Additionally, it may be that perimyasial collagen fibrils can be located. Subsequently, the changes undergone by these mechanically and structurally important elements in hypertensive pathologies could be indentified.

Investigation into this line of research may help to elucidate nanomechanical changes

associated with left ventricular hypertrophy and provide a mechanical understanding to support the current biochemically-based arguments.

Bibliography

[1] C. Schulze-Bauer, P. Regitnig, and G. Holzapfel. Mechanics of the human femoral adventitia including the high-pressure response. *American Journal of Physiology: Heart and Circulatory Physiology*, 282(6):H2427, 2002.

[2] M. Safar, J. Blacher, and P. Jankowski. Arterial stiffness, pulse pressure, and cardiovascular disease-is it possible to break the vicious circle? *Atherosclerosis*, 218(2):263–71, 2011.

[3] R. Zimlichman. Treatment of hypertension and metabolic syndrome: lowering blood pressure is not enough for organ protection, new approach-arterial destiffening. *Current Hypertension Reports*, 16(10):479, 2014.

[4] C. Koumaras, M. Tzimou, E. Stavrinou, T. Griva, T. Gossios, N. Katsiki, V. Athyros, D. Mikhailidis, and A. Karagiannis. Role of antihypertensive drugs in arterial 'de-stiffening' and central pulsatile hemodynamics. *American Journal of Cardiovascular Drugs : Drugs, Devices, and other Interventions*, 12(3):143–56, 2012.

[5] H. Kayed, K. Sizeland, N. Kirby, A. Hawley, S. Mudie, and R. Haverkamp. Collagen cross linking and fibril alignment in pericardium. *Royal Society of Chemistry Advances*, 5(5):3611, 2015.

Appendix A

Energy of Viscous Dissipation

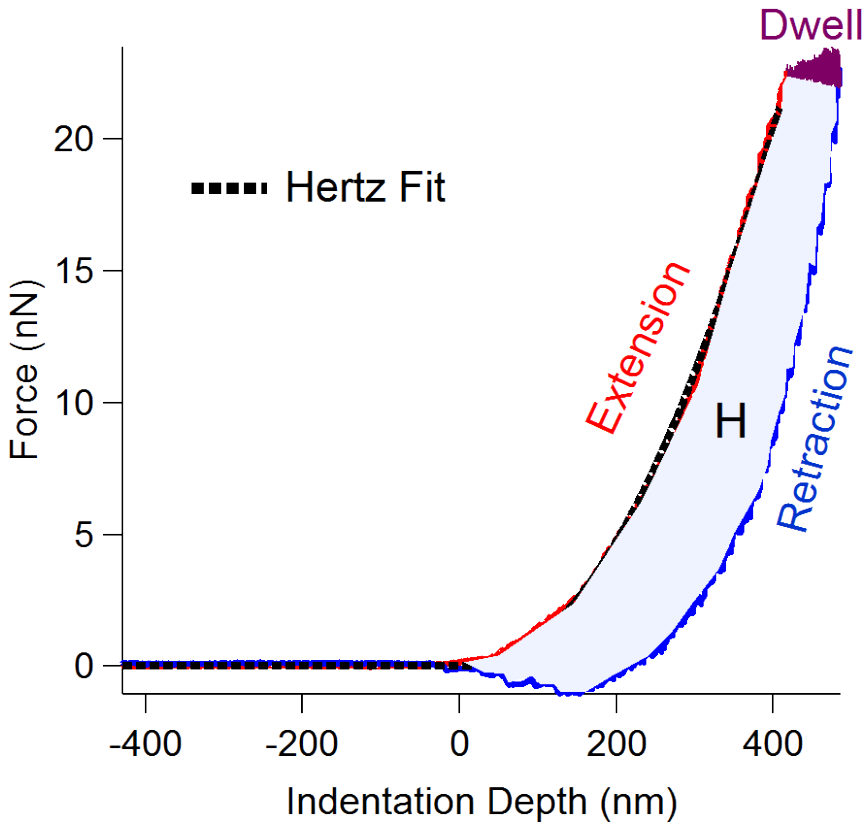

Figure A.1: Typical force spectroscopy experiment with dwell phase. Area of hysteresis, H, used to determine energy of viscous dissipation shaded in light blue.

In addition to investigating viscoelasticity in terms of creep indentation and the

associated creep-characteristics, $\tau_{1,2}$, we can also investigate the hysteresis present in force curves. The area, representing the overlap between force and indentation distance, incident between the extension and retraction curves can be identified as the energy of viscous dissipation. During extension the tip progressively indents deeper into the sample via function of an applied force. In doing so energy, here the energy of indentation, is input into the system. This means that hysteresis between the extension and retraction cycles is then indicative of a change in energy and, where we see lesser energies during retraction, can be identified as energy lost to viscous dissipation.

As has been discussed in Chapter 1 and further in Section 1.2 the dissipation of pulsatile energy in the proximal aorta is of primary interest. The aorta is known to demonstrate significant viscoelastic behaviour via the Windkessel effect and, in this work, has shown notable creep accommodation. Therefore the aorta very likely dissipates the majority of this pulsatile energy through viscous dissipation.

In order to enable estimation of the area of hysteresis, i.e. the energy of viscous dissipation, the CreepAnalysisAdvanced.ipf procedure presented in Appendix D can be used. This procedure will calculate the area between the extension and retraction curves, H, which can be used as an estimation of the energy of viscous dissipation. This is accomplished by taking the integral of both curves, subtracting that of the retraction curve from the approach curve, and then dividing by the area under the approach curve to normalize by the input energy, Equation A.1. [1]

$$H = \frac{\int_0^\delta F_E(\delta) - \int_0^\delta F_R(\delta)}{\int_0^\delta F_E(\delta)} \tag{A.1}$$

Comparing between the intimal, medial, and adventitial layers with mean energy values and ranges tabulated in Table A.1 we can see that the intima demonstrates the smallest dissipative capacity with energy on the order of 1,000 A.U. while the

Table A.1: Energies of viscous dissipation along with associated ranges for all arterial tissues.

Tissue	Mean Energy, H (A.U.)	Range (A.U.)
WKY-TI	$5.67\times10^{5\ddagger}$	4.80×10^{5} – 6.51×10^{5}
SHR-TI	$5.97\times10^{5\ddagger}$	4.97×10^{5} – 6.62×10^{5}
WKY-AI	8.00×10^{5}	5.08×10^{5} – 9.76×10^{5}
SHR-AI	5.53×10^{5}	2.60×10^{5} – 7.72×10^{5}
WKY-TM	$7.78\times10^{5\dagger}$	2.37×10^{5} – 9.41×10^{5}
SHR-TM	$6.82\times10^{5*}$	3.20×10^{5} – 7.07×10^{5}
WKY-AM	$7.65\times10^{5\dagger,*}$	2.57×10^{5} – 7.89×10^{5}
SHR-AM	13.4×10^{5}	5.24×10^{5} – 10.5×10^{5}
WKY-TA	10.3×10^{5}	4.23×10^{5} – 15.2×10^{5}
SHR-TA	14.1×10^{5}	5.52×10^{5} – 18.6×10^{5}
WKY-AA	9.21×10^{5}	$4.54\times10^{5\ddagger}$ – 8.91×10^{5}
SHR-AA	9.02×10^{5}	$5.06\times10^{5\ddagger}$ – 6.12×10^{5}

†Indicates statistical equivalence

media and the adventitia are on the order of 100,000-1,000,000 A.U. Additionally, the adventitial tissues are seem to have a larger dissipative capacity than the medial tissues. This is in following with previous reports that the adventitia supports the majority of the pressure load. [2] For the tunica intima we surprisingly see that there is no signficiant difference in the energy of dissipation between the healthy and hypertensive thoracic tissue. There is, however, a notable decrease in the energy dissipated by the hypertensive abdominal intima c.f. the healthy. The healthy abdominal intima also seems to have significantly more viscous dissipation than the thoracic which is contrary to the requirement of more proximal tissues to dissipate energy. However, it's worth considering that the tunica intima has relatively small mechanical contribution when compared to the media and adventitia and affects mechanical change primarily through its vasoactive capacity. It is, however, interesting that we see a consistent decrease in creep behaviour between healthy and hypertensive and also thoracic and abdominal tissues and don't see a corresponding trend in dissipation of viscous energy. In the healthy media, Figure A.3, we observe no significant difference between the dissipative abilities of the healthy thoracic and abdominal tissues. We do however see

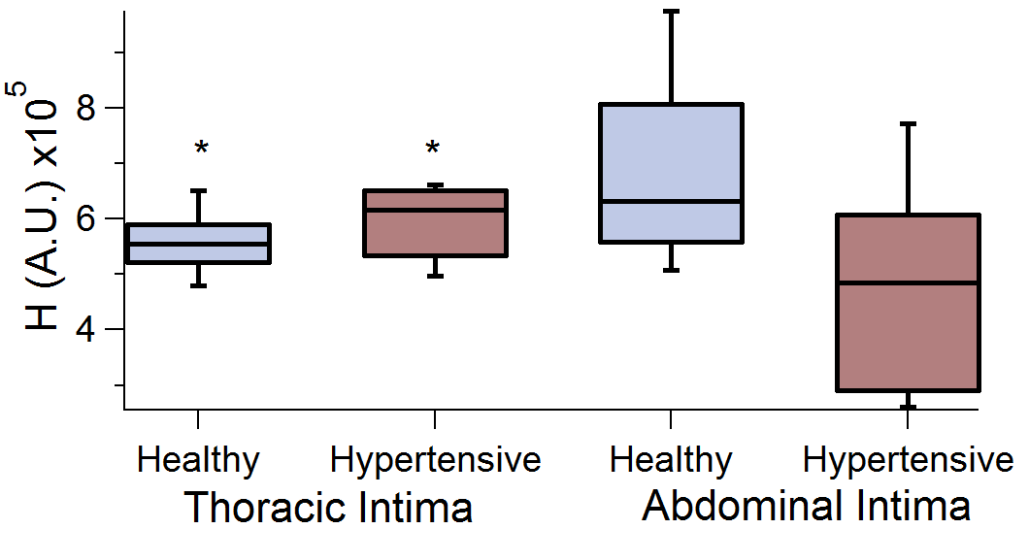

Figure A.2: Box and whisker plots showing relative magnitude of dissipated energies for healthy and hypertensive abdominal intima, N=1200 for each box.

an significant increase in the ability to dissipate energy in the hypertensive rat. This is somewhat confusing as hypertension is understood the impair bulk-scale dissipation of energies in advanced pathologies. There are two possibilities which might explain this occurrence: i) Changes in nanoscale point-dissipation are part of, or involved in, larger hierarchical changes that have an overall effect of decreasing bulk-scale energy dissipation even though we see an increase on this scale or ii) The tissues in question are at a point in the time-line of the pathology where compensatory mechanisms are causing structural changes within the aorta to try and better dissipate the increased pulsatile energies associated with hypertension. We can expect to see this compensatory behaviour become insufficient or be overpowered with time, ultimately producing tissues that are less able to dissipate energy, even at the nanoscale.

In the adventitia, the layer expected to be most significant in terms of energy dissipation, the same is as observed as in the media. Here we need to be careful and remember that the whisker plots in Figure A.4 do not show the mean value but rather the median. The mean values reported in Table A.1 make it clear the

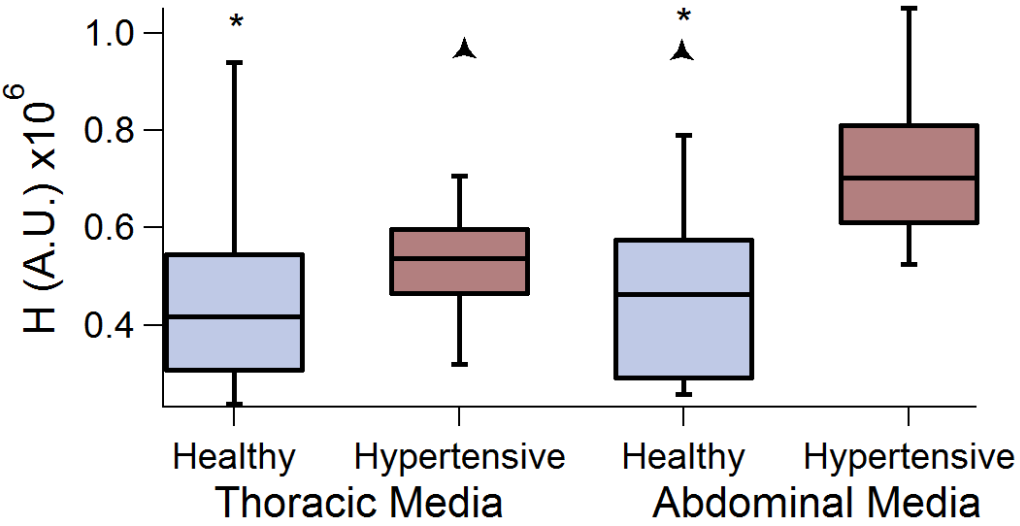

Figure A.3: Box and whisker plots showing relative magnitude of dissipated energies for healthy and hypertensive thoracic media, N=6000 for each box.

hypertensive abdominal adventitia has a greater dissipative capacity and that there exists no signficiant difference between the tissues in the abdomen.

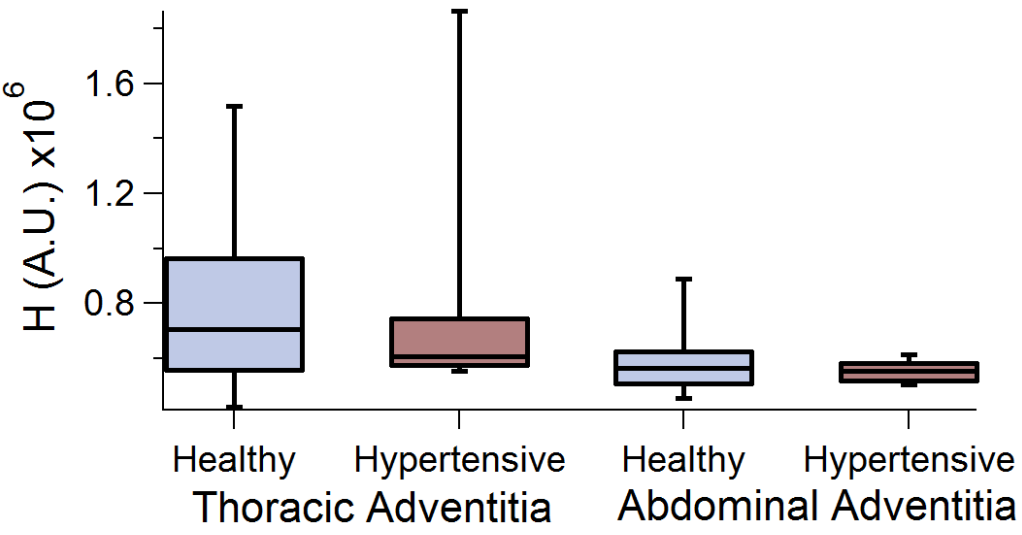

Figure A.4: Box and whisker plots showing relative magnitude of dissipated energies for healthy and hypertensive abdominal adventitia, N=1200 for each box.

Bibliography

[1] M. Papi, A. Maiorana, C. Douet, G. Maulucci, T. Parasassi, R. Brunelli, G. Goudet, and M. De Spirito. Viscous forces are predominant in the zona pellucida mechanical resistance. *Applied Physics Letters*, 102(4):43703, 2013.

[2] C. Schulze-Bauer, P. Regitnig, and G. Holzapfel. Mechanics of the human femoral adventitia including the high-pressure response. *American Journal of Physiology: Heart and Circulatory Physiology*, 282(6):H2427, 2002.

Appendix B

A Raman Investigation of Retinoids in Murine Eye Tissue

B.1 Introduction

Retinoids are vitamin A (all-E retinol) derivatives which, amongst other functions, play an important role in the vision cycle. [1] These derivatives include retinol, retinal, and retinoic acid being the alcohol, aldehyde, and acid derivatives respectively, Figure B.1. In all multicellular organisms retinoid based chromophores linked to G-protein coupled receptors (GPCRs) are the sole means through which light sensing is conducted. [2] More specifically, 11-cis retinal, is the chromophore of choice for the overwhelming majority of kingdom animalia including humans. This is the case for two primary reasons: i) Retinoid based chromophores undergo major conformational changes upon exposure to light. The magnitude of this change likely makes it easier to distinguish between the two states; and ii) when joined to the photoreceptor protein, called an opsin, the absorbance range of these compounds is shifted into the visual range where as most other light absorbing compounds absorb in the UV. [3]

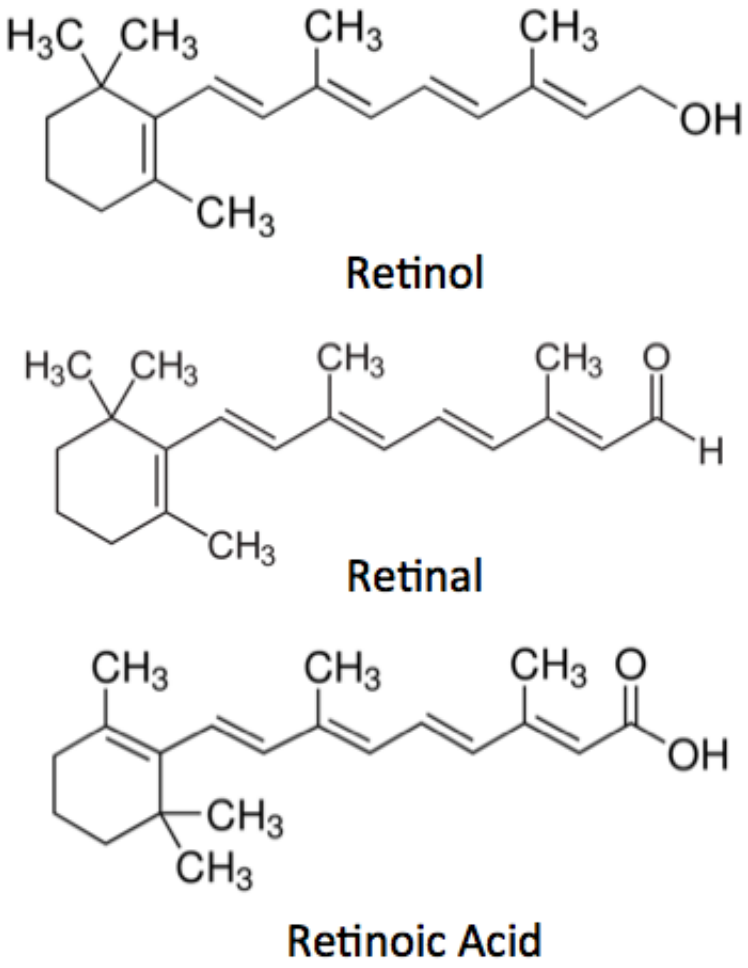

Figure B.1: Structures of the most common retinoids in their predominant physiological isomers. Respectively Retinol, all-E Retinal, and all-E Retinoic acid from top to bottom.

A large number of pathologies are associated with deficiencies or alterations in vitamin A and its derivatives. [2] For instance, vitamin A deficiency remains the leading cause of preventable blindless globally in addition to be largely responsible for the formation of the eye. [4] For this reason, the distribution, concentration, and proportion of retinoids in the retina are of particular interest. This work seeks to use Raman Spectroscopy in conjunction with AFM-based Tip Enhanced Raman Spectroscopy (TERS) to elucidate differences in these factors between healthy and pathological

tissues.

B.2 Methods

Whole eyes resected from C56B6 mice anesthetized immediately prior to collection were split hemispherically and pressed flat onto various substrates to include glass microscope slides, mica, the front side of a silicon wafer, and the reverse side of the same. Raman spectroscopy was then conducted upon each of these samples in addition to background scans. Scans were conducted with exposure times of 1 s, 20 s, and 30 s on each sample and at least 5 scans were completed at each exposure time. Additionally, the same was done with objective lenses of 10 x, 20 x, and 40 x. All scans were completed on a Renishaw 633 nm Raman spectrometer.

Extended scans were conducted over the range of 200-3200 cm^{-1}. Following this, static scans were conducted at 960 and 1620 cm^{-1} with 30 s exposure time and the 40 x objective in order to investigate regions of particular interest.

B.3 Results and Discussion

633 Raman investigation of the whole eye section on glass substrate demonstrated significant fluoresence increasing with higher magnification objective lenses. Consequently, the peaks at 1641 cm^{-1} were found to be optimized with a 30 s exposure using a 10 x objective lens, Figure B.2.

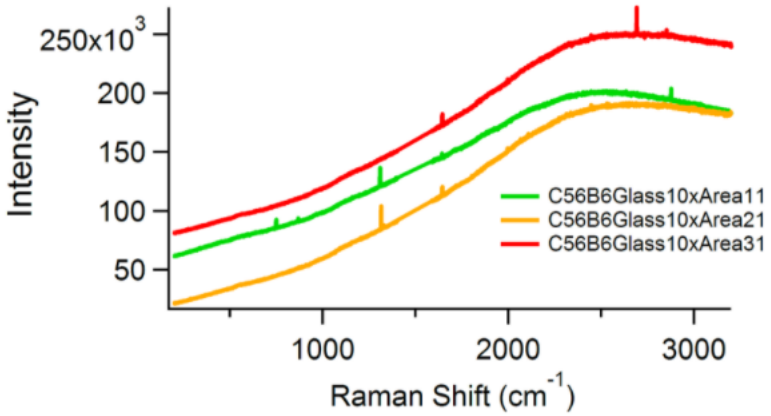

Figure B.2: Raman spectra of the C56B6 whole eye on glass substrate. Significant glass fluoresence is apparent but consistent peaks are observed at 1641 cm^{-1} that cannot be linked to the substrate.

Static scans, Figure B.3, conducted about this wavelength and then normalized within spectra using the RamanComparison procedure detailed in Appendix D.3 helped to draw out these peaks and also identify peaks at approximately 1310 cm^{-1} in two of the three spectra.

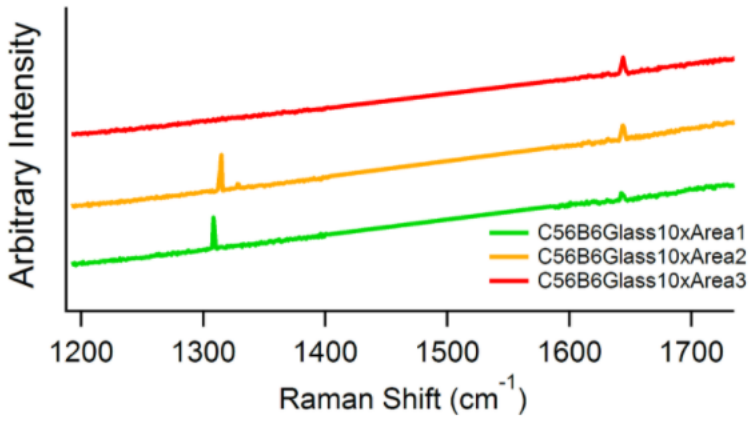

Figure B.3: Normalized static scan at 1640 cm^{-1} of the C56B6 whole eye on glass substrate. Peaks observed at 1641 cm^{-1} and unidentified peaks at 1310 cm^{-1} in two of the spectra now apparent.

The peak at 1641 cm^{-1} is comparable to a literature value of 1649 cm^{-1} for triglycerides observed recently by Liao and coworkers. [5] The 7 cm^{-1} shift can

reasonably be justified by variances in matrix possibly affecting polarizability and vibrational modes of the triglycerides themselves.

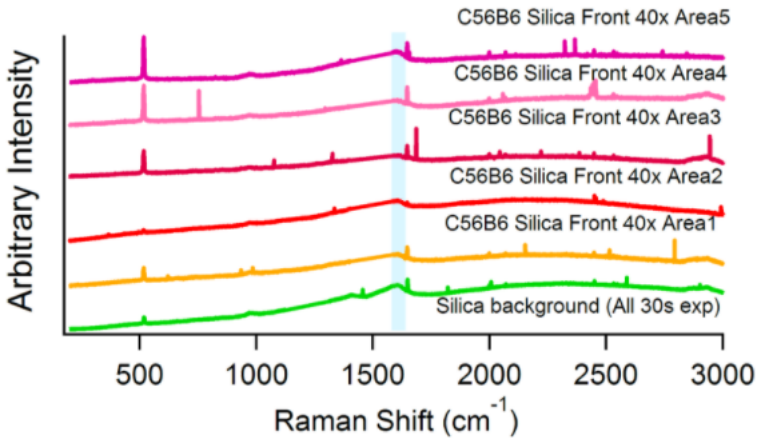

Figure B.4: Normalized Raman spectra of the C56B6 whole eye on front side of silicon front revealing fluorescence band about 1610 cm^{-1}, peaks are again seen at 1641 cm^{-1} with an additional silicon peak at 518 cm^{-1}.

Figure B.4 shows the Raman response for several areas of the mouse eye in addition to the background response (green). All scans were conducted with 30vs exposure. Once again we see a silicon peak at 518 cm^{-1} and the 1641 cm^{-1} peak previously assigned to triglycerides. The band about 1610 cm^{-1} also reoccurs here and several of the spectra seem to have a peak about 960 cm^{-1}, however, this also seems to be present in the background spectrum.

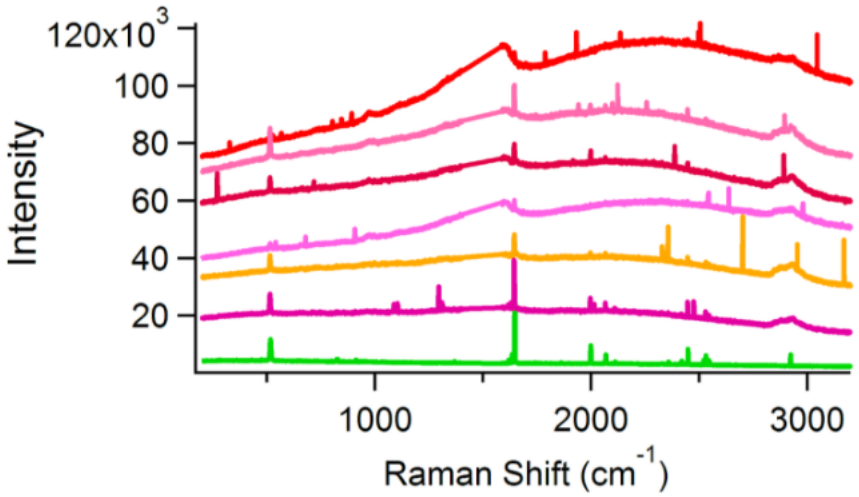

Figure B.5: Normalized Raman spectra of the C56B6 whole eye on reverse side of silicon revealing fluorescence band about 1600 cm^{-1} now resulting only from sample scans. Peaks are again seen at 1641 cm^{-1} with an additional silicon peak at 518 cm^{-1}.

However in Figure B.5 we see that the fluorescence band around 1610 cm^{-1} is no longer present in the background spectrum (green) from the reverse side of the silicon wafer. This would suggest that not only does the front side of the wafer show fluoresence in this region, but also the eye tissue itself which is unsurprising considering the magnitude of conjugation present in these light-sensitive components of eye tissues. Particularly, both retinoic acid and retinol are expected to contribute to this band as they have been found to give Raman signals at 1582 and 1610 cm^{-1}, respectively.

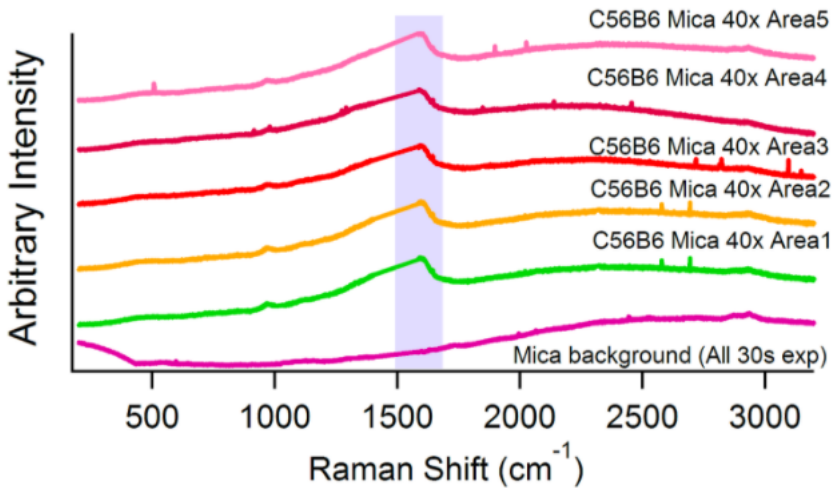

Figure B.6: Normalized Raman spectra of the C56B6 whole eye on Mica confirming sample related fluoresence at 1600 cm^{-1}. Vague suggestion of a triglyceride peak at 1641 cm^{-1} along with recurrent peak at 965 cm^{-1}.

Figure B.6 confirms that the eye sample itself gives rise to a fluoresence band indicated by a blue trace at roughly 1600 cm^{-1}, where there is no apparent Raman activity whatsoever on the substrate spectrum (purple). The supposed triglyceride peaks also reappear in a few of the spectra. In order to get a better understanding of the peak around 965 cm^{-1}, we conduct a static scan about this region, Figure B.7.

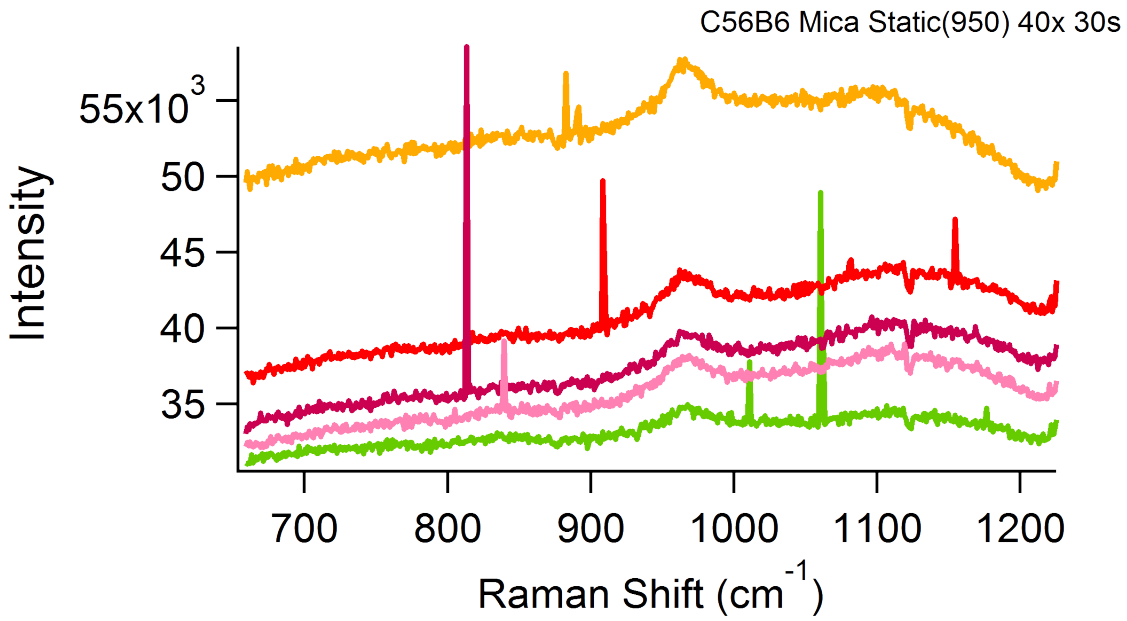

Figure B.7: Static scan Raman spectra about 950 cm^{-1} of confirming presence of a Retinal peak at 965 cm^{-1}.

These static scan were centered about 950 cm^{-1} and captured with 30 s exposure time on the 40 x objective lens. These experiments reveal a definite peak centered at 965 cm^{-1}. all-E retinal has previously been identified to be represented by a Raman peak about 972 cm^{-1} . [6] Considering the known Retinal density of the tissues investigated here it is quite likely that we are observing the presence of Retinal. Once again, a shift of 7 cm^{-1} is well within reason when considering matrix and experimental effects upon the vibrational behaviour of a molecule. The static scans centered about 1620 cm^{-1} in Figure B.8 also help to better represent a consistent triglyceride peak at 1641 cm^{-1} as well as very consistent fluoresence peaking around 1610 cm^{-1}. Additionally, there is a very interesting and consistent dips in intensity about 1770 cm^{-1}.

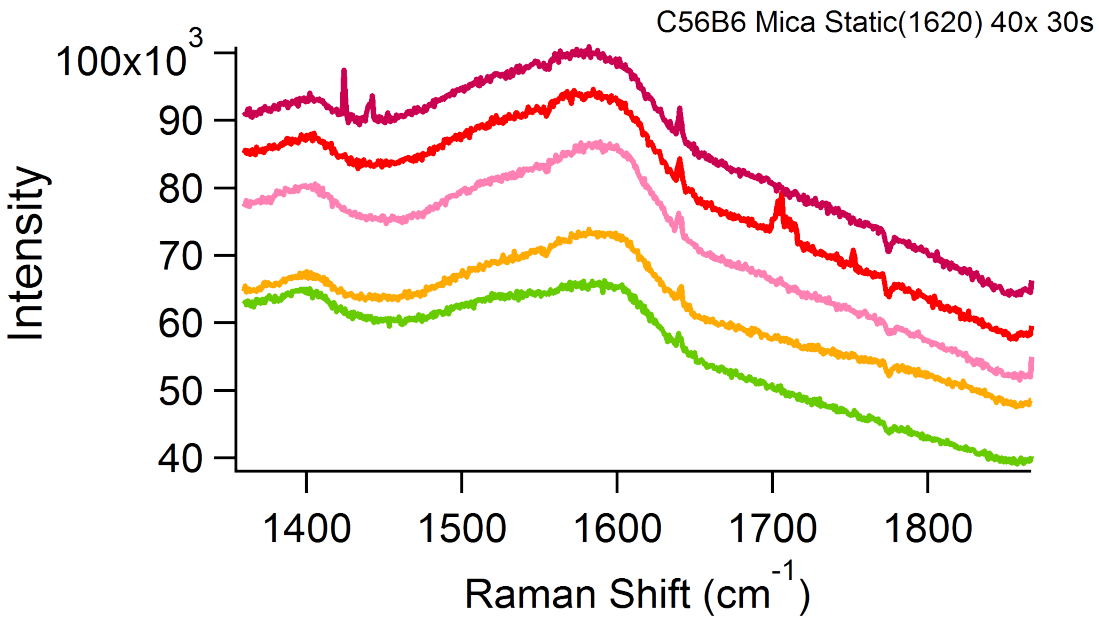

Figure B.8: Static Raman scan about 1620 cm^{-1} of the C56B6 whole eye on Mica confirming sample related fluoresence at 1600 cm^{-1} and triglyceride peak at 1641 cm^{-1}.

Figure B.9 displays the Raman spectra of retinyl acetate collected from five different sampling sites. The spectra are fairly consistent throughout and have obvious significant features in the 950-1300 and 1600 cm^{-1} regions. Apparent only in the unnormalized spectra are the consistent peaks at 972 cm^{-1} (not labelled) which match perfectly with a literature value of 927 cm^{-1} for retinal. [6] This indicates the presence of a vibrational mode common to both retinyl acetate and retinal that would give rise to this band. Considering the similarity of the two structures this can be easily justified especially if the structural component giving rise to this band is far removed from the few structural differences present. This can also be linked to our 965 cm^{-1} seen in the whole eye spectra. In this case shifting has likely occurred due to changes in chemical environment or matrix effects. The 1100-1300 cm^{-1} and 1600 cm^{-1} regions identified by faint pink and blue overlays respectively are better isolated in the normalized spectra seen in Figure B.10. In the faint pink region we can identify three peaks at

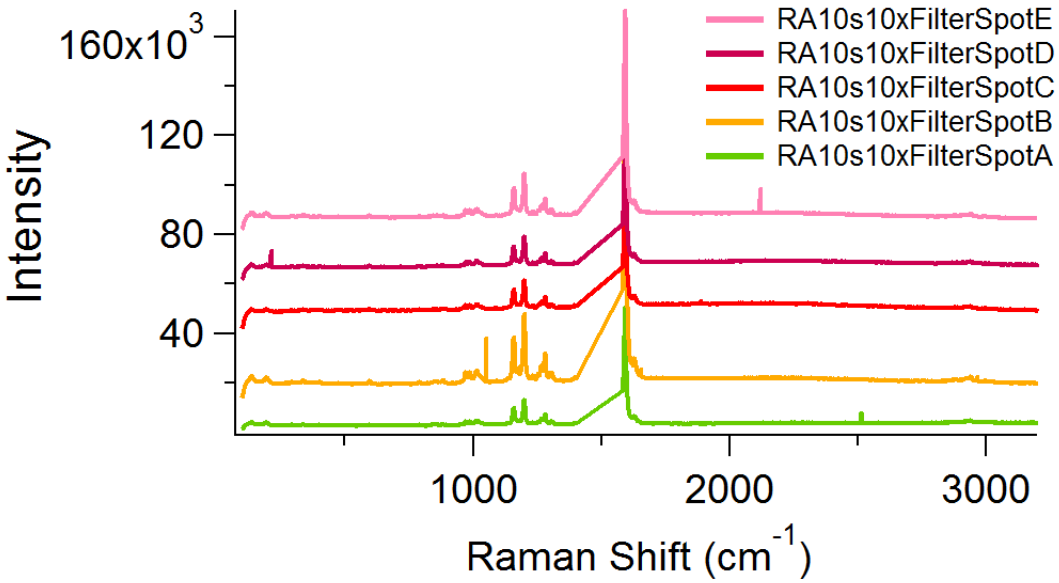

Figure B.9: Extended Raman scan of Retinyl Acetate standard under 10x objective with 10 s exposure.

1160, 1200, and 1282 respectively. The 1160 and 1200 peaks have appeared in other recent Raman investigations of retinyl acetate but have not been assigned. [7] The diagnostic peak at 1594 cm^{-1} is also present in the literature and may relate to the 1582 cm^{-1} vibrational mode discussed earlier for retinoic acid. This shifting can be related to earlier arguments. We suspect this peak to be present for the whole eye but to be buried in the fluorescence band near 1600 cm^{-1}.

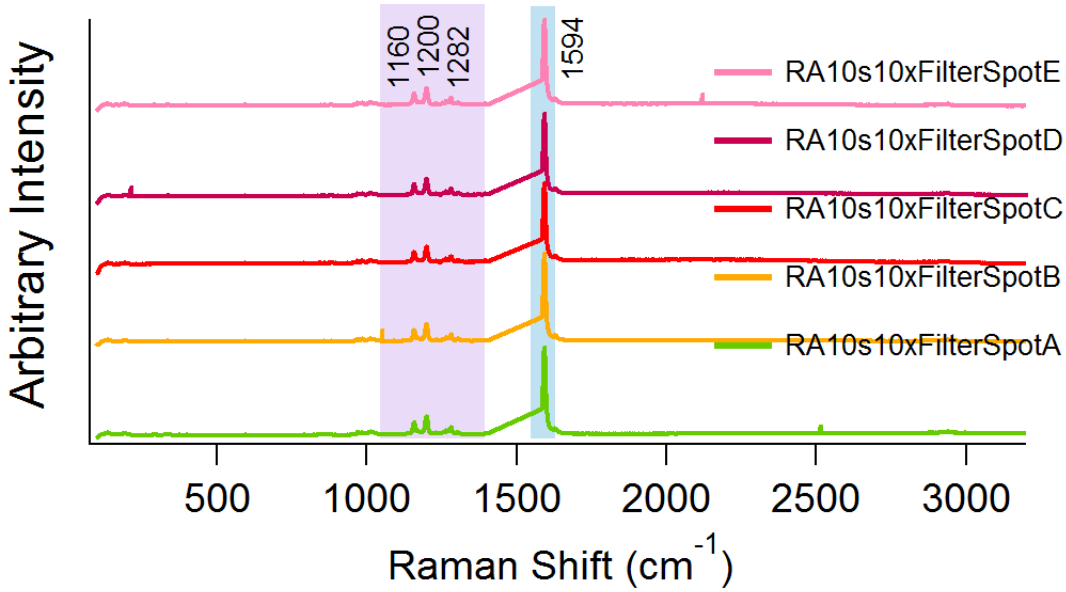

Figure B.10: Extended Raman scan of Retinyl Acetate standard under 10x objective with 10 s exposure with in-spectrum normalization, peaks of itnerest are labelled.

B.4 Conclusions

So far preliminary Raman characterization of whole eye samples has successfully identified a number of items. Firstly, mica has been determined to be the most ideal substrate as it shows no fluoresence coincident with the sample fluoresence about 1600 cm^{-1} and, at the same time, shows no other fluoresence so significant as to be obscuring of sample respone. Static scans conducted about 1620 cm^{-1} and 950 cm^{-1} on mica with 30 s exposure time and a 40 x objective lens have identified the following peaks:

1. A 965 cm^{-1} peak identified to be retinal which has a literature value of 972 cm^{-1} for one of its characteristic vibrations.

2. A fluoresence band about 1600 cm^{-1} which likely contains the response from retinoic acid and retinol with responses at 1582 and 1610 cm^{-1} respectively.

3. A discrete peak at 1641 cm^{-1} related to triglyceride response with a literature

value of 1649 cm^{-1}.

Small departures of from literature vibrations can be justified by contributions of the complex matrix about the molecules in question likely altering their characteristic vibrations.

B.4.1 Future Directions

Our current course of action involves seeking to confirm that the observed vibrations have been assigned correctly. This is being done through two approaches. Firstly, computational Raman spectrum for each target compound is being generated. Comparison between these spectra and our peaks of interest will hopefully confirm what has already been suggested in this chapter. Additionally we are looking to capture Raman spectra of standards of retinol, retinal, and retinoic acid which will also hopefully show agreement with the bands detailed here.

Following successful confirmation of our findings forward movement would be oriented to mapping spatial distributions of these compounds throughout the eye in order to produce a baseline and identify areas of particular interest. This would be accomplished through Raman mapping and is a step itself towards the use of TERS. If a TERS approach can be successfully attempted then it would provide unprecedented spatial resolution for chemical identification in addition to being coupled with AFM to yield compositional data linked to topographical data. TERS would also likely assist to overcome the fluoresence about 1600 cm^{-1} thus allowing us to identify the presence of retinoic acid and retinol which are both currently overwhelmed by the fluoresence.

Bibliography

[1] P. Kiser, M. Golczak, and K. Palczewski. Chemistry of the Retinoid (Visual) Cycle. *Chemical Reviews*, 114(1):194, 2014.

[2] M. Zhong, R. Kawaguchi, M. Kassai, and H. Sun. Retina, retinol, retinal and the natural history of vitamin A as a light sensor. *Nutrients*, 4(12):2069, 2012.

[3] S. Tseng and L. Hirst. Inhibition of conjunctival transdifferentiation by topical retinoids. *Investigative Opthamology and Visual Science*, (28):538, 1987.

[4] A. Sommer. *Vitamin A deficiency and its consequences : a field guide to detection and control*. World Health Organization, Geneva, Switzerland, 1995.

[5] C. Liao, M. Slipchenko, and P. Wang. Microsecond scale vibrational spectroscopic imaging by multiplex stimulated Raman scattering microscopy. *Light: Science & Applications*, (4):265, 2015.

[6] B. Curry, A. Broek, J. Lugtenburg, and R. Mathies. Vibrational analysis of all-trans-retinal. *Journal of the American Chemical Society*, 104(20):5274, 1982.

[7] L. dos Santos, C. Téllez S, M. Sousa, N. Azoia, A. Cavaco-Paulo, A. Martin, and P. Favero. In vivo confocal Raman spectroscopy and molecular dynamics analysis of penetration of retinyl acetate into stratum corneum. *Spectrochimica Acta Part A: Molecular and Biomolecular Spectroscopy*, 174(2):279, 2017.

Appendix C

Effect of Parameters

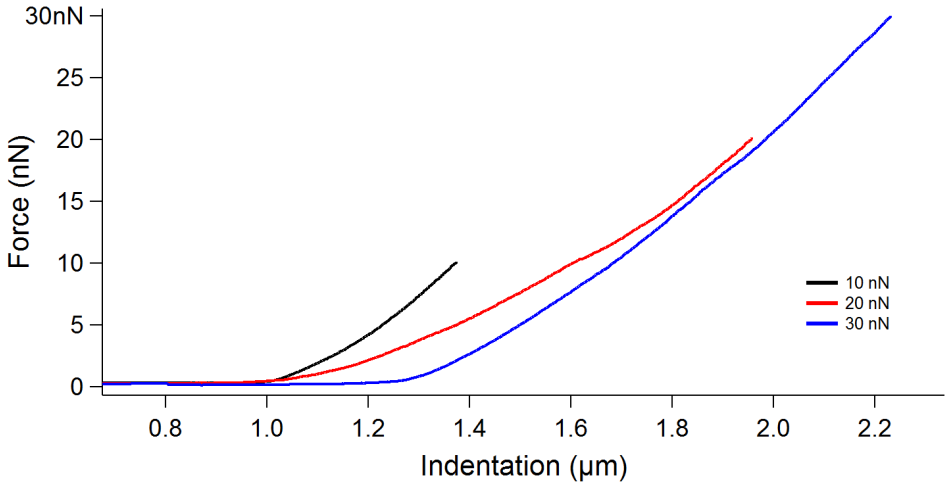

Figure C.1: Effect of increasing trigger force on indentation depth. Each curve is the smoothed average of 20 curves.

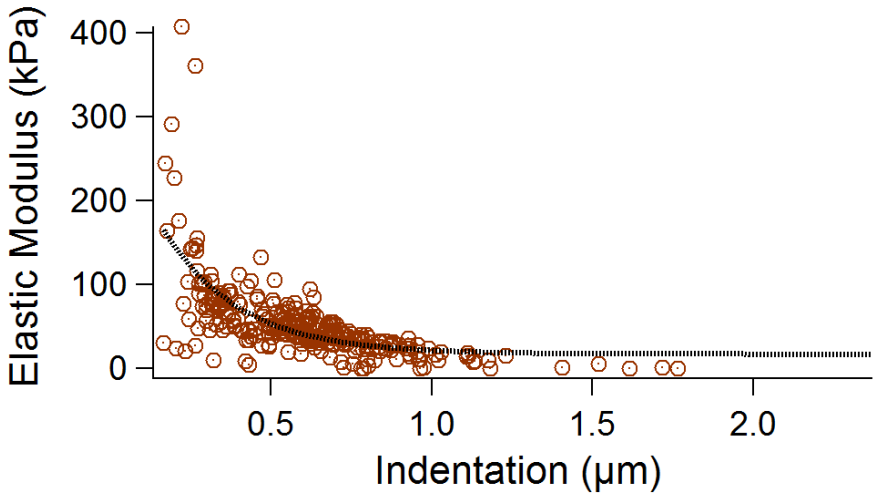

Figure C.2: Mild exponential relationship between elastic modulus and indentation taken from healthy tunica media. Direct examination is confounded by bi-exponential nature of the tissues.

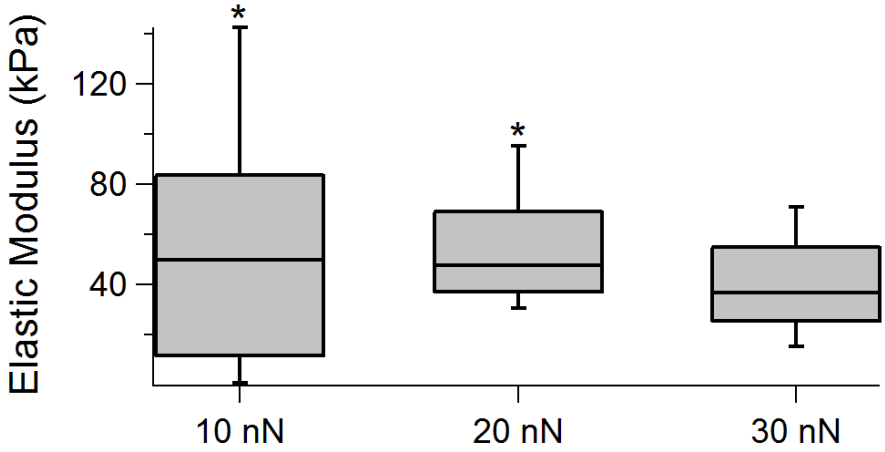

Figure C.3: Increasing trigger force seems to produce no significant difference in mean elastic modulus for healthy tunica media tissues but results in increasingly discrete distributions.N=2,000 per box.

Appendix D

Programming

D.1 Creep Analysis Procedure

The below procedure was created by myself in November of 2018 with updates as recently as May 2018 and is remodel of the original procedure I had written in October of 2017. This procedure enables the user to input infinitely many force curves in .ibw format and calculate the creep deformation for each curve using the bi-exponential model discussed in Section 1.2. If you have asked it to do so, the program will then produce statistics for the calculated creep deformation, generate a colour map showing the spatial distribution of creep and finally generate a histogram showing the numerical distribution. Additionally, advanced viscoelastic parameters related to the bi-exponential fit shown in Equation 1.7 can be determined. These parameters are the creep characteristics τ_1 (short-term) and τ_2 (long term), and the pre-exponential factors A_1 and A_2. Additionally, a new option allows the procedure to calculate the energy of viscous dissipation (area between the extension and retraction curves) and will output both a map and histogram of the energy data.

```
Function CreepAdv()
```

```
String DestFolder = BuildDataFolder(root;MyForceData;)
      String FPName, DataFolder, FPList, DataFolderList
   GetForcePlotsList(2,FPList,DataFolderList)
   Variable NameLength

   Variable i, NumOfPts = ItemsInList(FPList,;)
   Variable LastIndentIndex
   Make/O/N=(NumOfPts) CreepIndentation
   Make/O/N=(NumOfPts) CreepMap

   Variable scale// Scale of image
   String TauData, EnergyData
   Prompt scale, Enter the size of the images (in um)
   Prompt TauData, Do you want to solve for advanced viscoelastic
      parameters?, popup, No;Yes
   Prompt EnergyData, Do you want to solve for the energy of viscous
      dissipation?, popup, No;Yes
   DoPrompt Parameters, scale, TauData, EnergyData

   If (V_flag)
      return -1     // returns -1
   endif

   If(CmpStr(TauData,Yes)==0)
      Make/O/N=(NumOfPts) Tau1, A1, Tau2, A2
   EndIf
   If(CmpStr(EnergyData,Yes)==0)
      Make/O/N=(NumOfPts) Energies, EnergyMap
```

```
EndIf



for (i = 0;i < NumOfPts;i += 1)
   FPName = StringFromList(i,FPList,;)
   DataFolder = StringFromList(i,DataFolderList,;)
   Wave DestData = InitOrDefaultWave(DestFolder+FPName+Ind_Towd,0)
   Wave/Z SrcData = CalcForceDataType(DataFolder,FPName+Ind)
   if ((!WaveExists(SrcData)) || (DimSize(SrcData,0) == 0))
      Continue   //we dont have indentation data for this force plot
   endif
   ExtractForceSection(SrcData,DestData)
       LastIndentIndex=dimsize(DestData,0)
       CreepIndentation[i]=DestData[LastIndentIndex]-DestData[0]
       If(CmpStr(TauData,Yes)==0)
          CurveFit/Q=1/N=1/M=2/W=0/TBOX=(0x318) dblexp_XOffset,
              DestData[][0]/D


          Wave FitData =W_coef //W_coef is global wave created by curve
              fitting containing fit data, assign to local wave FitData
           A1[i]=FitData[1] //A1 and A2 are the pre-exponential factors
               for the first and second exponents respectively
           A2[i]=FitData[3]
           Tau1[i]=FitData[2] // Tau1[k] is the characteristic response
               time, i.e. the time reqd for 63.2% of creep deformation to
               occur
           Tau2[i]=FitData[4] // Tau2[k] is the second characteristic
               response time, i.e. the time reqd for for the last 37% of
```

```
        deformation to occur
 EndIf

 If(CmpStr(EnergyData,Yes)==0)
      Wave ExtData =
         InitOrDefaultWave(DestFolder+FPName+Force_Ext,0)
Wave RetData = InitOrDefaultWave(DestFolder+FPName+Force_Ret,0)
Wave/Z SrcData = CalcForceDataType(DataFolder,FPName+Force_Ext)
Wave/Z SrcData2 = CalcForceDataType(DataFolder,FPName+Force_Ret)
Wave ExtSep = InitOrDefaultWave(DestFolder+FPName+Sep_Ext,0)
Wave RetSep = InitOrDefaultWave(DestFolder+FPName+Sep_Ret,0)
Wave/Z SrcDataExtSep = CalcForceDataType(DataFolder,FPName+Sep_Ext)
Wave/Z SrcDataRetSep = CalcForceDataType(DataFolder,FPName+Sep_Ret)

if ((!WaveExists(SrcData)) || (DimSize(SrcData,0) == 0))
      Print No Indentation data for this plot
   Continue   //we dont have indentation data for this force plot
endif

ExtractForceSection(SrcData,ExtData) //extracts Ext wave into
    DestDate
ExtractForceSection(SrcData2,RetData)//Extracts ret wave into
    DestData2
ExtractForceSection(SrcDataExtSep,ExtSep)
ExtractForceSection(SrcDataRetSep,RetSep)
    //Display ExtData vs ExtSep
    //AppendToGraph RetData vs RetSep
```

```
        //   Print Area(ExtData,wavemin(ExtSep),wavemax(ExtSep))
        // Print Area(RetData) //,wavemin(RetSep),wavemax(RetSep))
           Energies[i]=Abs(Area(ExtData,wavemin(ExtSep),wavemax(ExtSep))-Area(RetData)),
        EndIf

endfor
Edit CreepIndentation
Print The creep indentation statistics are;
Wavestats CreepIndentation
ARHistogram(CreepIndentation,CreepDeformation,0)  //make a histogram.
ModifyGraph fSize=14;DelayUpdate
Label left \\Z16Counts;DelayUpdate
Label bottom \\Z16Creep Deformation (nm)\\u#2
SetAxis/A



String MapName
NameLength=Strlen(Datafolderlist)/NumOfPts
MapName=DataFolderList[0,NameLength-2]+CreepMap

CreepMap=CreepIndentation
Redimension/N=(Sqrt(NumOfPts),Sqrt(NumOfPts)) CreepMap
Duplicate/O CreepMap MapName
Display;AppendImage MapName
ModifyImage MapName ctab= {*,*,Rainbow,0} // Displays stiffness map
   under rainbow colour scale.
ModifyGraph margin(right)=120 // Changes margin to display colour scale
   properly
```

```
ModifyImage MapName ctab= {*,*,Rainbow,1} // Reverses colour scale
ColorScale/C/N=text0/A=RC/X=5.51/Y=4.32/E image=MapName Creep
    Deformation (m)

NewFreeAxis leftAxis
SetAxis leftAxis, 0, scale
NewFreeAxis /B bottomAxis
SetAxis bottomAxis, 0, scale
Label leftAxis Position (um)
Label bottomAxis Position (um)
ModifyGraph lblPosMode(leftAxis)=1, lblPosMode(bottomAxis)=1
ModifyGraph freePos(leftAxis)=0, freePos(bottomAxis)=0
ModifyGraph lblPos(leftAxis)=0, lblPos(bottomAxis)=0
ModifyGraph axRGB(left)=(65535,65535,65535),
    tlblRGB(left)=(65535,65535,65535), alblRGB(left)=(65535,65535,65535)
ModifyGraph axRGB(bottom)=(65535,65535,65535),
    tlblRGB(bottom)=(65535,65535,65535),
    alblRGB(bottom)=(65535,65535,65535)

    Duplicate/O CreepMap LayerData
    wave LayerData
   LayerData=CreepMap
    //Sort Creep table from lowest to highest
  //  sort creepIndentation, creepindentation
      If(CmpStr(TauData,Yes)==0)
   AppendToTable tau1, tau2, A1, A2
   EndIF
```

```
If(CmpStr(EnergyData,Yes)==0)
   AppendToTable Energies
   Print The energy of viscous dissipation statistics are;
Wavestats Energies
ARHistogram(Energies,DissipationEnergy,0)  //make a histogram.
ModifyGraph fSize=14;DelayUpdate
Label left \\Z16Counts;DelayUpdate
Label bottom \\Z16Energy of Dissipation \\u#2
SetAxis/A

String MapName2
NameLength=Strlen(Datafolderlist)/NumOfPts
MapName2=DataFolderList[0,NameLength-2]+EnergyMap

EnergyMap=Energies
Redimension/N=(Sqrt(NumOfPts),Sqrt(NumOfPts)) EnergyMap
Duplicate/O EnergyMap MapName2
Display;AppendImage MapName2
ModifyImage MapName2 ctab= {*,*,Rainbow,0} // Displays stiffness map
   under rainbow colour scale.
ModifyGraph margin(right)=120 // Changes margin to display colour
   scale properly
ModifyImage MapName2 ctab= {*,*,Rainbow,1} // Reverses colour scale
ColorScale/C/N=text0/A=RC/X=5.51/Y=4.32/E image=MapName2 Energy (J)

NewFreeAxis leftAxis
SetAxis leftAxis, 0, scale
NewFreeAxis /B bottomAxis
```

```
        SetAxis bottomAxis, 0, scale
        Label leftAxis Position (um)
        Label bottomAxis Position (um)
        ModifyGraph lblPosMode(leftAxis)=1, lblPosMode(bottomAxis)=1
        ModifyGraph freePos(leftAxis)=0, freePos(bottomAxis)=0
        ModifyGraph lblPos(leftAxis)=0, lblPos(bottomAxis)=0
        ModifyGraph axRGB(left)=(65535,65535,65535),
            tlblRGB(left)=(65535,65535,65535),
            alblRGB(left)=(65535,65535,65535)
        ModifyGraph axRGB(bottom)=(65535,65535,65535),
            tlblRGB(bottom)=(65535,65535,65535),
            alblRGB(bottom)=(65535,65535,65535)
        EndIf
        DeleteNaNNumWave(Creepindentation) //Prunes NaN values from creep
            table.
        DeleteNaNNumWave(tau1)
        DeleteNaNNumWave(tau2)
        DeleteNaNNumWave(A1)
        DeleteNaNNumWave(A2)
        DeleteNaNNumWave(Energies)
End


Function DeleteNaNNumWave(W)
Wave W
String OldName = NameofWave(W)
String NewName = OldName+_woNaNs
ConvertNumWvToTxtWv(W)
DeleteNaNTextwave(TxtConvert)
```

```
ConvertTxtWvToNumWv(WwoNaNs)
Duplicate /O NumConvert $NewName
End

// Handy Function to convert numeric waves into text waves
Function ConvertNumWvToTxtWv(W)
Wave W
Variable np = numpnts(W)
Make /T /O /N=(np) TxtConvert
Variable x
for(x=0;x<np;x+=1)
   TxtConvert[x] = num2str(W[x])
endfor
End

// Handy Function to delete NaNs from TextWaves;
Function DeleteNaNTextwave(W)
Wave /T W
Duplicate /T /O W WwoNaNs
Variable Points = numpnts(WwoNaNs)
InsertPoints Points,1, WwoNaNs // Insert trailing NaN to make
    loop-break-condition work
Variable i=0, NOP
   Do
   NOP = numpnts(WwoNaNs)
   if((strlen(WwoNaNs [i]) == 0)||(cmpstr(,WwoNaNs [i]) ==
       0)||(cmpstr(NaN,WwoNaNs [i])==0))
      DeletePoints i, 1, WwoNaNs
```

```
      i = 0 // Start over again
   else
   i = i+1
   endif
   while(strlen(WwoNaNs[NOP])==0) // see above
End

// Handy Function to convert text waves into numeric waves
Function ConvertTxtWvToNumWv(W)
Wave /T W
Variable np = numpnts(W)
Make /O /N=(np) NumConvert
Variable x
for(x=0;x<np;x+=1)
   NumConvert[x] = str2num(W[x])
endfor
End
```

D.2 Automated Raman Plotting

The RamanPlot.ipf procedure was written by myself in November and December of 2017. This procedure was written to automate the graphing of Raman spectra in order to expedite post-collection data preparation for other group members. The procedure will also automatically offset and color the loaded spectra and also provides two normalization options. Upon calling the function RamanPlot() the user will be prompted to selected any number of spectra (stored as white space delimited text files)

to plot.

Normalization is completed in one of two ways; i) intraspectrum normalization and ii) interspectra normalization. When intraspectrum or indvidual normalization is selected, the all intensity values of a spectrum will be divided by the maximum intensity of that spectrum. This will result in all intensity values for the spectrum in question falling between 0 and 1. If interspecra normalization, herein simply called normalization, is selected then the maximum intensity value across all spectra will be determined and all intensity values for all loaded spectra divided by that maximum value.

When normalization has been completed individually, Figure D.1, we label this arbitrary normalization. Conversely, interspectra normalization, Figure D.2 retains it s comparative significance.

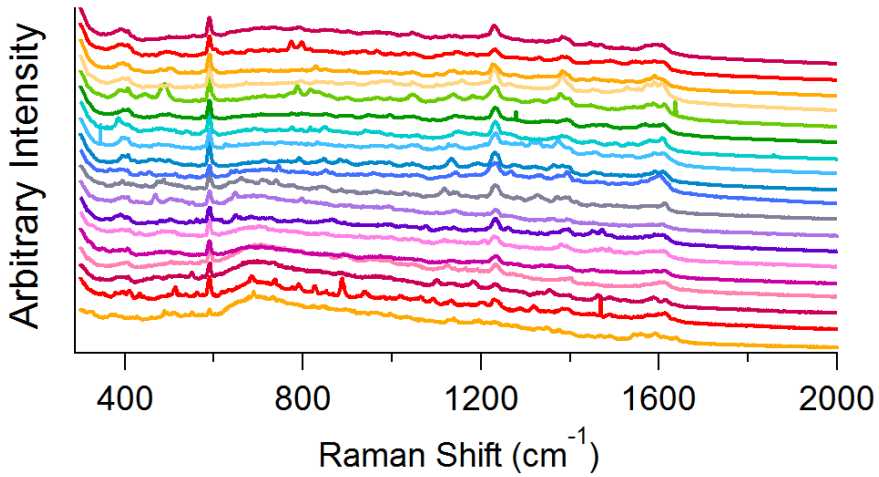

Figure D.1: RamanPlot.ipf generated Raman plot for 20 spectra with intraspectrum normalization.

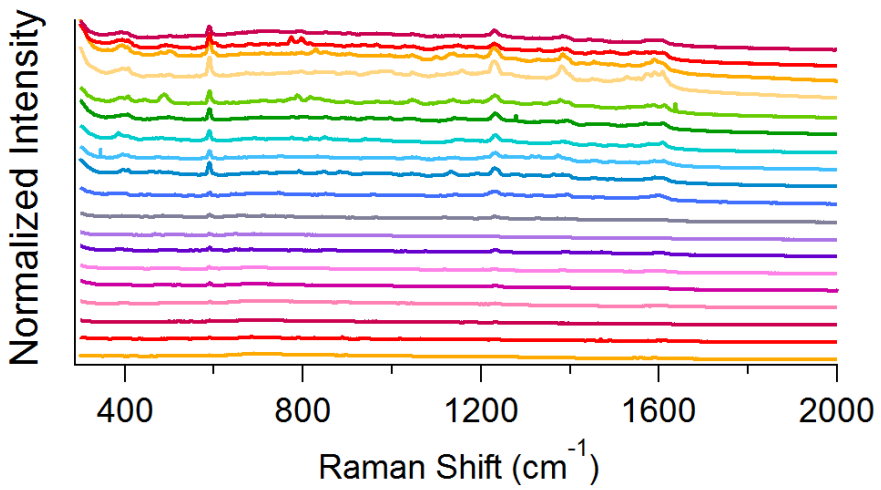

Figure D.2: RamanPlot.ipf generated Raman plot for 20 spectra with interspectra normalization.

```
// This procedure loads and plots multiple raman spectra from .txt files
   delimited by whitespace with shift values in the first column and
   intensity values in the left column. These files cannot have column
   headers.
// The governing function RamanPlot() calls LoadOnePlot which loads and
   graphs each spectrum iteratively and finds the max intensity value of
   each spectrum. This intensity value is returned to RamanPlot() which
   finds the biggest intensity value across all the spectra.
// Note; LoadOnePlot removes all values corresponding to Raman shift less
   than 300. This can be removed/changed by altering;
//   DeletePoints 2116,300, IntensityWave;
//   DeletePoints 2116,300, ShiftWave;
// Once loaded and graphed by LoadOnePlot, RamanPlot passes the maximum
   intensity value found to AlterTraces() which divides each plot
   pointwise by this maximum value to normalize each plot (if
   normalization is selected). AlterTraces() also automatically colors and
```

```
    offsets all plots.

//Written; Dec 2017
// Garrett McDougall, GGM877@MUN.CA

Function/S RamanPlot()
   Variable refNum
   String message = Select one or more files
   String outputPaths
   String fileFilters = Data Files (*.txt,*.dat,*.csv);.txt,.dat,.csv;
   fileFilters += All Files;.*;

   Open /D /R /MULT=1 /F=fileFilters /M=message refNum
   outputPaths = S_fileName
   String Normalize
   Prompt Normalize, Do you wish to normalize your spectra?, popup,
      Yes;Yes, Individually; No
   DoPrompt Normalize?, Normalize

      Display

   if (strlen(outputPaths) == 0)
      Print Cancelled
   else
      Variable numFilesSelected = ItemsInList(outputPaths, \r)
      Variable i,overallmax , Biggest=0
      for(i=0; i<numFilesSelected; i+=1) //iterates until out of files
         String path = StringFromList(i, outputPaths, \r) //loads ith files
```

```
            location to path
        //Printf %d; %s\r, i, path                                    //prints
            iteration and path
        LoadOneSpectra(, path, normalize, overallmax) //Loads ith file
        If(overallmax>Biggest)                                      //checks
            if overallmax for intensity from LoadOneSpectra
           biggest=overallmax                                       //is
               ibgger than running max biggest
        EndIf
      endfor
   endif
   ModifyGraph fSize=14;DelayUpdate

    If(CmpStr(Normalize,Yes)==0)
       Label left \\Z16Normalized Intensity\\u#2;DelayUpdate
       ModifyGraph nticks(left)=0,lblPosMode(left)=3,lblPos(left)=30
       Elseif(CmpStr(Normalize,Yes, Individually)==0)
       Label left \\Z16Arbitrary Intensity\\u#2;DelayUpdate
       ModifyGraph nticks(left)=0,lblPosMode(left)=3,lblPos(left)=30
       else
        Label left \\Z16 Intensity \\U;DelayUpdate
       EndIf
       Label bottom Raman Shift (cm\\S-1\\M)
    AlterTraces(Biggest,Normalize)
       Legend/C/N=text5/F=0/B=1/X=-8.00/Y=-10.00

   return outputPaths    // Will be empty if user canceled
End
```

```
//////////////////////////
//////////////////////////

Function LoadOneSpectra(pathName, filePath,normcheck, MaxFound) //readd
    normcheck if normalizing
   String pathName    // Name of Igor symbolic path or
   String filePath    // File name, partial path relative to symbolic path,
      or full path
      String NormCheck
      Variable &MaxFound //Pointer

   String fileName = ParseFilePath(3, filePath, ;, 0, 0) // Get file name
      without extension



   String baseShiftName = Shift
   String baseIntensityName =
   Variable baseMaxNameLength =
      max(strlen(baseShiftName),strlen(baseIntensityName))
   Variable maxIgorNameLength = 31

   // This is to make sure that your wave names dont wind up being too
      long for Igor to handle
   Variable clippedFileNameLength = maxIgorNameLength - baseMaxNameLength
   String clippedFileName = fileName[0,clippedFileNameLength-1]
   // Print clippedFileName // For debugging only
```

```
String columnInfoStr =
columnInfoStr += N= + baseShiftName + clippedFileName + ;
columnInfoStr += N= + baseIntensityName + clippedFileName + ;
// Print columnInfoStr // For debugging only

LoadWave/A/G/D/B=columnInfoStr/K=0/P=$pathName filePath  // Load waves

String wavesLoadedList = S_waveNames // S_waveNames is created by
    LoadWave
   String firstName = StringFromList(0, wavesLoadedList)
   Wave ShiftWave = $firstName               // Wave containing shift
      values
   String secondName = StringFromList(1, wavesLoadedList)
   Wave IntensityWave = $secondName    //Wave with corresponding
      intensity values
   DeletePoints 2116,200, IntensityWave;
   DeletePoints 2116,200, ShiftWave;

    If(CmpStr(NormCheck,Yes)==0)
         MaxFound=WaveMax(IntensityWave)
         AppendToGraph IntensityWave vs ShiftWave
         Return(MaxFound)
    ElseIf(CmpStr(NormCheck,Yes, Individually)==0)
          MaxFound=WaveMax(IntensityWave)
          IntensityWave=IntensityWave/MaxFound
          AppendToGraph IntensityWave vs ShiftWave
    Else
          AppendToGraph IntensityWave vs ShiftWave
```

```
      EndIf


End

////////////////////
////////////////////


Function AlterTraces(ScalingValue, NormCheck)            // colors traces
    with different colors
      Variable ScalingValue
      String NormCheck
   String Traces  = TraceNameList(,;,1)        // get all the traces from
       the graph
   Variable Items = ItemsInList(Traces)          // count the traces
   Make/FREE/N=(14,3) colors = {{65280,54528,32768}, {65280,43520,0},
       {65280,0,0}, {52224,0,20736}, {65280,32768,45824}, {52224,0,41728},
       {65280,32768,58880}, {26368,0,52224}, {44032,29440,58880},
       {32768,32768,39680}, {16384,28160,65280}, {0,34816,52224},
       {16384,48896,65280}, {0,52224,52224}, {0,39168,0}, {26112,52224,0},
       {65280,54528,32768}, {65280,43520,0}, {65280,0,0}, {52224,0,20736},
       {65280,32768,45824}, {52224,0,41728}, {65280,32768,58880},
       {26368,0,52224}, {44032,29440,58880}, {32768,32768,39680},
       {16384,28160,65280}, {0,34816,52224}, {16384,48896,65280},
       {0,52224,52224}, {0,39168,0}, {26112,52224,0}}
   Variable i,offset=0
   for (i = 0; i<DimSize(colors,1); i += 1)
```

```
        ModifyGraph
            rgb($StringFromList(i,Traces))=(colors[0][i],colors[1][i],colors[2][i])
             // set new colors
        ModifyGraph lsize($StringFromList(i,Traces))=2
         If(CmpStr(NormCheck,Yes)==0)
                 ModifyGraph
                     muloffset($StringFromList(i,Traces))={0,1/ScalingValue}
                EndIf
                ModifyGraph offset($StringFromList(i,Traces))={0,offset}
           offset+=0.25
    endfor
    ModifyGraph offset($StringFromList(0,Traces))={0,0}
End
```

D.3 Raman Comparison

RamanComparison is a procedure written by myself in late December 2017. This procedure uses some of the framework from the previous RamanPlot procedure but handles its plotting and comparison within the primary function to simplify wave management. When called, the procedure will iteratively compare all possible unique and non-self combinations of selected spectra and also provide the option to graph the loaded spectra. Two comparison scores are generated; i) the raw score and ii) the relative score. These scores are calculated as follows;

1. The pointwise product of intensity is taken between the two spectra under consideration for each value of Raman shift. Mathematically, P_i=$I_{1,i} \cdot I_{2,i}$ where I_i is the intensity value at the i^{th} shift for the designated wave.

2. We take the sum of all the pointwise products for two given spectra. The sum value is the raw score. That is to say, Raw Score=$\sum_{n=0}^{j} I_i$ where j is the number of intensity data points.

3. To determine the relative score, the largest raw score of all spectral comparisons is determined and each raw score is divided by this value.

Consequently, a larger raw score is indicative of a better agreement between the two spectra in question and a relative score closer to 1 indicative of the same. It is noteworthy that a relative score of 1 does not mean that two spectra are identical, but rather that they are the two most similar amongst all of the loaded spectra. Sample output can be found in Figure D.3 and Figure D.4.

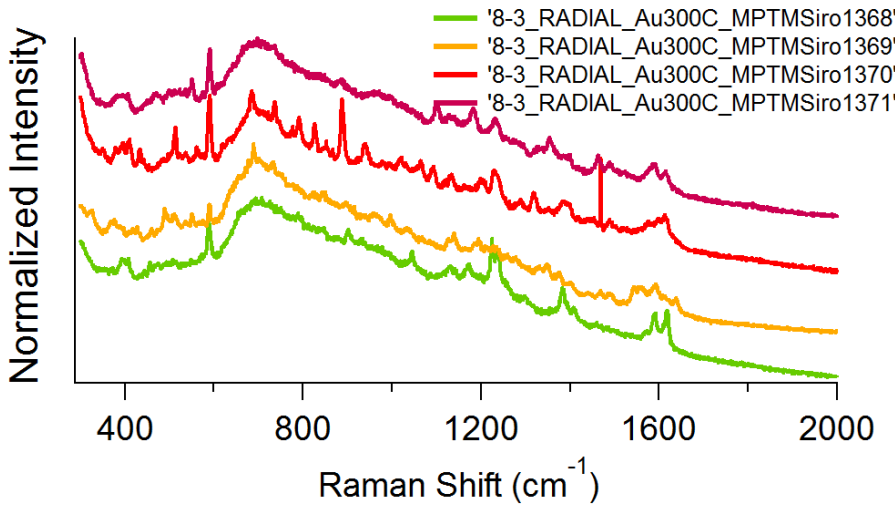

Figure D.3: RamanComparison.ipf generated Raman plot for 4 spectra with intraspectrum normalization for visual comparison of spectral similarity.

RawScore	RelativeScore	FirstWave	SecondWave
636.362	0.874443	8-3 RADIAL Au300C MPTMSiro1368	8-3 RADIAL Au300C MPTMSiro1369
691.474	0.950173	8-3 RADIAL Au300C MPTMSiro1368	8-3 RADIAL Au300C MPTMSiro1370
727.734	1	8-3 RADIAL Au300C MPTMSiro1368	8-3 RADIAL Au300C MPTMSiro1371
598.818	0.822853	8-3 RADIAL Au300C MPTMSiro1369	8-3 RADIAL Au300C MPTMSiro1370
630.848	0.866866	8-3 RADIAL Au300C MPTMSiro1369	8-3 RADIAL Au300C MPTMSiro1371
686.055	0.942728	8-3 RADIAL Au300C MPTMSiro1370	8-3 RADIAL Au300C MPTMSiro1371

Figure D.4: RamanComparison.ipf generated table of raw and relative similarity scores of all unique combinations of four selected Raman spectra.

```
// This procedure loads multiple raman spectra from .txt files delimited
   by whitespace with shift values in the first column and intensity
   values in the left column. These files cannot have column headers.

//The procedure then compares spectra on the basis of pointwise intensity
   and generates a raw and relative score with larger raw values and
   relative values closer to 1 being indicative of better similarity
   between the two indicated spectra.

//Note; This procedure removes all values corresponding to Raman shift
   less than 300. This can be removed/changed by altering;
//   DeletePoints 2116,300, IntensityWave;
//   DeletePoints 2116,300, ShiftWave;



//Written; Dec 2017
// Garrett McDougall, GGM877@MUN.CA

Function/S RamanComparison()
   Variable refNum
```

```
String message = Select one or more files
String outputPaths
String fileFilters = Data Files (*.txt,*.dat,*.csv);.txt,.dat,.csv;
fileFilters += All Files;.*;
Variable j,k=0

Open /D /R /MULT=1 /F=fileFilters /M=message refNum
outputPaths = S_fileName

   String Graph
Prompt Graph, Do you want your spectra graphed?, popup, Yes;No
DoPrompt Model Selection, Graph

If(CmpStr(Graph,Yes)==0)
    Display
EndIf
If (strlen(outputPaths) == 0)
   Print Cancelled
Else
   Variable numFilesSelected = ItemsInList(outputPaths, \r)
   Variable i,MaxFound,MaxSum
   Make/O/N=(2116,numFilesSelected) IntensityTable
   Make/O/N=((numFilesSelected*numFilesSelected-numFilesSelected)/2)/T
       NamesList
   //edit IntensityTable
   for(i=0; i<numFilesSelected; i+=1) //iterates until out of files
         String path = StringFromList(i, outputPaths, \r) //loads ith
            files location to path
```

```
 String Pathname=
    String fileName = ParseFilePath(3, path, ;, 0, 0) // Get file
        name without extension
       String baseShiftName = Shift
    String baseIntensityName =
    Variable baseMaxNameLength =
        max(strlen(baseShiftName),strlen(baseIntensityName))
    Variable maxIgorNameLength = 31

    // This is to make sure that your wave names dont wind up
        being too long for Igor to handle
    Variable clippedFileNameLength = maxIgorNameLength -
        baseMaxNameLength
 String clippedFileName = fileName[0,clippedFileNameLength-1]
 // Print clippedFileName // For debugging only

 String columnInfoStr =
 columnInfoStr += N= + baseShiftName + clippedFileName + ;
   columnInfoStr += N= + baseIntensityName + clippedFileName + ;
 // Print columnInfoStr // For debugging only

 LoadWave/Q/A/G/D/B=columnInfoStr/K=0/P=$pathName path  // Load
    waves

String wavesLoadedList = S_waveNames // S_waveNames is created by
   LoadWave
     String firstName = StringFromList(0, wavesLoadedList)
 Wave ShiftWave = $firstName                // Wave containing
```

```
        shift values
    String secondName = StringFromList(1, wavesLoadedList)
    NamesList[i]=secondName
    Wave IntensityWave = $secondName    //Wave with corresponding
        intensity values
    DeletePoints 2116,200, IntensityWave;
    DeletePoints 2116,200, ShiftWave;



        MaxFound=WaveMax(IntensityWave)
        IntensityWave=IntensityWave/MaxFound


        IntensityTable[][i]=IntensityWave[p] //creates table with
            Intensity values with in-spectra normalization
        If(CmpStr(Graph,yes)==0)
        AppendToGraph IntensityWave vs ShiftWave
        EndIf
 EndFor



If (strlen(outputPaths) == 0)
Print Cancelled
Else
Make/O/N=((numFilesSelected*numFilesSelected-numFilesSelected)/2)
    RelativeScore
Make/O/N=((numFilesSelected*numFilesSelected-numFilesSelected)/2)
    RawScore
Make/O/N=(2116,(numFilesSelected*numFilesSelected-numFilesSelected)/2)
```

```
    ProductWaves
  Make/O/N=((numFilesSelected*numFilesSelected-numFilesSelected)/2)/T
    FirstWave
  Make/O/N=((numFilesSelected*numFilesSelected-numFilesSelected)/2)/T
    SecondWave



//  Edit ProductWaves
  Edit RawScore
  AppendToTable RelativeScore, FirstWave, SecondWave
  ModifyTable width(FirstWave)=180
  ModifyTable width(SecondWave)=180
   For(i=0;i<numFilesSelected-1;i+=1)          //This loop multiplies
       Intensity waves together to generate one product wave
         For(j=i+1;j<numFilesSelected;j+=1)     //for every unique
             combination of 2 intensity waves. I.E. gives one product
             wave
             If(i!=j)                                          //for
                 wave mult of 1x2 and 2x1 and ignores cases such as 1x1,
                 2x2 etc.
              ProductWaves[][k]=IntensityTable[p][i]*IntensityTable[p][j]
              FirstWave[k]=NamesList[i]
              SecondWave[k]=NamesList[j]
              ElseIf(i==j)
              EndIf
              k+=1
            EndFor
   EndFor
```

```
    Make/O/N=(1,DimSize(ProductWaves,1)) WaveSums
    Make/O/N=(1,DimSize(ProductWaves,1)) NormalizedWaveSums


    MatrixOp/O WaveSums=SumCols(ProductWaves) //Finds largest sum from
       the sums of all product waves.
    wavestats/W/Q WaveSums
    NormalizedWaveSums=WaveSums/V_max


    For(i=0;i<(numFilesSelected*numFilesSelected-numFilesSelected)/2;i+=1)
       //This loop generates the Similarity Score table by
       automatically assigning values of 1 for comparisons of 1 vs 1, 2
       vs 2, etc.
        RawScore[i]=WaveSums[0][i]
        RelativeScore[i]=NormalizedWaveSums[0][i]
    EndFor
    EndIf


EndIf


  If(CmpStr(Graph,yes)==0)
  ModifyGraph fSize=14;DelayUpdate
    Label left \\Z16Normalized Intensity\\u#2;DelayUpdate
    ModifyGraph nticks(left)=0,lblPosMode(left)=3,lblPos(left)=30
    Label bottom Raman Shift (cm\\S-1\\M)
   AlterTrace()
```

```
      Legend/C/N=text5/F=0/B=1/X=-8.00/Y=-10.00
      EndIf

   return outputPaths    // Will be empty if user canceled
End

//////////////////////
//////////////////////

//////////////////////
//////////////////////


Function AlterTrace()              // colors traces with different colors
   String Traces  = TraceNameList(,;,1)        // get all the traces from
      the graph
   Variable Items = ItemsInList(Traces)          // count the traces
   Make/FREE/N=(14,3) colors = {{65280,54528,32768}, {65280,43520,0},
      {65280,0,0}, {52224,0,20736}, {65280,32768,45824}, {52224,0,41728},
      {65280,32768,58880}, {26368,0,52224}, {44032,29440,58880},
      {32768,32768,39680}, {16384,28160,65280}, {0,34816,52224},
      {16384,48896,65280}, {0,52224,52224}, {0,39168,0}, {26112,52224,0},
      {65280,54528,32768}, {65280,43520,0}, {65280,0,0}, {52224,0,20736},
      {65280,32768,45824}, {52224,0,41728}, {65280,32768,58880},
      {26368,0,52224}, {44032,29440,58880}, {32768,32768,39680},
      {16384,28160,65280}, {0,34816,52224}, {16384,48896,65280},
      {0,52224,52224}, {0,39168,0}, {26112,52224,0}}
   Variable i,offset=0
```

```
   for (i = 0; i<DimSize(colors,1); i += 1)
      ModifyGraph
          rgb($StringFromList(i,Traces))=(colors[0][i],colors[1][i],colors[2][i])
           // set new colors
      ModifyGraph lsize($StringFromList(i,Traces))=2
             ModifyGraph offset($StringFromList(i,Traces))={0,offset}
         offset+=0.25
   endfor
      ModifyGraph offset($StringFromList(0,Traces))={0,0}
End
```